QCD TOPOLOGY AND LATTICE PERTURBATION THEORY FROM MONTE CARLO SIMULATIONS WITH IMPROVED STAGGERED FERMIONS

by

Kit Yan Wong

B.Sc., University of New Brunswick, 1999

M.Sc., Simon Fraser University, 2002

THESIS SUBMITTED IN PARTIAL FULFILLMENT

OF THE REQUIREMENTS FOR THE DEGREE OF

DOCTOR OF PHILOSOPHY

in the Department

of

Physics

SIMON FRASER UNIVERSITY

Summer 2005

APPROVAL

Name: Kit Yan Wong

Degree: Doctor of Philosophy

Title of thesis: QCD Topology and Lattice Perturbation Theory from Monte Carlo Simulations with Improved Staggered Fermions

Examining Committee: Dr. M. E. Hayden (Chair)

Dr. H. D. Trottier, Senior Supervisor
Professor, Department of Physics

Dr. R. M. Woloshyn, Co-Supervisor
Senior Research Scientist, TRIUMF
Adjunct Professor, Department of Physics, SFU

Dr. G. Kirczenow, Supervisor
Professor, Department of Physics

Dr. B. K. Jennings, Internal Examiner
Senior Research Scientist, TRIUMF
Adjunct Professor, Department of Physics, SFU

Dr. R. Gupta, External Examiner
Group Leader, Elementary Particles and Field Theory
Group, Los Alamos National Laboratory

Date Approved: July 11, 2005

SIMON FRASER UNIVERSITY

PARTIAL COPYRIGHT LICENCE

Abstract

The staggered quark formulation is one of many ways to include fermions on the lattice. Dynamical simulations are now routinely done with improved staggered quark actions which are more efficient than other popular formalisms. In this thesis two research works on improved staggered fermions are presented.

A systematic study of the staggered Dirac operator's spectral properties is first presented. It is a long standing belief that staggered fermions do not feel gauge field topology because of the lack of zero eigenvalues of the operator at finite lattice spacing. The existence of fermionic zero modes in topological nontrivial background gauge fields is required by the Atiyah-Singer index theorem. In this study we observe that eigenmodes with very small eigenvalue and large chirality appear if improved staggered operators are used. These small eigenmodes can be identified as the "zero modes" associated with the topology of the gauge fields. We have also compared the distribution of the remaining nonchiral modes with the predictions of Random Matrix Theory. Satisfactory agreement is obtained.

In the second project perturbative expansions of Wilson loops are computed in full QCD from Monte Carlo simulations with improved staggered fermions. This approach provides a much simpler alternative to diagrammatic perturbation theory, and has previously been shown to be successful in reproducing the perturbation series in pure gauge theory. This method is applied here for the first time to unquenched QCD. Twisted boundary conditions are used to eliminate effects of zero momentum modes and to suppress tunneling between the degenerate Z_3 vaccua. A new simulation algorithm, the rational hybrid Monte Carlo algorithm, with no finite step size error is also employed. This is the first time this algorithm has been used in a numerical application. Results are in excellent agreement with analytic perturbation theory; this provides an important cross-check of the perturbation theory input to a recent determination of the strong coupling $\alpha_{\overline{MS}}(M_Z)$ by the HPQCD collaboration.

Dedication

To my parents

Acknowledgements

I would like to express my sincere thanks to both of my supervisors, Dr. Trottier and Dr. Woloshyn, for all their support and guidance towards the completion of this work.

I would like to thank Dr. Herbut for teaching me renormalization group and critical phenomena. Thanks as well to Dr. Ballentine, Dr. Kirczenow, Dr. Jennings and Dr. Viswanathan for teaching me many courses here at SFU. I would also like to thank Dr. Plischke for his interest in this work and as a former committee member.

Thanks also to the staff of the Physics Department for all the help and encouragement. Special thanks are due to Candida Mazza, the graduate secretary, who has shielded me from all the paperwork and let me concentrate on my research.

I would also like to thank my schoolmates Matt Nobes, Sacha Kautsky, Karn Kallio, Matt Case, Dan Vernon and Peter Matlock for their support and many valuable discussions.

Contents

Dedication i

Approval ii

Abstract iii

Acknowledgements v

1 Introduction 1

1.1 Quantum Chromodynamics (QCD) and Lattice QCD 1

1.2 Chiral Symmetry, QCD Topology and the Index Theorem 5

1.3 Fermions on the Lattice – Staggered Fermions 9

1.4 Staggered Fermion Spectral Properties 11

1.5 Lattice Perturbation Theory from Monte Carlo Simulations 15

2 Lattice QCD 20

2.1 Gauge Fields on the Lattice 21

2.2 Fermions on the Lattice — The "Doubling" Problem 22

2.3 Staggered Fermions and Overlap Fermions 24

2.4 Improvement 33

3 QCD Topology and Spectral Properties of the Staggered Dirac Operator 41

3.1 The Index Theorem 42

3.2 Random Matrix Theory 45

3.3 Spectral Properties of Various Lattice Fermions 47

3.4 Simulations 49

3.5 Results 52

3.6 Conclusion 63

4 Lattice Perturbation Theory: An Example **66**

5 Lattice Perturbation Theory from Monte Carlo Simulations at Weak Coupling **73**

5.1 Zero Modes and Tunneling 75

5.2 Twisted Boundary Conditions 79

5.3 Simulation Algorithms 85

5.4 Other Systematic Errors 93

6 Results **99**

6.1 Analysis 100

6.2 The Unimproved Action 102

6.3 The MILC Action 108

6.4 Summary and Discussion 113

7 Conclusions **116**

A Fermion Force in Molecular Dynamics Evolution **119**

Bibliography **123**

List of Tables

1.1 Properties of different quark flavours 2

2.1 Comparison among the various fermion actions 31
2.2 Path coefficients for the various improved staggered quark actions . . 39

3.1 Simulation parameters and measured string tensions $\hat{\sigma} = a^2\sigma$ 51

5.1 Summary of the various systematic effects 98

6.1 Relevant momentum scale for various small Wilson loops 101
6.2 Comparison of Monte Carlo errors and induced errors 102
6.3 Simulation parameters for the unimproved action 103
6.4 Dependence on N and the prior width $\bar{\sigma}_n$ (the unimproved action) . . 104
6.5 Perturbative coefficients of Wilson loops (the unimproved action) . . 105
6.6 Second and third order coefficients with c_1 fixed to the analytic results (the unimproved action) 107
6.7 Third order coefficients with c_1 and c_2 fixed to the analytic results (the unimproved action) 108
6.8 Simulation parameters for the MILC action 109
6.9 Zero step size extrapolation for the R-algorithm 110
6.10 Dependence on N and the prior width $\bar{\sigma}_n$ (the MILC action) 111
6.11 Perturbative coefficients of Wilson loops (the MILC action) 112
6.12 Second and third order coefficients with c_1 fixed to the analytic results (the MILC action) 113
6.13 Third order coefficients with c_1 and c_2 fixed to the analytic results (the MILC action) 113

List of Figures

1.1 The quark model and the lightest meson and baryon multiplets . . . 3
1.2 Splitting of zero modes on the lattice 11
1.3 Eigenvalue spectrum for the unimproved staggered operator 12
1.4 Distribution of the smallest eigenvalues of the unimproved staggered operator 13
1.5 Cumulative distribution of the smallest eigenvalues of the overlap operator at $a \approx 0.123$fm and $V = 10^4$ 14
1.6 Examples of lattice Feynman rules 17
1.7 Examples of 2-loop diagrams 17

2.1 QCD on the lattice 22
2.2 Flavour-changing interactions 27
2.3 The pion mass spectrum 28
2.4 The computational cost for dynamical simulations with staggered fermions and Wilson fermions 32
2.5 Operators used in the improved gluon action 34
2.6 Tadpole diagram 35
2.7 Paths used in fat-link improved staggered quark actions 38
2.8 Pion spectrum computed using unitarized fat-link operators 40

3.1 Spectral density and lattice volume 49
3.2 Determination of lattice spacing from the static quark potential . . . 50
3.3 Spectral graphs for the different staggered operators with unimproved gauge fields 53
3.4 Ratios of eigenvalues between the smallest nonchiral mode and the largest "zero mode" for unimproved gauge fields 54

3.5 Topological charge distributions obtained by using different operators for unimproved gauge fields 55
3.6 Spectral graphs for the different staggered operators with improved gauge fields 56
3.7 Ratios of eigenvalues between the smallest nonchiral mode and the largest "zero mode" for improved gauge fields 57
3.8 Topological charge distributions obtained by using different operators with improved gauge fields 58
3.9 Dependence of the spectral density on lattice spacings 59
3.10 Dependence of the spectral density on lattice volume 60
3.11 The total number of zero modes of the UFat7×Asq operator for different lattice volumes 61
3.12 Topological charge distribution for different lattice volumes 62
3.13 Cumulative distribution of the smallest nonchiral modes in different topological sectors 64

4.1 The strong coupling constant $\alpha_s^{\overline{MS}}(M_Z)$ determined from various experiments and theoretical calculations 68

5.1 Example of tunneling for the Wilson plaquette action 77
5.2 Run history and scatter diagram of the temporal Polyakov loop P_t using periodic boundary conditions 78
5.3 Run history and scatter diagram of the temporal Polyakov loop P_t with xy-twist 84
5.4 Run history and scatter diagram of the temporal Polyakov loop P_t using xyz-twist 85
5.5 The HMC algorithm 88
5.6 Quality of the optimal rational approximation to $x^{-1/12}$ and $x^{1/24}$ . . 91
5.7 Plaquette autocorrelation functions at $\beta = 11.0$ and $\beta = 47.0$ in the MILC simulations 94
5.8 Dependence of the average plaquette on ϵ 95

6.1 Plots of κ_1, κ_2, κ_3 (2×2 loop, $n_f = 1$ for the unimproved action . . . 106
6.2 Zero step size extrapolation for the R-algorithm 110
6.3 Plots of κ_1, κ_2, κ_3 (2×2 loop, $n_f = 1$ for the MILC action 112

Chapter 1

Introduction

1.1 Quantum Chromodynamics (QCD) and Lattice QCD

The Quark Model, Colour Symmetry and QCD

The development of quantum field theory over the past few decades has substantially improved our understanding of the fundamental interactions in nature [1]. Quantum electrodynamics (QED), perhaps the best fundamental physical theory we have, describes the electromagnetic interaction between charge particles. On the other hand, the strong interaction, which is responsible for nuclear binding and the interaction of the constituents of nuclei, is well described by the theory of quantum chromodynamics (QCD).

In the early 60's before QCD was invented, the quark model was very successful in classifying the many strongly interacting particles (collectively called hadrons). The quark model utilizes the symmetries known from classical and quantum mechanics and suggests that hadrons are composed of elementary spin-1/2 fermions called quarks. Hadrons constituted from a quark anti-quark pair are called mesons (e.g. pions) and bound states of three quarks are called baryons (e.g., protons and neutrons). There are six different kinds of quarks: up (u), down (d), strange (s), charm (c), top (t) and bottom (b). Some of their properties are listed in Table 1.1. Different kinds of quarks are called flavours and they are indistinguishable in the limit of equal quark masses. The corresponding symmetry is a *global* flavour symmetry. In reality only an approximate SU(3) flavour symmetry (see Fig. 1.1) can be realized in the hadron

Quark flavour	u	d	s	c	b	t
Charge (e)	+2/3	-1/3	-1/3	+2/3	-1/3	+2/3
Mass (MeV)	1-5	3-9	75-170	1150-1350	4000-4400	174300
Iso-spin I_3	1/2	-1/2	0	0	0	0
Hyper-charge Y	1/3	1/3	-2/3	1/3	1/3	1/3

Table 1.1: Properties of different quark flavours. The quark masses are the $\overline{MS}$-masses evaluated at scale 2GeV, see Ref. [2] (the 2004 Review of Particle Physics) for details.

spectrum because the c, t and b quarks are much heavier. In addition, the SU(2) symmetry of the u and d quarks is a better symmetry because of their similar masses.

There is one major problem of the original quark model. The quark scheme assigns the resonance state Δ^{++} a uuu configuration with zero orbital angular momentum and all three quark spins parallel. This violates the Pauli exclusion principle. In other words the wavefunction of Δ^{++}, a spin-3/2 particle, is symmetric under particle exchange which is inconsistent with the spin-statistics theorem. The solution to this problem was provided by Han and Nambu, Greenberg and Gell-Mann in the late 60's. They proposed that quarks should carry an additional quantum number called "colour". There are three colours and they obey exact SU(3) symmetry. Since colour charges do not reveal themselves in nature, hadrons must be colour neutral, i.e., colour singlet states. This implies that mesons should have a colour-anti-colour configuration while the three quarks in baryons must be completely antisymmetric in their colour indices. This resolves the spin-statistics problem because the colour wavefunction of Δ^{++} is antisymmetric making the overall wavefunction also antisymmetric.

Despite the phenomenological success of the quark model and colour symmetry, a theory which connects the dynamics of colour and the strong interaction was still missing. The development of QCD was further stimulated by two experimental observations. First, the failure to isolate a free quark experimentally suggests that there exists some underlying dynamics assuring the **confinement of quarks**, i.e., quarks can only exist in bound states to form colour singlet hadrons. Secondly, by probing the inner structure of the proton with high energy electron beams, particle physicists determined that the **strong interaction becomes weak at short distances (high energy)**. Consequently for a theory to correctly describe the strong interaction, it must **exhibit both quark confinement in the low energy regime and a weak**

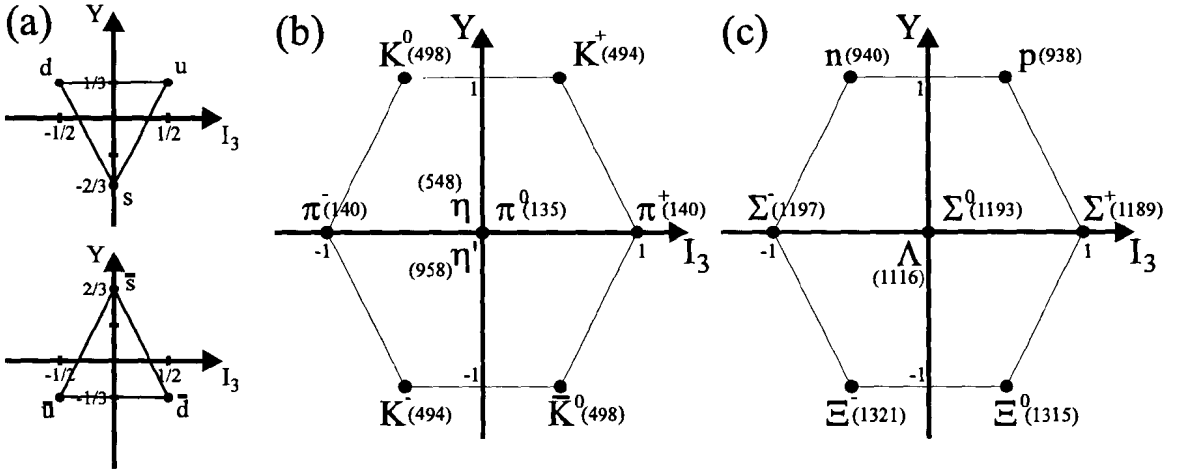

Figure 1.1: The quark model and the lightest meson and baryon multiplets (a) the approximate SU(3) flavour symmetry (b) nonet of spin-0 pseudo-mesons (c) octet of spin-1/2 baryons. The hadron masses (in MeV) are given in brackets. In the quark model, proton and neutron are assigned with a *uud* and *udd* configuration respectively, π^+ is $u\bar{d}$ and K^+ is $u\bar{s}$.

coupling limit at high energy.

In the early 70's, Politzer, Gross and Wilczek [3, 4] discovered a class of theories which has the property that the coupling becomes weak at high energy (this is known as asymptotic freedom) — the non-Abelian gauge theories. Non-Abelian gauge theories are theories with a *local* gauge symmetry, similar to that of QED but with non-Abelian gauge group structure. The colour symmetry was immediately identified as the gauge group, i.e., a *local* SU(3) colour symmetry. The colour quarks serve as the "charges" of QCD while gluons, the quanta of SU(3) gauge fields, play the role of photons in QCD. This quantum theory of colour charges is known as quantum chromodynamics (QCD).

For future reference we put down the *Euclidean* version of the QCD Lagrangian here [1]:

$$\mathcal{L}_E = \frac{1}{4}\left(F^a_{\mu\nu}\right)^2 + \sum_{\text{flavours } f} \bar{\psi}^f \left(D + m_f\right) \psi^f. \tag{1.1}$$

Euclidean field theory is considered because of two reasons. First, topological solutions are classical solutions of the *Euclidean* field equations. More importantly, changing to imaginary time converts QCD to a statistical system so that correlation functions

[1] Throughout this thesis, Latin letters a, b, ...denote colour indices and Greek letters α, β and μ, ν label spinor indices and space-time indices respectively.

can be computed numerically by Monte Carlo techniques [2]. In (1.1), $F^a_{\mu\nu}$ is the colour field strength tensor and $D \equiv \gamma^\mu D_\mu$ is the Dirac operator

$$\begin{aligned} F^a_{\mu\nu} &= \partial_\mu A^a_\nu - \partial_\nu A^a_\mu + g f^{abc} A^b_\mu A^c_\nu, \\ \gamma^\mu D_\mu &= \gamma^\mu \left(\partial_\mu - ig A^a_\mu t^a\right). \end{aligned} \tag{1.2}$$

The colour gauge fields are labeled by A^a_μ and $\psi^f_{\alpha a}$ are the quark fields. Here, f^{abc} are the structure constants and t^a are the generators of the SU(3) gauge group. The γ matrices (*Euclidean* version) are Hermitian and satisfy the following anti-commutation relations

$$\{\gamma_\mu, \gamma_\nu\} = 2\delta_{\mu\nu}, \quad \mu, \nu = 1, 2, 3, 4. \tag{1.3}$$

The chirality matrix γ_5 is defined by

$$\gamma_5 \equiv \gamma_1\gamma_2\gamma_3\gamma_4, \quad \{\gamma_5, \gamma_\mu\} = 0, \tag{1.4}$$

which is also Hermitian. The Lagrangian is invariant under a *local* SU(3) transformation, $V(x) = \exp\left(i\alpha^a(x)t^a\right)$, with phases $\alpha^a(x)$

$$\begin{aligned} \psi(x) &\rightarrow V(x)\psi(x), \\ A^a_\mu(x)t^a &\rightarrow V(x)\left(A^a_\mu(x)t^a + \frac{i}{g}\partial_\mu\right)V^\dagger(x). \end{aligned} \tag{1.5}$$

The strong coupling constant is $\alpha_s \equiv \frac{g^2}{4\pi}$. Notice the similarity between (1.1) and the standard QED Lagrangian. Note that since $\{\gamma_5, \gamma_\mu\} = 0$, D anti-commutes with the chirality matrix also

$$\{\gamma^5, D\} = 0. \tag{1.6}$$

Lattice QCD

Because of asymptotic freedom the strong coupling constant α_s becomes small in the high energy regime or at short distances. This allows precision tests of QCD where perturbative QCD gives accurate calculations of certain processes that can be observed in high energy experiments. An example is the jet production in hadron collisions [1]. On the other hand, quark confinement and other low energy properties

[2] This is because the original oscillatory factor $\exp[iS] = \exp\left[i\int d^4x\mathcal{L}\right]$ in the partition function becomes a Boltzmann weight $\exp[-S_E] = \exp\left[-\int d^4x\mathcal{L}_E\right]$ in Euclidean field theory.

of hadrons, such as their masses and decay rates, cannot be demonstrated or computed from a perturbative calculation. Non-perturbative treatment is required.

Lattice QCD was originally invented by Wilson around 1974 [5] (see Ref. [6] for a review on the origins of lattice field theory) to study non-perturbative physics. The continuum gauge theory is replaced by a discrete statistical mechanical system on a 4-dimensional Euclidean lattice. The lattice not just provides an integration grid but also a cutoff in momentum, i.e., a regularization scheme. With this formulation of QCD, Wilson showed that QCD exhibits confinement of colours in the strong coupling limit. In fact, numerical simulations [7, 8] confirmed a linearly rising potential between a static quark anti-quark pair at moderate separation.

The major challenge of lattice QCD is to reduce the discretization errors and lattice artifacts introduced by the lattice spacing a. Computational cost scales as best as a^{-6} [9] and hence reducing the lattice spacing is not feasible. Until recently it was not possible to do lattice simulations of sufficient precision even on the largest available computer clusters. Fortunately the proposal of improved lattice actions with better continuum properties and smaller discretization errors in the last decade dramatically reduced the amount of computer power that is required. Accurate lattice calculations are now available [10]. An example is the accurate determination of the value of the strong coupling constant [11, 12, 13]. This will be discussed in Section 4.1. Another example is the precise determination of the CKM matrix elements [14], which is important to the search for new physics.

A brief introduction to lattice QCD will be given in Chapter 2.

1.2 Chiral Symmetry, QCD Topology and the Index Theorem

Another non-perturbative aspect of QCD where lattice models have provided important insights is topological effects. Topological solutions are finite energy classical solutions to the non-linear field equations of the system. In QCD, the Euclidean version of the self-coupled pure gauge theory, i.e., the first term in (1.1), possesses topological solutions. The first project of the thesis is the study of QCD topology on the lattice with improved staggered fermions. These finite energy solutions have important phenomenological consequences because they are directly related to the chiral symmetry of QCD. We are now going to give a brief review on this subject.

Chiral Symmetry in QCD and the $[U(1)]_A$ Problem

As mentioned before, the QCD Lagrangian (1.1) has an approximate SU(3) flavour symmetry, i.e., it is invariant under the following *global* transformation

$$[SU(3)]_V : \quad \psi(x) \to e^{i\omega^a \tau^a} \psi(x), \tag{1.7}$$

where τ^a are the generators of the SU(3) flavour symmetry group [3]. This symmetry is reflected in the particle spectrum where hadrons fall into easily recognizable multiplets as shown in Fig. 1.1. The Lagrangian is also invariant under a *global* U(1) phase transformation

$$[U(1)]_V : \quad \psi(x) \to e^{i\omega} \psi(x). \tag{1.8}$$

This symmetry can be realized physically as the conservation of baryon number. Overall the symmetry group is SU(3)×U(1).

Aside from these symmetries there are two additional "chiral" symmetries in the limit of *zero quark masses*

$$[SU(3)]_A : \quad \psi(x) \to e^{i\theta^a \tau^a \gamma^5} \psi(x), \tag{1.9}$$

and

$$[U(1)]_A : \quad \psi(x) \to e^{i\theta \gamma^5} \psi(x). \tag{1.10}$$

This is a good approximation because the masses of the u, d and s quarks are relatively small compared to the energy scale of most hadronic processes, which is about $\Lambda_{QCD} \sim 200$MeV [2]. Note that the chiral symmetries are equivalent to the anti-commutation (1.6), $\{\gamma^5, D\} = 0$, and the symmetry group is extended to SU(3)×SU(3)×U(1)×U(1). However, none of these chiral symmetries can be realized in nature because a direct manifestation of $[SU(3)]_A$ and $[U(1)]_A$ would require each hadron multiplet to be accompanied by a mirror multiplet of the same mass, but with opposite parity. For example, there is not even an approximate mirror image of the proton and neutron.

Assuming that the real world is well approximated by the chiral symmetric limit, we must conclude that the symmetries $[SU(3)]_A$ and $[U(1)]_A$ are spontaneously broken (it turns out that this is not true for $[U(1)]_A$, see below), giving rise to a set of massless

[3] We use the symbol τ here in order to distinguish from the generators of the SU(3) colour symmetry group mentioned earlier. Also the index a refers to flavour indices instead of colour.

particles (Goldstone bosons) associated with the generators of the broken symmetry group. This is indeed the case for $[SU(3)]_A$ where the Goldstone bosons are the eight light mesons, $\boldsymbol{\pi}$, $\mathbf{K}$, and η, listed in Fig. 1.1. These mesons are not exactly massless because the symmetry $[SU(3)]_A$ is also explicitly broken by the small quark masses of u, d and s. On the other hand, the next lightest pseudo-scalar meson $\eta'(985\text{MeV})$ would be the Goldstone boson if $[U(1)]_A$ is also considered to be spontaneously broken. However this Goldstone boson is expected to have a mass comparable to those of $\boldsymbol{\pi}$ because they all have the same quark configuration. In fact, using chiral perturbation theory, Weinberg estimated the mass to be less than $\sqrt{3}m_\pi$ [15]. With its mass at 985MeV, η' cannot be considered as the Goldstone boson associated with the spontaneously breaking of $[U(1)]_A$ because it violates the Weinberg's bound. This is the famous $[U(1)]_A$ problem: why η' is so heavy?

The Axial Anomaly and QCD Topology

According to the Noether theorem (see for example [1]), *classically*, there is a conserved current associated with the $[U(1)]_A$ symmetry

$$j^{\mu 5} = \bar{\psi}\gamma^\mu\gamma^5\psi \quad \text{and} \quad \partial_\mu j^{\mu 5} = 0, \tag{1.11}$$

for massless quarks. However, the conservation of the axial current is actually spoiled by quantum effects. In QCD, careful analysis [16, 17] gives the following operator equation

$$\partial_\mu j^{\mu 5} = -\frac{g^2 n_f}{32\pi^2}\epsilon^{\mu\nu\rho\sigma}F^a_{\mu\nu}F^a_{\rho\sigma}, \tag{1.12}$$

where n_f is the number of quark flavours and $\epsilon^{\mu\nu\rho\sigma}$ is the totally antisymmetric tensor with $\epsilon^{0123} = 1$ and vanished if two indices are the same. This is known as the Adler-Bell-Jackiw anomaly or the axial anomaly. The anomaly implies that, at the *quantum* level, there is no $[U(1)]_A$ symmetry and no associated Goldstone boson. Therefore strong interaction contains no light flavour-singlet pseudo-scalar meson with a mass comparable to those of the pions.

The anomalous non-conservation relation (1.12) is related to one of the most fundamental problems in quantum field theory. We cannot fully discuss this issue here, and refer the interested readers to the original articles and Ref. [1] for further details. In brief, it can be shown that $\partial_\mu j^{\mu 5} = 0$ is incompatible with gauge invariance or charge conservation at the quantum level. The axial anomaly arises when one insists

on the definition $\partial_\mu j^\mu \equiv 0$, i.e., charge conservation. Since gauge invariance or charge conservation is the most important property of a field theory, we have to sacrifice conservation of the $[\mathrm{U}(1)]_A$ current.

Notice that the residual on the right hand side of (1.12) depends only on the background gauge field and can be written as a total derivative of a quantity. Hence it is possible to retain the global conservation law if the quantity falls off sufficiently rapidly at infinity so that its integral vanishes. This leads us to QCD topology. As mentioned earlier, pure gauge theories contain topological solutions which are extended solutions of the non-linear field equations. These solutions are stable despite the non-linear nature of the parent theories, and are characterized by some conserving topological indices (topological charges). The topological index Q of a SU(3) configuration is precisely given by the integral of the residual in (1.12) [18]

$$Q = -\frac{g^2 n_f}{32\pi^2} \int d^4x \epsilon^{\mu\nu\rho\sigma} F^a_{\mu\nu}(x) F^a_{\rho\sigma}(x), \tag{1.13}$$

and consequently

$$Q = \int d^4x \partial_\mu j^{\mu 5}(x). \tag{1.14}$$

Therefore axial current is conserved only in the world with $Q = 0$. For configurations with nontrivial topology the integral of $\partial_\mu j^{\mu 5}(x)$ takes a non-zero value.

Apparently topological effects are responsible for the non-conservation of the axial current, which in turn explains why the η' meson is so heavy. In the late 70's, by studying the large N_c (N_c is the number of colours) limit of the $\mathrm{SU(N_c)}$ colour gauge group, Witten and Veneziano were able to extend these ideas and explicitly derive a formula for the η' mass (Witten-Veneziano's formula) [19, 20]

$$\chi \equiv \frac{\langle Q^2 \rangle}{V} = \frac{f_\pi^2}{6} \left(m_\eta^2 + m_{\eta'}^2 - 2m_K^2 \right), \tag{1.15}$$

where V is the volume of the system and $f_\pi^2 \sim 93\mathrm{MeV}$ [2] is the pion decay constant which can be determined experimentally. This formula shows that gauge field topology is indeed important to QCD phenomenology. Topological solutions are non-perturbative so it is not possible to obtain the topological susceptibility χ from a perturbative calculation. Lattice QCD, on the other hand, provides a direct means to which χ can be determined from numerical simulations.

The Index Theorem

Another consequence of QCD topology is the existence of zero eigenvalues of the Dirac operator $D = \gamma^\mu D_\mu = \gamma^\mu \left(\partial_\mu - igA^a_\mu t^a\right)$ in background gauge fields with non-trivial topological structure. This is known as the Atiyah-Singer index theorem [21]. An informal derivation of the theorem will be given in Section 3.1 and here we only give a short summary of its implications.

The quark field ψ can be decomposed into left- and right-handed chiral components ψ_L and ψ_R

$$\psi = \psi_L + \psi_R; \quad \psi_L = \left(\frac{1-\gamma^5}{2}\right)\psi, \quad \psi_R = \left(\frac{1+\gamma^5}{2}\right)\psi. \tag{1.16}$$

The chirality of ψ is given by $\chi = \langle\psi|\gamma^5|\psi\rangle$ where γ^5 is the chirality operator defined in (1.4). Since $(\gamma^5)^2 = 1$, ψ_L and ψ_R are eigenvectors of γ^5 with chirality -1 and +1 respectively.

We are now ready to discuss the index theorem. It states that, for gauge field configurations with non-zero topological charge index Q, some of the eigenmodes of the Dirac operator D should have zero eigenvalues and definite chirality ± 1. The difference in the numbers of left-handed zero modes (n_L) and right-handed chiral modes (n_R) is equal Q

$$Q = \text{index}(D) \equiv n_R - n_L. \tag{1.17}$$

The index theorem provides a convenient definition for the topological index Q. Given a gauge field configuration, its topology can be determined by computing a few lowest eigenvalues of D and then counting how many left- and right- handed chiral modes are present. In the the first project of the thesis we study the validity of this procedure for the staggered Dirac operator.

1.3 Fermions on the Lattice – Staggered Fermions

The index theorem allows the topological index of the gauge field to be determined by counting the number of zero chiral modes of the Dirac operator. Discretization of the Dirac action, however, is complicated by the so-called "fermion-doubling" problem. A detailed discussion of this problem will be presented in Section 2.2. In brief, the naïve discretization scheme, where one simply replaces the continuum derivative in (1.2) by

a finite difference on the lattice, leads to an action which describes 2^d continuum-like fermions rather than one! Here d is the dimension of the space-time and hence the number of modes doubles for each additional dimension. The excess fermions are called doublers and their presence is a lattice artifact. When the coupling to gauge field is turned on, the doubler modes are allowed to interact through the exchange of highly virtual gluons.

There are several approaches to the doubling problem. We will concentrate on the staggered quark discretization scheme in this thesis. In this formalism one accepts fermion doubling and identifies the excess fermions with other fermion degrees of freedom such as quark flavours. There are two steps in constructing the staggered quark action (see Section 2.3 for details). First one "spin-diagonalizes" the naïve action by making an appropriate transformation of the quark fields. Secondly, since the naïve quark action is now diagonal in spinor space and the 4 spinor components are decoupled, one can throw away three components and keep only one. The resulting action is the standard staggered quark action, and let us call the 1-component staggered quark fields χ. Because the number of degrees of freedom is reduced to 4 in the staggered quark scheme, the staggered quark action describes 4 equivalent flavours. The origin of the name "staggered" becomes clear when the action is re-written in terms of the four 4-component spinors [22]: the lattice is first divided into elementary 4-dimensional hypercubes, and the Dirac spinors at each hypercube (i.e., the lattice spacing is effectively doubled) can be constructed by forming certain linear combination of the 16 χ-fields located at the 16 corners of the hypercube. Therefore the 16 components of the four quark fields are "staggered" on the lattice.

The major advantage of the staggered quark formulation is that it is computationally the most efficient (as the system's number of degrees of freedom is reduced) among the various implementations, e.g., about 10 times faster than the Wilson fermions and 1000 times faster than the overlap fermions [4].

On the other hand the unconventional identification of doubler modes as quark flavours complicates the interpretation of staggered quark simulations. In particular interactions between the doublers correspond to flavour-changing interactions in the flavour basis, which are again purely lattice artifacts and have no continuum analogue. The flavour-changing interactions explicitly break the continuum SU(4) flavour sym-

[4]The cost also depends on the quark masses (see Table 2.1 and Fig. 2.4 in Section 3.3). The comparison is made at the values used in present-day dynamical simulations.

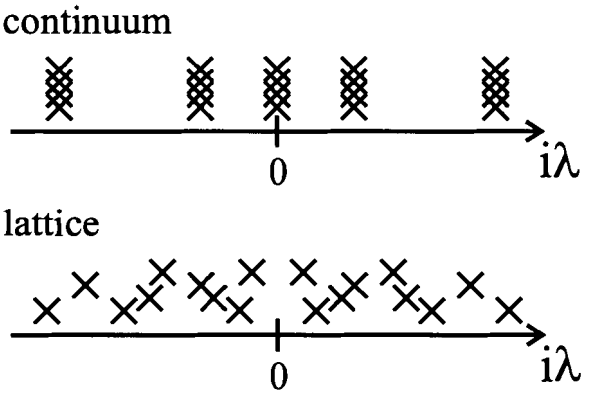

Figure 1.2: Splitting of zero modes on the lattice. The continuum 4-fold degeneracy is lifted so that any continuum zero modes will move away from zero.

metry and can have significant impact on the phenomenology. An example is that the 16 pions, associated with the spontaneously breaking of the flavour symmetry, are no longer degenerate (see Section 2.3 for more details).

Another example which is relevant to QCD topology is the lack of zero eigenvalues of the staggered Dirac operator. This can be understood as follows. The staggered quark operator describes 4 quark flavours in the continuum limit and the eigenvalue spectrum has a 4-fold degeneracy in this limit. At finite lattice spacing, however, the flavour-changing interactions break the flavour symmetry and the degeneracy is lifted. Hence any continuum zero modes will move away from zero on the lattice. This property is demonstrated in Fig. 1.2.

1.4 Staggered Fermion Spectral Properties

According to the index theorem, zero eigenvalues appear when the background gauge fields have nontrivial topological structure. It is therefore conventional wisdom that **staggered fermions do not feel gauge field topology because of the lack of zero eigenvalues of the operator.** This can be easily checked in numerical simulations by inspecting the microscopic eigenvalue spectrum. In Fig. 1.3 we have plotted the lowest 10 eigenmodes (chirality χ vs. eigenvalue λ) of the *unimproved* staggered operator for 50 gauge field configurations on 10^4 lattices. The lattice spacing is about 0.123fm which is relatively coarse (see Section 3.4 for details of the simulation). The spectrum clearly indicates that all configurations have zero topological charge. There are no zero modes, otherwise a cluster of states with very small λ and large χ would

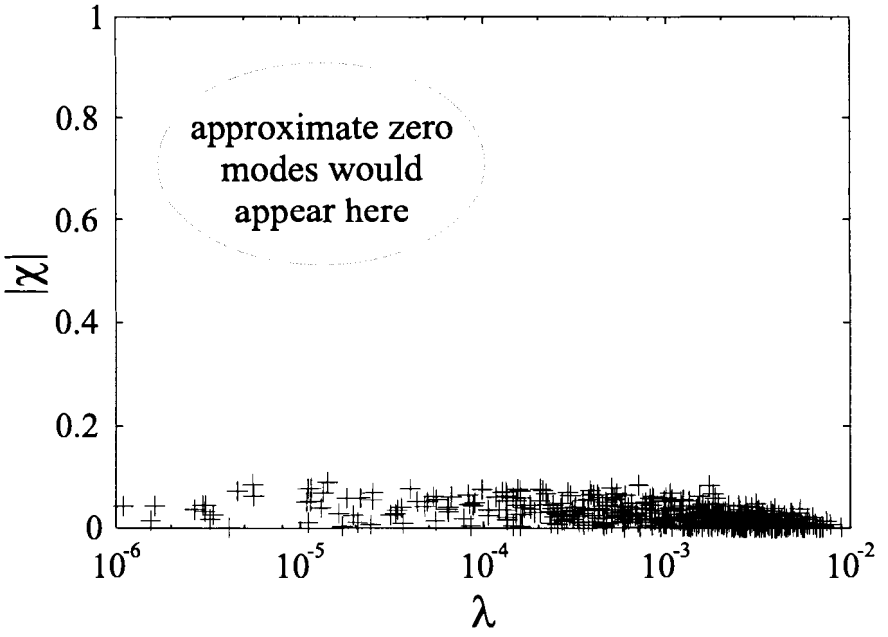

Figure 1.3: Eigenvalue spectrum for the *unimproved* staggered operator. It is clear that there are no, not even approximate, zero modes. The *unimproved* operator is insensitive to the topology at this lattice spacing ($a \approx 0.123$fm) and volume ($V = 10^4$).

be visible. One may suspect that our lattice is too small to hold topological solutions (which are extended objects) so that the gauge fields really do have trivial topological structure. We indeed observe that the number of configurations that have $Q = 0$ increases with decreasing volume. However, results in Chapter 3 show that (see Fig. 3.5) about 70% of the configurations should have $Q \neq 0$ at this lattice spacing and volume.

This unpleasant feature of staggered fermions was further revealed in comparisons of the eigenvalue spectrum obtained in simulations with the predictions of Random Matrix Theory (RMT) [23, 24, 25]. RMT gives analytic expressions for the distribution of the low-lying *nonchiral* modes in different topological sectors [26]. A short introduction to RMT will be given Section 3.2. In Ref. [23, 24, 25], the eigenvalue distribution in *all* topological charge sectors was found to be consistent with the predictions of RMT for topological charge equal to zero.

In particular, Fig. 1.4 shows the distribution of the smallest eigenvalues, $\rho^Q_{\rm min}(\zeta)$, of the *unimproved* staggered operator at $a \approx 0.123$fm and $V = 10^4$. Here $\zeta = \lambda \Sigma V$ where Σ is the infinite-volume chiral condensate (see (3.24)). Results are taken from Ref. [25]. The authors first calculated the topological charges of the gauge fields using

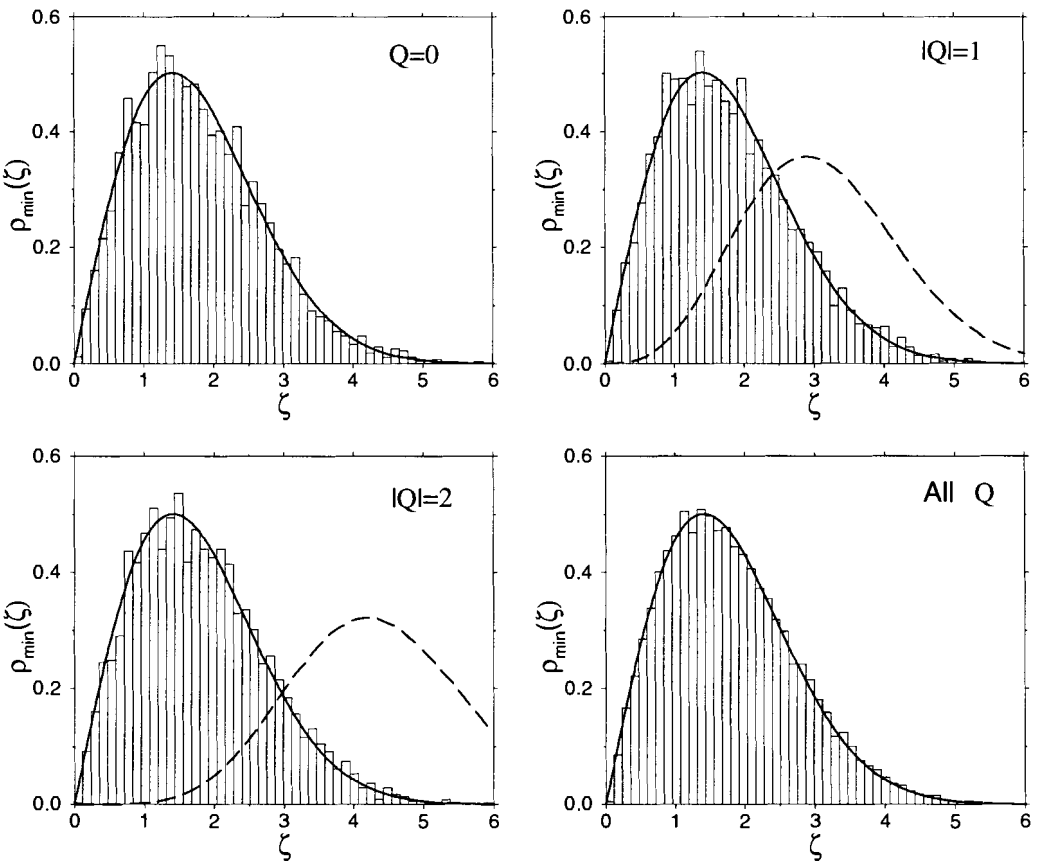

Figure 1.4: Distribution of the smallest eigenvalues of the *unimproved* staggered operator at $a \approx 0.123$fm and $V = 10^4$. Results are taken from Ref. [25]. Histograms are simulation results and dotted curves are predictions of RMT, see (3.24).

a discretized version of the continuum formula (1.13). The configurations were then classified and the distribution of the smallest eigenvalues was computed in each topological sector (the histogram). Overall about 17,000 gauge field configurations were analyzed [5]. The dotted curves are predictions of RMT (see (3.24)). It is worrisome that all results agree perfectly with the $Q = 0$ distribution even though the configurations have been divided into different charge sectors using the naïve formula (1.13). The *unimproved* staggered operator clearly fails to see the gauge field topology at this lattice spacing and volume.

This result should be compared with those of the overlap Dirac operator. As we

[5]There is always a small renormalization of the topological charge on the lattice so that it is not exactly equal to an integer. About 10% of the total configurations were thrown out in this study because their charge indices could not be determined unambiguously using (1.13).

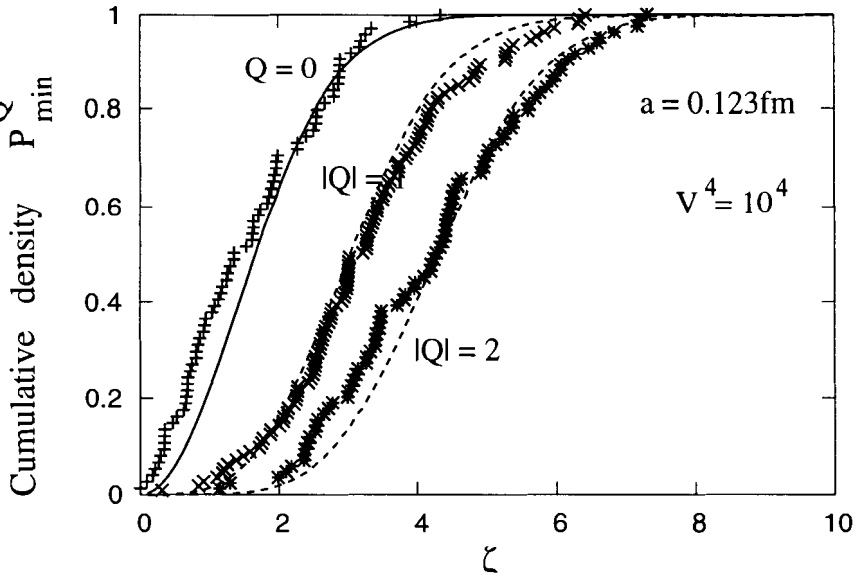

Figure 1.5: Cumulative distribution of the smallest eigenvalues of the overlap operator at $a \approx 0.123$fm and $V = 10^4$. Results are taken from Ref. [29]. Solid curves are predictions of RMT, see (3.25).

will see in Chapter 2, the overlap Dirac operator satisfies the Ginsparg-Wilson relation [27] and therefore there exists a symmetry on the lattice which can be interpreted as the continuum chiral symmetry [28]. Consequently, unlike the staggered Dirac operator, the overlap operator has exact chiral modes even at finite lattice spacing, and the eigenvalue spectrum shows a better agreement with the predictions of RMT. This can be observed in Fig. 1.5 where the *cumulative* distribution of the smallest eigenvalues $P^Q_{\rm min}(\zeta)$ (see (3.25)), after deleting the zero modes, is plotted for different charge indices. The results are taken from Ref. [29] with $a \approx 0.123$fm and $V = 10^4$, exactly the same as those used in Fig. 1.4. One can see that there are clear distinctions between the results with different Q and agreement with RMT is impressive.

Since flavour-changing interactions cause the continuum zero modes of the staggered Dirac operator to move away from zero, it has been suggested [30] that sensitivity to gauge field topology can be increased if one can reduce flavour-changing effects. Significant progress on controlling flavour-changing interactions has been made over the past few years through the invention of improved staggered quark actions constructed using fat-links [31]. In this study, we observe that the distribution of the low-lying eigenmodes depends quite sensitively on the way in which the operator is improved. Eigenmodes with very small eigenvalue and large chirality appear as the level of improvement increases. These small eigenmodes can be identified as the "zero

modes" associated with the topology of the background gauge fields. We also observe that separation between the "zero modes" and the nonchiral modes increases even more if the gauge field action is also improved, or when the lattice spacing is reduced. These show that discretization errors and lattice artifacts are indeed responsible for the failure of staggered fermions to see gauge field topology in Ref. [23, 24, 25] where the *unimproved* operator was used. Finally, after successfully identifying the "zero modes", the distribution of the remaining nonchiral modes is compared with the predictions of RMT. Satisfactory agreement is obtained for *all* charge sectors.

1.5 Lattice Perturbation Theory from Monte Carlo Simulations

The second topic of the thesis demonstrates how perturbative quantities can be efficiently computed from Monte Carlo simulations at weak coupling. In particular, perturbative series of Wilson loops are obtained, through third order, in *full* QCD with improved staggered fermions.

Lattice Perturbation Theory and Its Complexity

At first it may seem surprising to do perturbative calculations on the lattice since lattice QCD was originally invented to study non-perturbative physics like the hadron spectrum. However, lattice QCD is an effective field theory formulated on a grid with lattice spacing a and is therefore different from continuum QCD at short distance ($< a$). Since QCD is an asymptotically free theory, these short distance effects can be studied using perturbation theory. We will encounter two applications of lattice perturbation theory in this thesis. Perturbative improvement of lattice actions will be discussed in Section 2.4. We will see how the missing physics can be included back into the lattice theory by matching perturbatively the scattering amplitudes in lattice QCD to those of the continuum. Lattice perturbation theory is also important in connecting simulation results to physical quantities in the continuum. This will be illustrated in Chapter 4 where we will discuss how to extract the strong coupling constant $\alpha_s^{\overline{MS}}(M_Z)$ from simulation data using perturbation theory.

It is worth knowing to what order perturbative calculations must be done. We are interested in the expansions the observable $\mathcal{O}$

$$\mathcal{O} = c_1\alpha + c_2\alpha^2 + c_3\alpha^3 + \ldots \tag{1.18}$$

Affordable dynamical simulations can only be done for lattice spacings as small as $a \approx 0.1$fm. The value of α at this scale can be estimated from the typical low energy scale of QCD, which is $\Lambda_{QCD} \approx 200$MeV:

$$\alpha(0.1\text{fm}) \approx a\Lambda_{QCD} \approx 0.2 - 0.3. \tag{1.19}$$

Therefore in order to obtain high precision predictions of physical quantities from lattice simulations, perturbative matching must be done through α^2 (1-loop) or even α^3 (2-loop) to reduce systematic errors to a few percent.

Lattice perturbation theory can be done in the same way as continuum perturbation theory using Feynman rule techniques. Analytic calculations, however, are **extremely difficult** because of the enormous number of diagrams that have to be evaluated. Typically, the number is of $\mathcal{O}(10)$ for a 1-loop calculation, and of $\mathcal{O}(100)$ for 2-loop! Perturbation theory on the lattice is **even more challenging** because lattice actions have complicated structure and have complicated Feynman rules. Many of them have no continuum analogue also [22, 32]. This is particular true for the highly improved actions that are now commonly used in numerical simulations. To illustrate this problem, Fig. 1.6 and 1.7 shows some of the Feynman rules and loop diagrams that appear in the 2-loop calculation for the Wilson loops [33, 32]. We should emphasize that only a small portion of all diagrams are shown! Although many parts of analytic lattice perturbation theory can be automated with the help of computer codes [34, 32], these are still very difficult and potentially error-prone calculations. Given the central role of perturbative matching in many important phenomenological applications of lattice QCD, other methods are needed.

Perturbation Theory from Monte Carlo Simulations at Weak Coupling

A simpler alternative to analytic perturbation theory, proposed in Ref. [35], is **to simulate the quantity of interest at weak coupling where QCD is perturbative, and fit perturbative expansions to the results**. This alternative approach

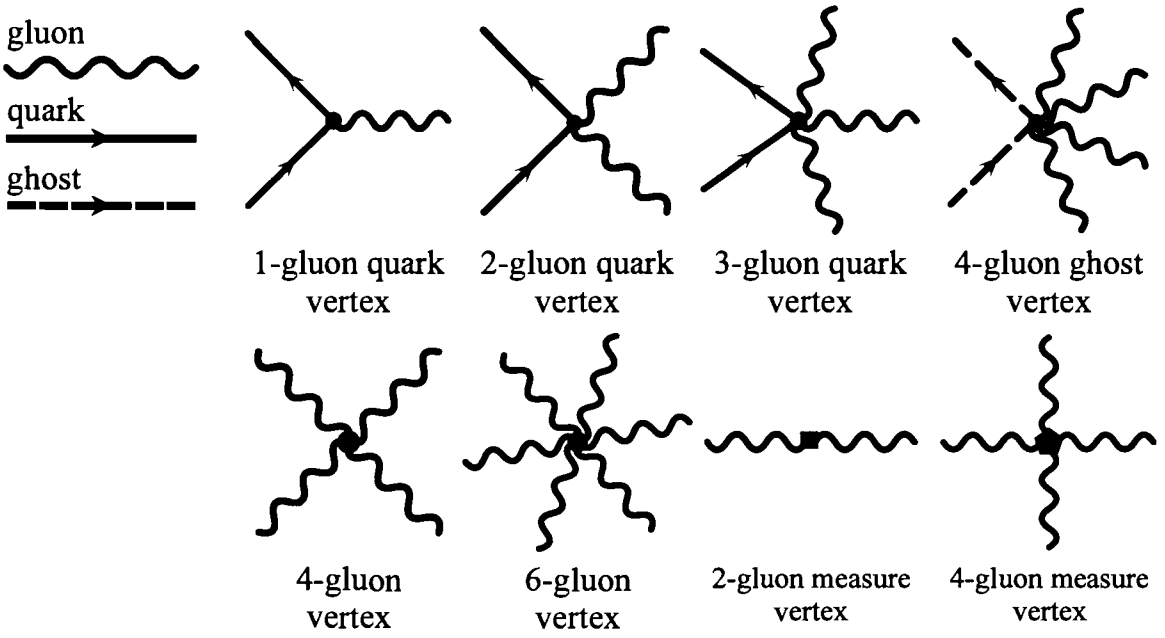

Figure 1.6: Examples of lattice Feynman rules. Note that there is a 6-gluon vertex on the lattice. The group measure in lattice actions also gives new vertices which have no continuum analogue.

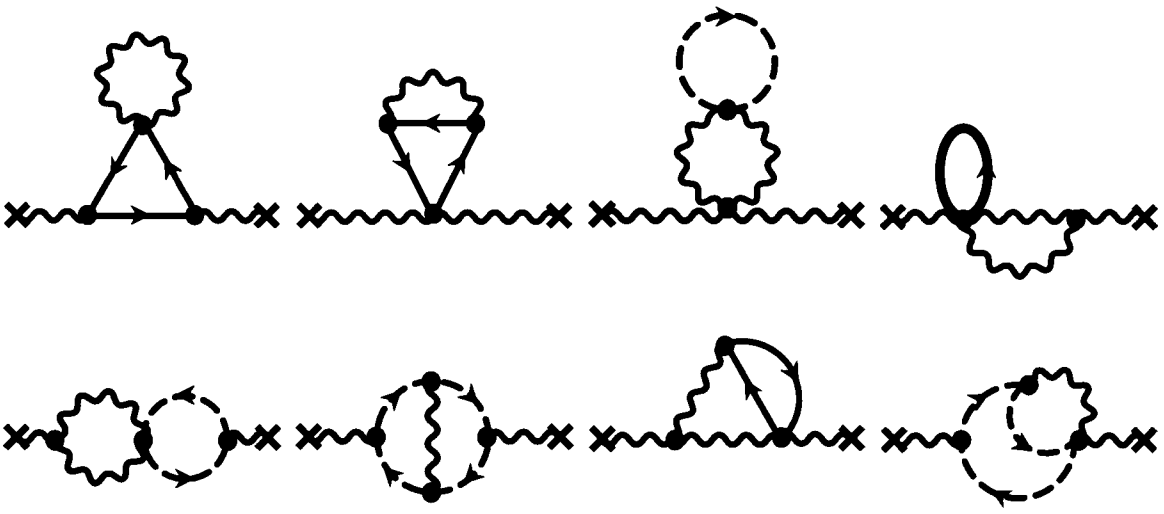

Figure 1.7: Examples of 2-loop diagrams.

to analytic perturbation theory has been successful in reproducing perturbative series for many quantities in pure gauge theory [35, 36, 37, 38], but has never been applied to lattice actions describing a *full* dynamics of QCD. For example the perturbative coefficients of Wilson loops are extracted from Monte Carlo simulations for the Wilson gauge field action (see (2.5)) in Refs. [36, 37]. Results are in excellent agreement, through third order, with the analytic calculation of Ref. [33]. In this project we extend the simulations to include dynamical fermions. In particular, the perturbative series for various small Wilson loops are computed, through third order, for both the unimproved staggered quark action and the Asqtad action [39]. The Asqtad action is currently the most improved action used in dynamical simulations with staggered fermions [10].

This numerical approach produces estimates of higher-order coefficients with far less effort than conventional perturbation theory. One does not have to keep track of the hundreds of diagrams (and to calculate them, of course) in higher-order calculations, but instead simply extracts the perturbative series from simulation data. With the help of constrained curve fitting (see Section 5.4), it is possible to extract the third order coefficients with relatively high accuracy. In fact, by setting the first and second order coefficients to the analytic results of Ref. [33] in the fitting codes, we obtain a *more* precise determination of the third order coefficients, which have smaller statistical errors than those of Ref. [33]. This is a major contribution because to obtain the third order coefficients in conventional perturbation theory requires a very difficult 2-loop calculation.

We should also emphasize that, although we develop our own computer programs in this thesis, simulation codes are publicly available, e.g., the MILC code developed by the MILC collaboration [6]. Hence in principle one does not have to write their programs, and only have to perform the simulations.

The major challenge of the Monte Carlo method is to account for all the possible systematic errors in numerical simulations. This will be discussed in chapter 5. There are three major sources of errors: i) effects of zero momentum modes (or finite size effects), ii) tunneling between the Z_3 center phases, and iii) finite step size error in simulation equations. Twisted boundary conditions are used in the simulations to eliminate the effects of zero momentum modes and to suppress tunneling. A new simulation algorithm, the rational hybrid Monte Carlo algorithm (RHMC) [40], with

[6] Web site: http://physics.indiana.edu/ sg/milc.html.

no finite step size error is employed for the unimproved staggered quark action. This is the first time this algorithm has been used in a numerical application. However the RHMC algorithm is computationally much more expensive and is impractical to apply to highly improved actions such as the Asqtad action. In that case we use the standard R-algorithm [41] and results are extrapolated to zero step size.

Perturbative series of Wilson loops are obtained, through third order, in *full* QCD with improved staggered fermions. Results are in excellent agreement with analytic perturbation theory [33, 32]. **This provides an important cross-check of the perturbation theory input to a recent determination of the strong coupling $\alpha_{\overline{MS}}(M_Z)$ by the HPQCD collaboration** [11, 12, 13].

Finally, we should mention that there is another approach to lattice perturbation theory — the stochastic perturbation theory proposed by Di Renzo *et al.* [42, 43]. This method is based on numerical simulations also, but a perturbative expansion in the coupling g [7] is applied to the simulation equations themselves, which leads to a set of coupled stochastic equations that are truncated at some order in g. Perturbative expansions of Wilson loops, again through third order, have been computed in *full* QCD with *unimproved* Wilson fermions. A comparison on the efficiency of this method and the approach used in the present project was made in Ref [37] for pure gauge theories, which indicates that weak coupling simulations are more favourable. Also it is not clear how difficult to apply this stochastic method to very complex improved actions, such as the Asqtad staggered quark action studied here, since one must explicitly expand the action and the simulation equations in g.

[7] Remember that $g^2 \equiv 4\pi\alpha_s$.

Chapter 2

Lattice QCD

An introduction to lattice QCD will be given in this chapter. The original proposal by Wilson on how to formulate pure gauge theories on a finite size lattice will be reviewed in Section 2.1. In Section 2.2 we will demonstrate the difficulty in including fermion fields on the lattice. We will see that the naïve discretization scheme leads to the so-called "fermion doubling problem" where extra fermionic modes (the "doublers") appear in the continuum limit. Two different approaches to the doubling problem, the staggered quark formulation and overlap fermions, will be presented in Section 2.3. Lattice actions are different from their continuum counterparts because of discretization errors. In the final section of this chapter we will discuss how to construct improved actions which have smaller discretization errors. Many improvement programs will be considered for both gluon and fermion fields. These include classical improvement, tadpole improvement, perturbative improvement and actions constructed with "fat-links".

2.1 Gauge Fields on the Lattice

In this section we concentrate on pure gauge theories, i.e., the first term in the QCD Lagrangian (1.1). The corresponding gauge field action is

$$S = \frac{1}{4}\int d^4x \left(F^a_{\mu\nu}\right)^2 = \frac{1}{2}\int d^4x \,\mathrm{tr}\left(\tilde{F}^2_{\mu\nu}\right) \tag{2.1}$$

where $\tilde{F}_{\mu\nu} = F^a_{\mu\nu}t^a$. To formulate a gauge invariant theory on a lattice with discrete points $x = a(n_1, n_2, n_3, n_4)$, $n_i \in$ integers (see Fig. 2.1), we start with the link variable $U_{x,\mu}$

$$U_{x,\mu} = \mathrm{P}\left\{\exp\left[ig\int_x^{x+a\hat{\mu}} dx^\mu \tilde{A}_\mu(x)\right]\right\}, \tag{2.2}$$

where $\tilde{A}_\mu = A^a_\mu t^a$ and $\mathrm{P}\{\ldots\}$ stands for path-ordered product. Under a local SU(3) transformation defined by (1.5), i.e., $\psi(x) \to V(x)\psi(x) = e^{i\alpha^a(x)t^a}\psi(x)$, the link variable transforms as

$$U_{x,\mu} \to V(x)U_{x,\mu}V(x+\hat{\mu}). \tag{2.3}$$

This can be seen from the fact that $U_{x,\mu}$ acts as a "connection" in the covariant derivative

$$D_\mu\psi = \lim_{a\to 0}\frac{1}{a}\left[\psi(x+\hat{\mu}) - U_{x,\mu}\psi(x)\right] \tag{2.4}$$

in order to compensate for the difference in the phase transformations of $\psi(x)$ and $\psi(x+\hat{\mu})$.

The transformation law (2.3) is very important because it tells us how to construct gauge invariant lattice actions: the trace of any closed loop (Wilson loop) is gauge invariant. In particular, Wilson's [5] original idea is to consider the following action

$$S_W = \beta\sum_{x,\mu\neq\nu}\left(1 - P_{\mu\nu}(x)\right), \quad \beta \equiv \frac{6}{g^2} = \frac{6}{4\pi\alpha_s}, \tag{2.5}$$

where

$$P_{\mu\nu}(x) = \frac{1}{3}\mathrm{ReTr}\left[U_{x,\mu}U_{x+\hat{\mu},\nu}U^\dagger_{x+\hat{\nu},\mu}U^\dagger_{x,\nu}\right] \tag{2.6}$$

is the plaquette located at position x (see Fig. 2.1). This is called the Wilson plaquette action. Expanding (2.2) in powers of the lattice spacing a

$$U_{x,\mu} \xrightarrow[a\to 0]{} e^{iag\tilde{A}_\mu(x)} = 1 + iag\tilde{A}_\mu(x) - \frac{1}{2}a^2g^2\tilde{A}^2_\mu + \mathcal{O}(a^3), \tag{2.7}$$

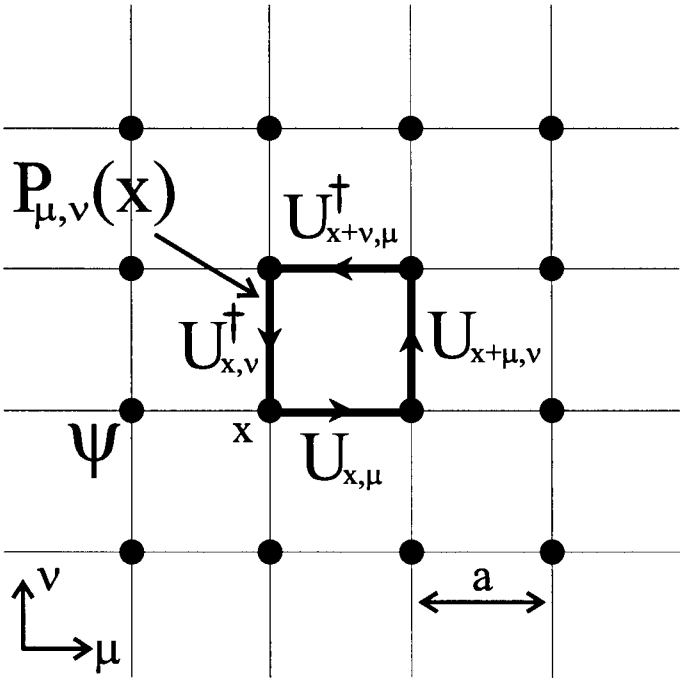

Figure 2.1: QCD on the lattice. Fermions live on the lattice sites and gauge fields $\tilde{A}_\mu(x)$ become the link variables $U_{x,\mu}$ on the lattice. The plaquette $P_{\mu\nu}(x)$ is the product of link variables around the square located at x.

and substituting the result into (2.5), one can check that the Wilson plaquette action reduces to the continuum action as $a \to 0$ with errors of $\mathcal{O}(a^2)$

$$\begin{aligned} S_W &= \beta \sum_{x,\mu\neq\nu} (1 - P_{\mu\nu}(x)) \\ &\xrightarrow[a\to 0]{} \frac{1}{2}\int d^4x \,\mathrm{tr}\left(\tilde{F}^2_{\mu\nu}\right) + \mathcal{O}(a^2). \end{aligned} \tag{2.8}$$

2.2 Fermions on the Lattice — The "Doubling" Problem

The inclusion of fermions on the lattice is complicated by the "doubling" problem. The problem is apparent even for free quarks so let us begin with the *free* continuum Dirac action

$$S = \int d^4x \bar{\psi} \left(\gamma^\mu \partial_\mu + m\right) \psi. \tag{2.9}$$

On the lattice, the derivative is replaced by a finite difference with $\mathcal{O}(a^2)$ errors [1]. This gives the so-called *free* "naïve" quark action

$$S_{\text{naïve}} = \sum_x \left(\bar{\psi}(x) \sum_\mu \gamma^\mu \frac{\psi(x+\hat{\mu}) - \psi(x-\hat{\mu})}{2} + m\bar{\psi}(x)\psi(x) \right). \tag{2.10}$$

The problem for this naïve discretization scheme is that $S_{\text{naïve}}$ describes more than one quark flavour, 16 in total in 4-dimensions, in the continuum limit when $a \to 0$. This can be easily seen in momentum space

$$S_{\text{naïve}} \xrightarrow[\text{Fourier}]{} \sum_\mu \int_{-\pi/a}^{\pi/a} \frac{d^4p}{(2\pi)^4} \bar{\psi}(p) G(p)^{-1} \psi(p), \tag{2.11}$$

where $G(p)$ is the quark propagator

$$G(p) = \left[\sum_\mu i\gamma^\mu \tilde{p}_\mu + m \right]^{-1}, \quad \tilde{p}_\mu = \frac{1}{a} \sin a p_\mu. \tag{2.12}$$

Note that the momentum is allowed to have any value between $-\pi/a$ to π/a, i.e., the first Brillouin zone. Since the sine-function vanishes in the corners of the Brillouin zone, there exists 16 regions in momentum space, $\zeta \approx (0,0,0,0)$, $(\frac{\pi}{a},0,0,0)$, $(\frac{\pi}{a},\frac{\pi}{a},0,0)$, ..., where $G(p)$ is non-zero when $a \to 0$. For $p_\mu \approx 0$, we have

$$\frac{1}{a} \sin a p_\mu \approx p_\mu, \tag{2.13}$$

and for $p_\mu \approx \frac{\pi}{a}$,

$$\frac{1}{a} \sin a p_\mu = \frac{1}{a} \sin \left[a \left(\frac{\pi}{a} - p'_\mu \right) \right] \approx p'_\mu, \tag{2.14}$$

where $p'_\mu = \frac{\pi}{a} - p_\mu$ is again a small momentum. Therefore the propagator splits up into 16 pieces in the continuum limit, labeled by 16 ζ's, and the naïve quark action describes 16 fermion species in this limit. The mode with $\zeta \approx (0,0,0,0)$ is the usual low energy mode and $\zeta \approx (\frac{\pi}{a},0,0,0)$, $(\frac{\pi}{a},\frac{\pi}{a},0,0)$, ..., give the "doublers". These modes have **very large momentum on the lattice** ($p_\mu \approx \frac{\pi}{a}$, the maximum on the lattice) **but behave like a low energy mode**. Since the number of degrees of freedom doubles for each additional dimension, this is called the "doubling" problem.

[1] The leading error can be checked by using Taylor's theorem (take $\mu = 1$): $\psi(x+a) - \psi(x-a) = 2a\partial_x\psi(x) + \mathcal{O}(a^3)$ so that $(\psi(x+a) - \psi(x-a))/2a = \partial_x\psi(x) + \mathcal{O}(a^2)$.

2.3 Staggered Fermions and Overlap Fermions

There are many solutions to the fermion doubling problem. Two different approaches will be presented: staggered fermions [44] and overlap fermions [45, 46]. Another popular discretization scheme which has no doubler modes is Wilson fermions [47]. We will not, however, discuss this method here. Each formulation has its own advantages and disadvantages in terms of computational time and chiral properties. A comparison will be given at the end of this section.

Staggered Fermions

In the staggered quark discretization scheme [44, 22], **one accepts fermion doubling and identifies the excess fermions with other fermion degrees of freedom such as quark flavours**. This unconventional way to introduce quark flavours has surprising phenomenological consequences as we will see below.

The naïve quark action might be fine if there were 16 flavours of quarks in Nature. The number of flavours is reduced to 4 in the staggered quark formulation. This is accomplished by "spin-diagonalizing" the naïve action [48]. Consider the local transformation

$$\psi(x) \to \Omega(x)\psi(x), \quad \bar{\psi}(x) \to \bar{\psi}\Omega^\dagger(x), \quad \Omega(x) \equiv \prod_\mu (\gamma^\mu)^{x_\mu}. \tag{2.15}$$

Note that there are only 16 Ω's because $(\gamma^\mu)^2 = \mathbb{I}$ ($\mathbb{I}$ is the identity matrix in spinor space). The Ω matrices have the following properties

$$\begin{aligned} \Omega^\dagger(x)\Omega(x) &= \mathbb{I}, \\ \Omega^\dagger(x)\gamma^\mu\Omega(x \pm \hat{\mu}) &= (-1)^{x_1+\ldots+x_{\mu-1}}\mathbb{I} \equiv \eta_\mu(x)\mathbb{I}. \end{aligned} \tag{2.16}$$

Applying this transformation to $S_{\text{naïve}}$ given in (2.10), we obtain

$$S_{\text{naïve}} \xrightarrow[\text{spin diag.}]{} \sum_x \left(\bar{\psi}(x) \sum_\mu \eta_\mu(x)\mathbb{I} \frac{\psi(x+\hat{\mu}) - \psi(x-\hat{\mu})}{2} + m\bar{\psi}(x)\mathbb{I}\psi(x) \right). \tag{2.17}$$

The last result is diagonal in spinor space, i.e., the transformation "spin-diagonalizes" the naïve action! This makes each spinor component of ψ equivalent to every other

component. The staggered quark action is obtained by keeping only one spinor component. This effectively reduces the number of degrees of freedom from 16 to 4. Define χ to be the remaining component (χ now carries colour index only), the staggered quark action S_{sf} reads

$$S_{sf} = \sum_{x,y} \bar{\chi}(x) M^{sf}_{x,y}(U) \chi(y) = \sum_{x,y} \bar{\chi}(x) \left(m\delta_{x,y} + D^{sf}_{x,y}(U) \right) \chi(y), \tag{2.18}$$

where $D^{sf}_{x,y}(U)$ is the staggered Dirac operator

$$D^{sf}_{x,y}(U) = \frac{1}{2} \sum_{\mu} \eta_{\mu}(x) \left(U_{x,\mu} \delta_{x,y-\hat{\mu}} - U^{\dagger}_{x-\hat{\mu},\mu} \delta_{x,y+\hat{\mu}} \right). \tag{2.19}$$

We have put back the quark-gluon interactions by inserting the link variables. Therefore if one interprets the fermionic degrees of freedom as quark flavours, the staggered quark action describes 4 equivalent quark species in the continuum limit, i.e., an SU(4) flavour symmetry. The action (2.18) has the same structure as the naïve quark action and hence the leading discretization errors are of $\mathcal{O}(a^2)$, the same as that of $S_{\text{naïve}}$.

Two technical points should be mentioned before we further discuss the properties of staggered fermions. First, the representation (2.18) is not convenient for numerical simulations because χ, being a fermion field, contains Grassmann variables. To transform to a complex-valued field ϕ (again, ϕ has colour index only) which is easy to implement on computers, we notice that in the path integral formulation the contribution of fermions to the partition function is

$$\begin{aligned} \int D\bar{\chi} D\chi e^{-S_{sf}} &= \int D\bar{\chi} D\chi e^{-\bar{\chi} M^{sf} \chi} \\ &= \det M^{sf} \\ &= \int D\phi D\phi^* e^{-\phi^* \left[(M^{sf})^{\dagger} M^{sf} \right]^{-1} \phi}. \end{aligned} \tag{2.20}$$

Consequently, the following effective action is always used in simulations

$$S_{sf} = \sum_{x,y} \phi^{\dagger}(x) \left[(M^{sf})^{\dagger} M^{sf} \right]^{-1}_{x,y} (U) \phi(y) \tag{2.21}$$

where ϕ is a complex vector.

Secondly, the discretization scheme described above automatically fixes the number of quark flavours to be 4. It would then be helpful if it is possible to simulate staggered fermions with arbitrary number of flavours n_f. This can be achieved by taking the $n_f/4$-root of the determinant

$$\left[\det M^{sf}\right]^{n_f/4} = \int D\phi D\phi^* e^{-\phi^* \left[(M^{sf})^\dagger M^{sf}\right]^{-n_f/4} \phi} \tag{2.22}$$

so that the action

$$S_{sf} = \sum_{x,y} \phi^\dagger(x) \left[(M^{sf})^\dagger M^{sf}\right]^{-n_f/4}_{x,y} (U)\phi(y) \tag{2.23}$$

describes n_f quark flavours. In particular, $\sqrt{\det M^{sf}}$ is required for $n_f = 2$, which would be suitable for simulations where only the dynamics of the two lightest quarks, u and d, are considered. How to incorporate the $n_f/4$-root into simulation equations will be discussed in Section 4.2. This procedure of taking the fourth-root (or the $n_f/4$-root) of the determinant raises questions on the locality of the action [49, 50]. The search for a theoretical verification of the "fourth-root trick" is currently an active research area [51, 52]. We will not discuss this issue in this project. However, we want to emphasize that this prescription of staggered quarks is able to produce results which agree with experimental data at the few percent level [10]. In Chapter 6 we will also see that simulations, done with the 12th-root of the determinant, agree order by order with perturbation theory.

Staggered Fermions – Flavour-Changing Interactions and Chiral Symmetry

The staggered quark fields are represented by one-component complex vectors on the lattice. This makes staggered fermions relatively inexpensive for dynamical simulations (see Table 2.1). The unusual identification of doubler modes as quark flavours, however, complicates the interpretation of staggered quark simulations.

Flavour-changing interactions. The staggered quark action describes 4 equivalent quark flavours in the continuum limit. This symmetry is broken on the lattice by flavour-changing interactions. Since doubler modes are interpreted as quark flavours, if a low-energy quark absorbs momentum close to $(\frac{\pi}{a}, 0, 0, 0)$, $(0, \frac{\pi}{a}, 0, 0)$, ..., it will not be driven far off energy shell but instead will turn into a low-energy quark of another

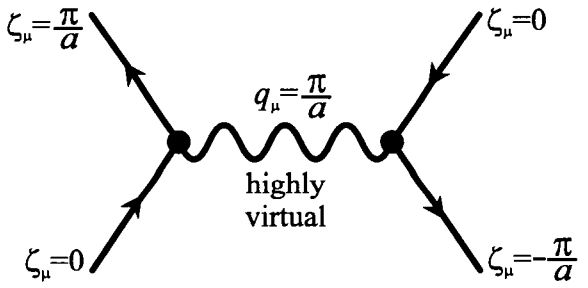

Figure 2.2: Flavour-changing interactions. A low-energy quark that absorbs momentum $q_\mu \approx \frac{\pi}{a}$ will turn to a low-energy quark of another flavour.

flavour. The simplest process of this kind is one-gluon exchange (see Fig. 2.2). The gluon emitted has momentum $q^2 \approx \left(\frac{\pi}{a}\right)^2$ so it is highly virtual. Hence flavour-changing interactions are extremely short range, which allows their effects to be analyzed in perturbation theory. This will be discussed in the next section.

We have already seen that flavour-changing effects cause the eigenvalues of the staggered Dirac operator to move away from zero when $a \neq 0$. Another phenomenological consequence is the mass splitting of the pion multiplets in the chiral sector.

Chiral Symmetry. The spinor structure of the original fermion fields is hidden in the staggered quark formulation. Hence one can anticipate that not all the continuum γ_5-symmetries, (1.9) and (1.10), will be reproduced on the lattice with staggered fermions. In fact, only the $[\mathrm{U}(1)]_A$ symmetry is protected: when the quark masses are equal to zero, S_{sf} is invariant under the following global transformation

$$\chi(x) \to e^{i\epsilon(x)}\chi(x), \quad \bar{\chi}(x) \to e^{i\epsilon(x)}\bar{\chi}(x) \tag{2.24}$$

where $\epsilon(x) \equiv (-1)^{x_1+x_2+x_3+x_4}$. This remnant symmetry is equivalent to

$$\{\epsilon(x), D^{sf}\} = 0. \tag{2.25}$$

Notice the difference between this anti-commutation relationship and the one for the continuum Dirac operator $\{\gamma^5, D\} = 0$, see (1.6). The spontaneous breaking of this symmetry results in a true Goldstone mode with $m_G = 0$ in the zero quark mass limit.

On the other hand, the $[\mathrm{SU}(4)]_A$ symmetry is explicitly broken by flavour-changing interactions. As a result the 15 pions, associated with the spontaneous breaking of the SU(4) flavour symmetry in the continuum limit, are no longer degenerate, and

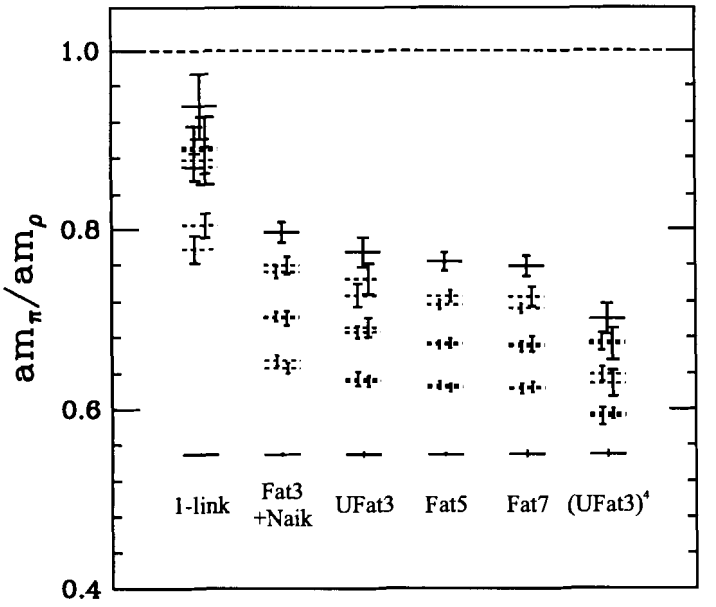

Figure 2.3: The pion mass spectrum. The 16 pions are no long degenerate on the lattice. They organize themselves into five multiplets. The π masses were measured in units of m_ρ, the mass of the ρ meson, and results were normalized with respect to the lowest state, i.e., the Goldstone mode. See Ref. [54] for more details on the calculation. The splitting between the various multiplets reduces substantially when improved operators are used.

their masses do not vanish even when the quark masses are equal to zero. However, because of the $[\mathrm{U}(1)]_A$ symmetry, $m_\pi^2 = \mathcal{O}(a^2)$ in the chiral limit [53], i.e., there is no additive mass renormalization. In contract the pions acquire a **finite** mass shift even when $m = 0$ for Wilson-type quarks [22], and one has to tune the bare quark masses to obtain massless pions. This makes dynamical simulations very expensive for Wilson fermions at small quark masses (see summary of this section).

The cubic symmetry of the lattice suggests that the 15 pions should form 4 degenerate multiplets [53]. Fig. 2.3 shows the pion spectrum obtained in Ref. [54]. Many staggered quark actions were considered. Here we only have to look at the "1-link" results, which were computed using the standard staggered quark action (2.21). We will discuss the other results in the next section. The data clearly shows that the pions organize themselves into 4 multiplets, together with the true Goldstone mode associated with the breaking of $[\mathrm{U}(1)]_A$.

The Overlap Fermions

Staggered quark formulation lacks exact chiral symmetry. Only a remnant of the symmetry is realized by the staggered quark action. We are now going see how the continuum chiral symmetry can be restored, as least partially, on the lattice.

We have seen that chiral invariance requires $\{\gamma^5, D\} = 0$, see (1.6). In Ref. [27], Ginsparg and Wilson suggested to replace the continuum anti-commutation relation with the following criterion on the lattice

$$\{\gamma^5, D\} = aD\gamma^5 D, \tag{2.26}$$

i.e., the condition for the right-hand-side to vanish is relaxed to a term of $\mathcal{O}(a)$, but the relation $\{\gamma^5, D\} = 0$ is recovered in the continuum limit. This is known as the Ginsparg-Wilson relation. Later on, Lüscher showed that any operator that satisfies (2.26) induces a continuous symmetry on the lattice which can be interpreted as the continuum chiral symmetry [28]. Let us consider the following global transformation

$$\psi \to e^{i\theta\gamma^5(1-\frac{aD}{2})}\psi \approx \left[1 + i\theta\gamma^5(1 - \frac{aD}{2})\right]\psi. \tag{2.27}$$

It is not difficult to check that the usual chiral Lagrangian (i.e., zero quark masses), $\bar{\psi}D\psi$, is invariant under (2.27) if D satisfies the Ginsparg-Wilson relation

$$\begin{aligned}
\bar{\psi}D\psi &\to \bar{\psi}\left[1 + i\theta(1 - \frac{aD}{2})\gamma^5\right] D \left[1 + i\theta\gamma^5(1 - \frac{aD}{2})\right]\psi \\
&\approx \bar{\psi}D\psi + i\theta\bar{\psi}\left[(1 - \frac{aD}{2})\gamma^5 D + D\gamma^5(1 - \frac{aD}{2})\right]\psi \\
&\approx \bar{\psi}D\psi + i\theta\bar{\psi}\left[\gamma^5 D + D\gamma^5 - aD\gamma^5 D\right]\psi \\
&= \bar{\psi}D\psi.
\end{aligned} \tag{2.28}$$

The same is also true if we consider axial-vector transformation.

The Ginsparg-Wilson relation not only gives a precise definition of chiral symmetry on the lattice but also indicates how the Dirac operator should be constructed. Unfortunately, it is not until recently that a solution of (2.26) has been found. In 1998, Neuberger [45, 46] showed that the following operator, called the overlap Dirac

operator [2], satisfies the Ginsparg-Wilson relation

$$D^{ov} = 1 + \gamma^5 \epsilon(H), \tag{2.29}$$

where $\epsilon(H)$ is the matrix sign function

$$\epsilon(H) = \frac{H}{|H|}. \tag{2.30}$$

A popular choice for the kernel H is the Hermitian Wilson Dirac operator [22], $H \equiv \gamma^5 D^{Wf}$, with

$$D^{Wf}_{x,y} = \delta_{x,y} - \kappa \sum_{\mu} \left[(1 - \gamma_\mu) U_{x,\mu} \delta_{x,y-\hat{\mu}} + (1 + \gamma_\mu) U^{\dagger}_{y,\mu} \delta_{x,y+\hat{\mu}} \right]. \tag{2.31}$$

where κ is called the hopping parameter. To avoid fermion doubling κ has to be appropriately adjusted. A detail description of how κ must be chosen can be found in Refs. [55, 56, 57]. The overlap action is

$$S_{ov} = \sum_{x,y} \bar{\psi}(x) M^{ov}_{x,y} \psi(y) = \sum_{x,y} \bar{\psi} \left[m\delta_{x,y} + D^{ov}_{x,y} \right] \psi(y). \tag{2.32}$$

It has been shown that the leading discretization errors of S_{ov} are also of $\mathcal{O}(a^2)$ [58].

In practice, the sign function can be implemented using the optimal rational approximation (l-order Zolotarev expansion) [59]

$$\epsilon(H) \simeq H \cdot \sum_{i}^{l} \frac{c_i}{H^{\dagger}H + b_i} \tag{2.33}$$

where b_i and c_i are constants. Because each term in the expansion requires an inversion of $H^{\dagger}H$, a very large matrix [3], computational cost for overlap fermions is many order of magnitudes larger than the other formulations.

[2] It is called the "overlap" operator because the operator is originally written as an overlap of two state vectors in an auxiliary 5-dimensional space-time. We will not go into the details of the derivation but rather simply adopt the definition presented here.

[3] The matrix $H_{x,y} = \gamma^5 D^{Wf}_{x,y}$ has dimensions $4n_c N \times 4n_c N$, where n_c is the number of colours and N is the total number of lattice sites which is usually of $\mathcal{O}(10^4)$.

Action	Cost	Chiral Symmetry	Anti-commutation Relation	Leading Errors
Staggered	1	a remnant	$\{\epsilon(x), D^{sf}\} = 0$	$\mathcal{O}(a^2)$
Wilson	10	explicitly broken	$(D^{Wf})^\dagger = \gamma^5 D^{Wf} \gamma^5$	$\mathcal{O}(a)$
Overlap	1000	preserved	$\{\gamma^5, D^{ov}\} = aD\gamma^5 D$	$\mathcal{O}(a^2)$
Continuum	–	exact	$\{\gamma^5, D\} = 0$	–

Table 2.1: Comparison among the various fermion actions. The computational cost is normalized by that of staggered fermions, and comparison is made at the quark masses used in today's dynamical simulations.

Summary

We finish this section by comparing the various discretization schemes, including Wilson fermions, in terms of their chiral properties and computational cost (see Table 2.1). Wilson's ideas on how to construct lattice fermion action that has no doubler modes are explained in Ref. [22].

Chiral Symmetry. Among the three discretization schemes discussed in this section, the overlap action is the only formulation which reproduces a chiral symmetry on the lattice. The overlap Dirac operator satisfies the Ginsparg-Wilson relation, and chiral zero modes exist even at finite lattice spacing. On the other hand, only a remnant of the continuum chiral symmetry is retained in the staggered quark action, and the staggered Dirac operator lacks exact zero modes on the lattice. The chiral symmetry is explicitly broken for Wilson fermions [22].

Computational cost. The advantage that the continuum chiral symmetry is explicitly realized by the overlap action is overshadowed by its high computational cost. In comparison to staggered fermions, dynamical simulation with Wilson fermions is about 10 times slower (because of the spinor structure of the quark field and the presence of exceptional configurations, see next paragraph), and is about 1000 times slower with overlap fermions (because of the many matrix inversions in computing the sign function)! This comparison is made at the values of quark masses used in present-day simulations, where m_u and m_d, the masses of the u and d quarks, are about half of the physical s quark mass. In general the computational cost also depends on the quark masses, and all formalisms exhibit a sharp increase in the cost at small m_u and m_d (a "cost wall"). Simulations therefore are always done at relatively large values of m_u and m_d, and results are extrapolated to the physical quark

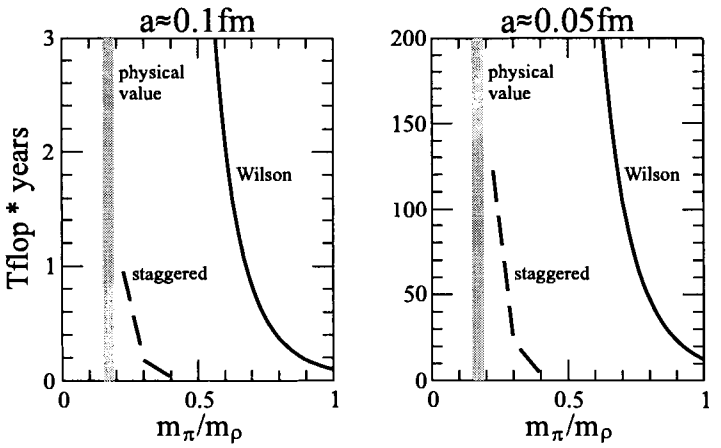

Figure 2.4: The estimated computational cost for dynamical simulations, as a function of m_π/m_ρ, with staggered fermions and Wilson fermions.

masses in post-simulation analysis. Chiral extrapolation, however, is not trivial and introduces fitting errors [60].

This problem is illustrated in Fig. 2.4 (this figure is taken from Ref. [49]), which shows the estimated computational cost for dynamical simulations with staggered fermions and Wilson fermions as a function of m_π/m_ρ (ratio of the π and ρ meson masses). The physical value is at $m_\pi/m_\rho = 0.174$. Results are shown for two lattice spacings, $a \approx 0.1$fm which is the typical value used in today's dynamical simulations, and $a \approx 0.05$fm. One can see that the "cost wall" appears at a much larger value of m_π/m_ρ for Wilson fermions. This is due to the presence of "exceptional configurations" [61], related to the fact that one has to set the bare quark masses at some critical value to obtain massless pions. On the other hand there is no such complication for staggered fermions. The $[\mathrm{U}(1)]_A$ symmetry of the staggered quark action protects the pions from acquiring an additive mass renormalization, and hence one can go deeper toward the chiral limit before the computational cost explodes. Note also the dramatic increase in the cost when the lattice spacing is halved. This reflects the scaling a^{-6} in computational cost mentioned earlier. Improvement of lattice actions, which will be discussed in the next section, therefore becomes very important for small quark masses because it allows simulations to be done on relatively coarse lattices.

The situation for overlap fermions is not clear since dynamical simulations so far have only been done on very small lattices, e.g. 4^4 [62]. On the other hand, it is believed that overlap fermions and staggered fermions become equally efficient at very

small quark masses [63] (perhaps at the physical m_u and m_d), because the overlap action has the correct chiral properties. These values, however, will not be reached in the near future, for both staggered fermions and overlap fermions.

In conclusion, dynamical simulations can now be done at realistically small quark masses with staggered fermions (with improvement), and it is **the only discretization scheme which is capable of delivering accurate simulation results that can be compared with experiments in the near future.**

2.4 Improvement

We have now seen that lattice actions contain discretization errors and lattice artifacts. It is therefore necessary to minimize their effects in order to obtain precise measurements from lattice simulations. This is particularly important when working on coarse lattices with large lattice spacing. In this section several improvement programs will be discussed: classical improvement, tadpole improvement, perturbative improvement and fat-link improvement. Actions used today in dynamical simulations often employ a combination of these improvement methods.

The general idea of improvement is very simple. One adds higher dimensional operators to the original action so to eliminate the leading discretization errors. The analogue of this is the use of a better finite difference in the approximation of the continuum derivative. For example, we can instead use the following approximation in the naïve quark action so the leading errors become $\mathcal{O}(a^4)$

$$\partial_x \psi(x) = \Delta_x \psi(x) - \frac{a^2}{6} \Delta_x^3 \psi(x) + \mathcal{O}(a^4), \tag{2.34}$$

where $\Delta_x \psi(x) = \frac{\psi(x+a) - \psi(x-a)}{2}$ is original finite difference. The coefficients of the additional terms have to be adjusted carefully so that the lattice model reduces back to the continuum theory when $a \to 0$. Perturbative improvement, on the other hand, gives $\mathcal{O}(\alpha_s)$ corrections to these coefficients, which allows short distance physics ($< a$) to be restored at finite lattice spacing.

Classical Improvement

Classical improvement corrects the leading discretization errors in lattice spacing. Consider the improvement of the Wilson plaquette action (2.5) as an example. We

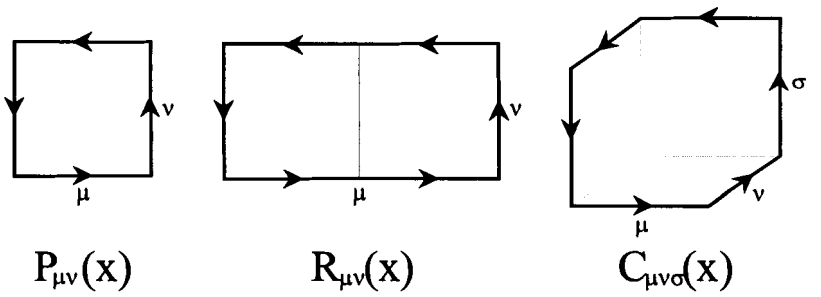

Figure 2.5: Operators used in the improved gluon action: the plaquette $P_{\mu\nu}(x)$, the rectangle $R_{\mu\nu}(x)$ and the cubic chair term $C_{\mu\nu\sigma}(x)$.

have shown that any closed loop on the lattice is gauge invariant and can therefore be used to construct gauge invariant lattice actions. The Wilson action uses the plaquettes and has $\mathcal{O}(a^2)$ errors. An improved action [64] can be obtained by including the next largest loops — the rectangles

$$S_{imp} = \frac{5}{3}\sum_{x,\mu<\nu}(1 - P_{\mu\nu}(x)) + \frac{1}{12}\sum_{x,\mu\neq\nu}(1 - R_{\mu\nu}(x)) \tag{2.35}$$

where $R_{\mu\nu}(x)$ is the trace of the 1×2 rectangle at position x (see Fig. 2.5) [4]. This action has leading errors of $\mathcal{O}(a^4)$, which again can be checked by expanding the link variables in powers of the lattice spacing using (2.7).

Tadpole Improvement

The improved action (2.35) was originally designed to eliminate the $\mathcal{O}(a^2)$ errors in the Wilson plaquette action. Simulations with S_{imp}, however, indicated that improvement in many cases was not as significant as would be expected. The solution of this problem was provided by Lepage and Mackenzie [65]. They showed that quantum corrections that would be suppressed by a^2g^2, suggested from a classical analysis, are actually only suppressed by g^2. To see this, consider the expectation value of the link variables, i.e., the mean link u_0. Taking the average of (2.7), we have

$$u_0 \equiv \frac{1}{3}\mathrm{tr}\langle U_{x,\mu}\rangle_{gf} = \frac{1}{3}\mathrm{tr}\left[1 + iag\langle\tilde{A}_\mu(x)\rangle_{gf} - \frac{1}{2}a^2g^2\langle\tilde{A}^2_\mu(x)\rangle_{gf} + \mathcal{O}(a^3g^3)\right], \tag{2.36}$$

where "gf" stands for gauge fixing. Gauge fixing is necessary because the expectation value of a gauge non-invariant quantity always vanishes in lattice theory [66]. However

[4] Note that the second sum is over rectangles with all possible orientations.

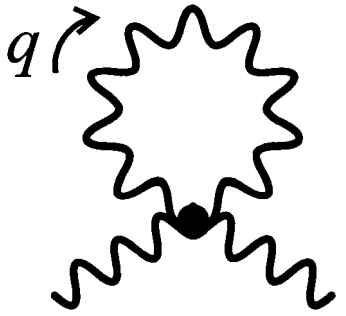

Figure 2.6: Tadpole diagram.

as we will see shortly, this gauge fixing procedure can be eliminated by using a gauge invariant definition of u_0.

Now, the linear term $\langle \tilde{A}_\mu(x) \rangle = \langle A^a_\mu(x) t^a \rangle$ vanishes under the trace because the generators t^a of the colour group are traceless. The last term corresponds to a tadpole diagram, a higher-order quantum correction (see Fig. 2.6). The virtual gluon propagator is $\sim 1/q^2$ where q is the momentum going through the loop. Hence on the lattice the tadpole diagram is proportional to

$$\langle \tilde{A}^2_\mu(x) \rangle \sim \int_{-\pi/a}^{\pi/a} \frac{d^4q}{q^2} \sim a^{-2}. \tag{2.37}$$

Naïvely one would expect the tadpole to be suppressed by $a^2 g^2$. However, since $\langle \tilde{A}^2_\mu \rangle$ is proportional to a^{-2}, it is actually suppressed by g^2 only.

Notice that it is the integration over the high momentum modes $q \approx \pi/a$ of the gluon that gives $\langle \tilde{A}^2_\mu \rangle \sim a^{-2}$. This suggests the possibility of removing these quantum effects by a mean field renormalization of the links

$$U_{x,\mu} \to \frac{U_{x,\mu}}{u_0}. \tag{2.38}$$

To see this, split up the gauge field into a long distance part $A_\mu(x)|_{ir}$ (infrared) and a short distance part $A_\mu(x)|_{uv}$ (ultraviolet): $A_\mu(x) = A_\mu(x)|_{ir} + A_\mu(x)|_{uv}$. This implies that the link variable can be factorized as $U_{x,\mu} = U_{x,\mu}|_{ir} \times U_{x,\mu}|_{uv}$. Since u_0 is short-range, it gives a good approximation to $\langle U_{x,\mu}|_{uv} \rangle$. Therefore division of each link by u_0 removes the short distance fluctuations in the gauge fields and consequently the tadpole effects. Applying this idea to the classically improved gauge field action (2.35),

the tadpole improved version reads

$$S_{imp} = \frac{5}{3}\frac{1}{u_0^4}\sum_{x,\mu<\nu}(1 - P_{\mu\nu}(x)) + \frac{1}{12}\frac{1}{u_0^6}\sum_{x,\mu\neq\nu}(1 - R_{\mu\nu}(x))\,. \tag{2.39}$$

which has leading errors of $\mathcal{O}(a^2 g, a^4)$.

As mention above, computation of $u_0 \equiv \langle U_\mu(x)\rangle_{gf}$ requires gauge fixing because link variables are not gauge invariant objects. An alternative definition of u_0 which does not require gauge fixing is to take the 4th-root of the average plaquette, $u_0 \equiv \langle P_{\mu\nu}(x)\rangle^{1/4}$. Since the plaquette $P_{\mu\nu}(x)$ is the smallest gauge invariant object on the lattice, it also gives a good measure of the ultraviolet quantum fluctuations.

Perturbative Improvement

Lattice provides a hard cutoff in the momentum ($\frac{\pi}{a}$) so lattice models are different from the continuum theories at short distance (less than the lattice spacing). We are now going to present a systematic procedure to add in renormalizations due to contributions from $p > \frac{\pi}{a}$ physics. Tadpole improvement discussed above is the first step to include these short distance effects. In that case the couplings are renormalized by powers of u_0.

Again consider the gauge field action as an example. It has been shown that [64] the most general action that can be constructed from operators up to dimension 6 (6 links) can be expressed as

$$S_{imp} = \beta_{pl}\sum_{x,\mu<\nu}(1 - P_{\mu\nu}(x)) + \beta_{rt}\sum_{x,\mu\neq\nu}(1 - R_{\mu\nu}(x)) + \beta_{cu}\sum_{x,\mu<\nu<\sigma}(1 - C_{\mu\nu\sigma}(x)) \tag{2.40}$$

where $C_{\mu\nu\sigma}$ is the 6-link cubic chair term defined in Fig. 2.5. The improved actions (2.35) and (2.39) are special cases with $\beta_{cu} = 0$. Asymptotic freedom guarantees that we are in the perturbative phase when $p > \frac{\pi}{a}$. Therefore to incorporate the missing short distance ($< a$) physics, the coefficients are tuned (renormalized) in such a way that physical quantities, like scattering amplitudes, computed using lattice perturbation theory match with the analogous quantities in the continuum. The improved action obtained this way should have an overall better resemblance to the continuum theory.

As discussed in the introduction, lattice perturbation theory is done in the same way as continuum perturbation theory using Feynman rule techniques. Analytic per-

turbative theory, however, is very challenging because lattice Feynman rules are generally much more complicated. An alternative method to analytic calculations will be presented in the second part of the thesis. Here we simply report the results without going any further into the details of the matching calculation. To 1-loop order in perturbation theory, the coefficients are given by [67]

$$\beta_{rt} = -\frac{\beta_{pl}}{20u_0^2}\left(1 + 0.4805\alpha_s\right), \quad \beta_{cu} = -\frac{\beta_{pl}}{u_0^2}0.03325\alpha_s, \quad \alpha_s = -\frac{4\ln u_0}{3.0684}, \tag{2.41}$$

where β_{pl} is a free parameter. The leading errors are of order $\mathcal{O}(a^2\alpha_s^2, a^4)$. This 1-loop improved action will be used in the next chapter to generate gauge field configurations.

Fat-link Improvement

The fat-link improvement program [68, 69] was designed to suppress flavour-changing interactions for staggered quarks. The central idea is to suppress the transfer of high momentum gluon ($q_\mu \sim \frac{\pi}{a}$) by "smoothing out" the quark-gluon vertex. To see how this might be done, consider the following replacement of the gauge field [69]

$$A_\mu(x) \to A_\mu(x+\hat{\nu}) + A_\mu(x-\hat{\nu}) + 2A_\mu(x). \tag{2.42}$$

In momentum space, this reads

$$A_\mu(q) \to \frac{1}{4}\left(e^{iaq_\nu} + e^{-iaq_\nu} + 2\right)A_\mu(q) = \frac{1}{4}\left(2\cos aq_\nu + 2\right)A_\mu(q). \tag{2.43}$$

It reduces back to $A_\mu(q)$ for low momentum transfer $q_\nu \approx 0$. On the other hand the right hand side vanishes when a single gluon with momentum $q_\nu \approx \frac{\pi}{a}$ is extracted. Hence this removes quark-gluon coupling with momentum close to $\frac{\pi}{a}$ in the ν-component. To eliminate contributions from other q's, $(\frac{\pi}{a},0,0,0)$, $(0,\frac{\pi}{a},0,0)$, ..., one simply applies (2.43) to all directions. This suggests the use of "fat-links" in the staggered operator (see Fig. 2.7)

$$\begin{aligned} U_{x,\mu} &\to c_1 U_{x,\mu} \\ &+ w_3 \sum_{\nu\neq\mu}\left[U_{x,\nu}U_{x+\hat{\nu},\mu}U^\dagger_{x+\hat{\mu},\nu} + U^\dagger_{x-\hat{\nu},\nu}U_{x-\hat{\nu},\mu}U^\dagger_{x-\hat{\nu}+\hat{\mu},\nu}\right]. \end{aligned} \tag{2.44}$$

The coefficients c_1, w_3 can be determined from the classical and perturbative improvement schemes described earlier. The staggered quark action that employs this

replacement is called "Fat3" because neighboring sites are connected by 3-link staples. This idea can be extended to include staples with more links [31, 70]

$$U_{x,\mu} \to c_1 U_{x,\mu} + \sum_{\nu} \left[w_3 S^{(3)}_{\mu\nu}(x) + \sum_{\rho} \left(w_5 S^{(5)}_{\mu\nu\rho}(x) + \sum_{\sigma} w_7 S^{(7)}_{\mu\nu\rho\sigma}(x) \right) \right], \qquad (2.45)$$

where $S^{(3)}$, $S^{(5)}$, $S^{(7)}$ are the 3-staples, 5-staples and 7-staples respectively

$$\begin{aligned} S^{(3)}_{\mu\nu}(x) &= U_\nu(x) U_\mu(x+\hat{\nu}) U^\dagger_\nu(x+\hat{\mu}), \\ S^{(5)}_{\mu\nu\rho}(x) &= U_\nu(x) S^{(3)}_{\mu\rho}(x+\hat{\nu}) U^\dagger_\nu(x+\hat{\mu}), \\ S^{(7)}_{\mu\nu\rho\sigma}(x) &= U_\nu(x) S^{(5)}_{\mu\rho\sigma}(x+\hat{\nu}) U^\dagger_\nu(x+\hat{\mu}). \end{aligned} \qquad (2.46)$$

The action constructed using $S^{(3)}$ and $S^{(5)}$ is called "Fat5", and the "Fat7" action includes all staples up to 7 links. Finally, one can also add a 3-link coupling (the Naik term), and another 5-link staple similar to $S^{(5)}$ but with $\nu = \rho$ (the Lepage term) to the action. This gives the "Asq" action. The tadpole improved version is called the "Asqtad" action. This is the most improved staggered quark action used in today's dynamical simulations of QCD [10]. The path coefficients for the various improved staggered quark actions are listed in Table 2.2.

A good way to see how effective these fat-link improved actions are in flavour symmetry restoration is to study the level of pion mass splitting (see Fig. 2.3 on P. 27). Clearly the levels are less spread out when improved actions are used. Results also indicate that the splitting becomes smaller as the links get "fatter", e.g., Fat5 $\to$ Fat7. The Asqtad operator was studied in Ref. [39] and even less flavour-symmetry breaking effect was observed.

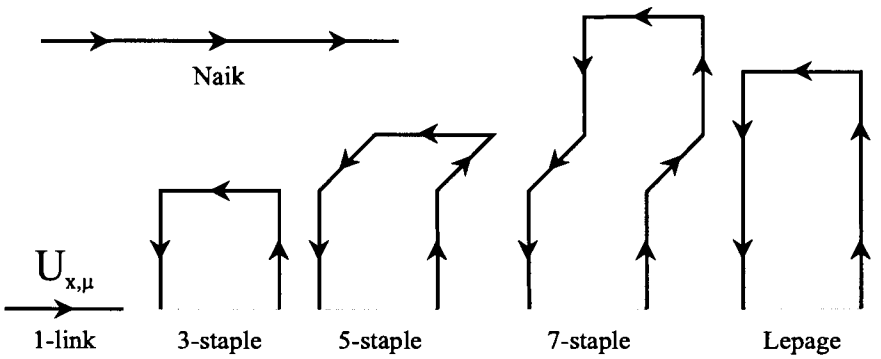

Figure 2.7: Paths used in fat-link improved staggered quark actions.

Action	Link	3-staple	5-staple	7-staple	Lepage	Naik
	c_1	w_3	w_5	w_7	w_{lp}	c_3
1-link (unimp)	1	0	0	0	0	0
Fat3+Naik	$\frac{9}{32}$	$\frac{9}{64}$	0	0	0	$-\frac{1}{24}$
Fat5	$\frac{1}{7}$	$\frac{1}{14}$	$\frac{1}{56}$	0	0	0
Fat7	$\frac{1}{8}$	$\frac{1}{16}$	$\frac{1}{64}$	$\frac{1}{384}$	0	0
Asq	$\frac{5}{8}$	$\frac{1}{16}$	$\frac{1}{64}$	$\frac{1}{384}$	$\frac{-1}{16}$	$\frac{-1}{24}$
Asqtad	$\frac{5}{8u_0}$	$\frac{1}{16u_0^3}$	$\frac{1}{64u_0^5}$	$\frac{1}{384u_0^7}$	$\frac{-1}{16u_0^5}$	$\frac{-1}{24u_0^3}$

Table 2.2: Path coefficients for the various improved staggered quark actions [39].

Further Improved Staggered Quark Action

It has been found that further improvement is possible with multiple fattening using *unitarized* fat-links [71], i.e., the fat-links [5] are projected back to the SU(3) group manifold before they are used in the next fattening process. An example is the improved Asq action $(\text{UFat7})^n \times \text{Asq}$

$$(\text{UFat7})^n \times \text{Asq} \equiv \text{Asq} \times \underbrace{\ldots \left(\text{Proj}_{SU(3)} \times \text{Fat7}\right) \times \left(\text{Proj}_{SU(3)} \times \text{Fat7}\right)}_{n \text{ times}} \qquad (2.47)$$

where the order of operations is from right to left and $\text{Proj}_{SU(3)}$ labels SU(3) reunitarization.

Another class of actions which use *unitarized* fat-links are the HYP-improved (hypercubic blocking) staggered quark actions [72]. In this case only those links within the hypercube containing the original link are included in the fattening process.

These improved actions were studied in Ref. [73]. Results are given in Fig. 2.8 where the mass square difference between the multiplets and the Goldstone pion is plotted. It can be observed that the splitting is reduced considerably with the UFat7 $\times$ Asq and the HYP operator. Additionally, results seem to indicate that improvement using UFat7 links or hypercubic blocking are equally efficient in suppressing flavour-changing effects.

From (2.47) one can see that unitarized fat-link actions generally have very complicated structure. Also to derive simulation algorithms we need $\frac{\partial S}{\partial U}$ (see Section 5.3). However the standard iterative method for SU(3) reunitarization [74] is not differentiable hence an alternative implementation of $\text{Proj}_{SU(3)}$ is required. All these make

[5] Fat-links are not SU(3) elements because the sum of two SU(3) matrices is not an SU(3) matrix.

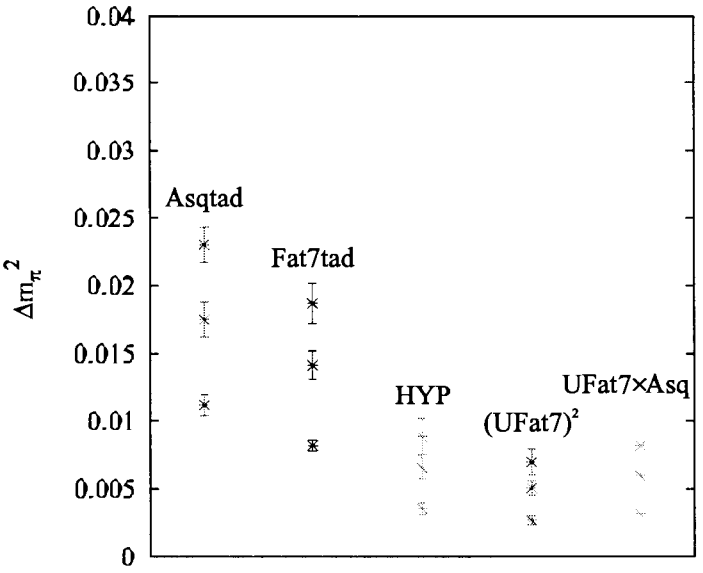

Figure 2.8: Pion spectrum computed using *unitarized* fat-link operator. The mass squared difference, i.e., $a^2\Delta m_\pi^2 \equiv a^2(m_\pi^2 - m_G^2)$, between the higher multiplets (m_π^2) and the Goldstone pion (m_G^2) is shown. Results are taken from Ref. [73].

code development for dynamical simulations very difficult. Until now only one group has successfully performed dynamical simulations with unitarized fat-link actions [75]. The study, however, used a relatively simple action (containing 3-staples only). We have developed computer codes for the $(UFat7)^n \times$ Asq action. Some test runs were also done on 4^4 lattices [76]. Given the success of the Asqtad action, which has been shown to reproduce results that agree with experimental data at the few percent level (see for example Ref. [10]), the next step certainly is to do full QCD simulations with the UFat7×Asq action or the HYP-improved action. Our computer program, although is not used in this project, is the first step toward this goal. A short summary of how to incorporate the reunitarization step into the simulation equations is given in Appendix A.

Figures 2.3 and 2.8 show that flavour-symmetry breaking lattice artifacts can be strongly suppressed by using improved staggered operators. Since flavour-changing effects also cause the continuum zero modes to spread out when $a \neq 0$ and make the index theorem invalid for staggered fermions on the lattice, it is interesting to study how improvement in staggered quark operator affects the distribution of the low-lying eigenmodes. This is the subject of the next chapter.

Chapter 3

QCD Topology and Spectral Properties of the Staggered Dirac Operator

A systematic study of the spectral properties of a variety of improved staggered operators is presented in this chapter. Previous studies showed that the index theorem cannot be reproduced by the *unimproved* staggered operator on the *coarse* lattices because the operator has no, not even approximate, zero eigenvalues. This problem was further revealed in comparisons of the distribution of the small eigenmodes obtained in simulations with the predictions of Random Matrix Theory (RMT). The eigenvalue spectrum in all topological sectors was found to be consistent with the prediction of RMT for topological charge equal to zero. Therefore it is conventional wisdom that staggered fermions do not feel gauge field topology.

Many systematic effects on the spectral properties have been considered in this thesis. These include i) improvement in the staggered operator, ii) improvement in the gauge field action, iii) lattice spacing, and iv) lattice volume. It has been observed that eigenmodes with small eigenvalue and large chirality appear as the level of improvement increases. These small eigenmodes can be identified as the "zero modes" associated with the topology of the background gauge field. This indicates that **lattice artifacts and discretization errors are responsible for the failure of the *unimproved* operator to show the proper topological properties.** We have also compared the distribution of the remaining nonchiral modes against the predictions of RMT. Excellent agreement is obtained not only for the zero charge

sector but for $Q = 1$, 2 also.

This chapter is organized as follows. An informal derivation of the index theorem will first be presented in the next section. Application of RMT to QCD Dirac spectrum will be reviewed in Section 3.2. In Section 3.3, we will discuss previous simulation results and explain why the *unimproved* operator did not see gauge field topology in these studies. We will argue that the correct topological properties should be reproduced if one uses *improved* operators. Details of the simulations will be given in Section 3.4 and results will be presented in Section 3.5.

3.1 The Index Theorem

An informal derivation of the index theorem is given in this section. We will follow the proof presented in Ref. [18]. The index theorem states that, when *massless* fermions couple to a gauge field with nontrivial topology, some of the eigenvalues of the corresponding Dirac operator D necessarily vanish ((1.17) repeated here)

$$Q = \text{index}(D) \equiv n_R - n_L, \tag{3.1}$$

where Q is the topological charge of the background gauge field and n_L, n_R are the numbers of zero eigenmodes of D with -1, +1 chirality.

For simplicity, let us prove the theorem in QED (Euclidean). We will also approach the *massless* case by starting with a *massive* (mass m) Dirac field. In this case the chiral symmetry $[\text{U}(1)]_A$ is explicitly broken and the axial current (1.14) acquires a new source term $-2m\bar{\psi}(x)\gamma^5(x)\psi$ additional to the topological charge density $Q(x)$ of the gauge field [1]

$$\partial_\mu J^{\mu 5}(x) = -2m\bar{\psi}(x)\gamma^5\psi(x) - 2Q(x). \tag{3.2}$$

Integrating over the entire 4-dimensional space-time and assuming that $J^{\mu 5}(x) \to 0$ at infinity, we have

$$Q = m\int d^4x\bar{\psi}(x)\gamma^5\psi(x). \tag{3.3}$$

[1]The reason why there is an extra factor of 2 multiplying the charge density $Q(x)$ is that, in QED, the topological charge is $Q = -\frac{e^2}{16\pi^2}\int d^4x\epsilon^{\mu\nu\rho\sigma}F_{\mu\nu}F_{\rho\sigma}$, while the QCD formula (1.13) has an extra factor of $1/2$ ($n_f = 1$) which comes from taking the trace of the colour matrices.

Taking the expectation value of the above equation gives

$$Q = m \int d^4x \langle \bar{\psi}(x)\gamma^5\psi(x)\rangle, \tag{3.4}$$

where

$$\langle \bar{\psi}(x)\gamma^5\psi(x)\rangle = \frac{\int D\psi(y)D\bar{\psi}(y)\left(\bar{\psi}(x)\gamma^5\psi(x)\right)e^{-S}}{\int D\psi(y)D\bar{\psi}(y)e^{-S}}, \tag{3.5}$$

and

$$S = \int d^4y\bar{\psi}(y)\left(D+m\right)\psi(y) \tag{3.6}$$

is the Euclidean QED action. Notice that ψ, $\bar{\psi}$ are the only dynamical variables so $\langle Q\rangle = Q$. We want to show that the right hand side of (3.4) reduces to $n_R - n_L$. To proceed, expand the Grassmann fields ψ, $\bar{\psi}$ in the eigen-basis of the *massless* Dirac operator D

$$\psi(x) = \sum_r a_r f_r, \quad \bar{\psi}(x) = \sum_r \bar{a}_r \bar{f}_r \tag{3.7}$$

where a_r, $\bar{a}_r$ are Grassmann numbers and f_r are orthonormal eigenfunctions of D with eigenvalues λ_r

$$Df_r(x) = \lambda_r f_r(x), \quad \int d^4x \bar{f}_{r'}(x) f_r(x) = \delta_{rr'}. \tag{3.8}$$

The functions f_r are also eigenmodes of the *massive* operator $D+m$ with eigenvalues $\lambda_r + m$

$$\left[D+m\right] f_r(x) = \left[\lambda_r + m\right] f_r(x). \tag{3.9}$$

Using the following rules for Grassmann variables

$$a_r^2 = 0, \quad \int da_r 1 = 0, \quad \int da_r a = 1, \tag{3.10}$$

it can be checked that the denominator of (3.5) gives $\det\left[D+m\right]$

$$\begin{aligned}
\int D\psi(y)D\bar{\psi}(y)e^{-\int d^4y\bar{\psi}(y)(D+m)\psi(y)} &= \int \prod_r d\bar{a}_r da_r e^{-\sum_r \bar{a}_r a_r(\lambda_r+m)} \\
&= \prod_r \int d\bar{a}_r da_r \left(1 - \bar{a}_r a_r(\lambda_r+m)\right) \\
&= \prod_r (\lambda_r + m) \\
&= \det\left[D+m\right].
\end{aligned} \tag{3.11}$$

Similarly, the numerator gives

$$\begin{aligned}\int D\psi(y)D\bar{\psi}(y)\left(\bar{\psi}(x)\gamma^5\psi(x)\right)e^{-S} \\ &= \sum_{s,s'}\int\prod_r d\bar{a}_r da_r\left(1-\bar{a}_r a_r(\lambda_r+m)\right)\bar{a}_s a_{s'}\bar{f}_s\gamma^5 f_{s'} \\ &= \sum_s \bar{f}_s\gamma^5 f_s\prod_{r\neq s}(\lambda_r+m).\end{aligned} \tag{3.12}$$

Dividing (3.12) by (3.11), the right hand side of (3.4) becomes

$$\int d^4x\langle\bar{\psi}(x)\gamma^5\psi(x)\rangle = \sum_s \frac{\int d^4x\bar{f}_s(x)\gamma^5 f_s(x)}{\lambda_s+m}. \tag{3.13}$$

Now, since $Df_r = \lambda_r f_r$ and $\{D,\gamma^5\}=0$, $\gamma^5 f_r$ is also an eigenfunction of D with eigenvalue $-\lambda_r$

$$\{D,\gamma^5\}f_r = 0 = D\gamma^5 f_r + \gamma^5 D f_r \quad \Rightarrow \quad D\left(\gamma^5 f_r\right) = -\lambda_r\left(\gamma^5 f_r\right). \tag{3.14}$$

Hence the orthonormal condition $\int d^4x\bar{f}_r f_{r'} = \delta_{rr'}$ implies

$$\int d^4x\bar{f}_s(x)\gamma^5 f_s(x) = 0 \ \text{ for } \ \lambda_s \neq 0, \tag{3.15}$$

and only those terms with $\lambda_s = 0$ (i.e., zero modes) survive in the sum in (3.13), so

$$m\int d^4x\langle\bar{\psi}(x)\gamma^5\psi(x)\rangle = \sum_{\text{zero modes}}\int d^4x\bar{f}_s(x)\gamma^5 f_s(x). \tag{3.16}$$

Finally, because zero modes have definite chirality, i.e., $\gamma^5 f_s = \pm f_s$ for $\lambda_s = 0$, we have

$$m\int d^4x\langle\bar{\psi}(x)\gamma^5\psi(x)\rangle = n_R - n_L, \tag{3.17}$$

where n_R, n_L are the numbers of zero modes with $+1$, -1 chirality. Substituting this back into (3.4), we obtain the index theorem.

3.2 Random Matrix Theory

Applications of Random Matrix Theory (RMT) to QCD will be reviewed in this section. We have seen that the index theorem relates the number of zero modes of the Dirac operator to the topological charge of the background gauge fields. Random Matrix Theory, on the other hand, gives analytic expressions for the distribution of low-lying *nonchiral* modes in different topological sectors.

RMT was originally invented to study the distribution of energy levels of complex nuclei [77]. Random matrix models that have the general symmetries of nuclear interactions (e.g., time reversal symmetry) were able to describe experimental data with high accuracy. Nowadays RMT finds applications in many branches of physics [78]. In this section the QCD Dirac spectrum will be studied within the context of chiral Random Matrix Theory. As we will see below the matrix theory reflects the chiral structure of QCD.

Consider the matrix model with partition function

$$Z = \int DW \left(\det \tilde{D}\right)^{n_f} e^{-N\Sigma \mathrm{Tr}(W^\dagger W)}, \tag{3.18}$$

where

$$\tilde{D} = \begin{pmatrix} 0 & iW \\ iW^\dagger & 0 \end{pmatrix} \tag{3.19}$$

which plays the role of the Dirac operator. Here W is a $n \times m$ matrix with $|n-m| = Q$ and $n+m = N$. The constant Σ is the chiral condensate [2] which will act as a fitting parameter in our analysis (see (3.23)) . This model reproduces the following chiral properties of QCD:

- **Spontaneous symmetry breaking of chiral symmetry**. The partition function (3.18) describes n_f equivalent massless quark flavours. The $\mathrm{SU}(n_f)$ flavour symmetry is spontaneously broken with chiral condensate Σ. This is analogous to the breaking of the chiral $[\mathrm{SU}(3)]_A$ symmetry in QCD.

- **The $[\mathrm{U}(1)]_A$ symmetry**. The non-zero eigenvalues of the random matrix Dirac operator $\tilde{D}$ come in pairs $\pm\lambda$. This represents the $[\mathrm{U}(1)]_A$ symmetry of QCD

[2] To see that Σ is the chiral condensate, introduce a quark mass m_f such that $\tilde{D} \to \tilde{D} + m_f$. The chiral condensate is defined by $\lim_{m_f \to 0} \lim_{N\to\infty} -\frac{1}{N}\frac{d}{dm_f} \ln Z$ which is equal to Σ.

which is realized through the continuum commutation relation $\{\gamma^5, D\} = 0$ so that the eigenvalues the Dirac operator D also come in pairs.

- **Topology**. The model satisfies the index theorem. The Dirac matrix $\tilde{D}$ has exactly $Q = |n - m|$ zero eigenvalues.

The conjecture of RMT is that spectral fluctuations are universal, and theories that have the same global symmetries should share similar spectral properties. Therefore one might expect the QCD Dirac spectrum to be naturally described by the eigenvalue distribution function $\rho(\lambda)$ (the spectral density) of the matrix model (3.18)

$$\rho(\lambda) = \lim_{N\to\infty} \langle \frac{1}{N} \sum_{k=1}^{N} \delta(\lambda - \lambda_k) \rangle. \tag{3.20}$$

In Ref. [26], $\rho(\lambda)$ was calculated analytically so that these ideas can be checked in numerical simulations. We will only describe some of the key elements of the derivation here. The most important observation is that any complex matrix W can be decomposed as $W = U\Lambda V^{-1}$, where U, V are unitary and Λ is a positive definite diagonal matrix with entries $\lambda_1, \ldots, \lambda_N$. With this transformation, the eigenvalue distribution can be written as

$$\rho_N(\lambda_1, \ldots, \lambda_N) = J(\lambda_1, \ldots, \lambda_N) \prod_f \prod_k \lambda_k^2 \exp\left[-N\Sigma \sum_{k=1}^{N} \lambda_k^2 \right], \tag{3.21}$$

where $J(\lambda_1, \ldots, \lambda_N)$ is the Jacobian characterizing the change of integration variables from matrix W (the Haar measure) to λ_k. The spectral density $\rho(\lambda)$ can be obtained by integrating over all λ_k except one

$$\rho(\lambda) = \lim_{N\to\infty} \frac{1}{N} \int \left(\prod_{k=2}^{N} d\lambda_k \right) \rho_N(\lambda_1, \ldots, \lambda_N). \tag{3.22}$$

The multiple integral can be evaluated analytically and the result is [25]

$$\rho^Q(\zeta) = \frac{\Sigma}{2} \zeta \left[J_Q^2(\zeta) - J_{Q-1}(\zeta) J_{Q+1}(\zeta) \right], \tag{3.23}$$

where $J_n(\zeta)$ is the nth-order Bessel function, $\zeta \equiv \lambda\Sigma V$ and V is the volume. Note that the chiral condensate Σ acts only as an overall scaling factor. Another useful

statistic is the distribution $\rho_{\rm min}$ of the smallest non-zero eigenvalue

$$\begin{aligned}
\rho_{\rm min}^{Q=0}(\zeta) &= \frac{\Sigma}{2} e^{-\zeta^2/4}, \\
\rho_{\rm min}^{Q=1}(\zeta) &= \frac{\Sigma}{2} I_2(\zeta) e^{-\zeta^2/4}, \\
\rho_{\rm min}^{Q=2}(\zeta) &= \frac{\Sigma}{2} \left[I_2^2(\zeta) - I_1(\zeta) I_3(\zeta) \right] e^{-\zeta^2/4},
\end{aligned} \tag{3.24}$$

where $I_n(\zeta)$ is the nth-order modified Bessel function of the first kind. We are also interested in the cumulative distribution of the smallest eigenvalue, $\mathcal{P}_{\rm min}^{Q}(\zeta)$, which is obtained by simply integrating the above equations

$$\mathcal{P}_{\rm min}^{Q}(\zeta) = \frac{\int_0^\zeta \rho_{\rm min}^{Q}(x) dx}{\int_0^\infty \rho_{\rm min}^{Q}(x) dx}. \tag{3.25}$$

Of course, QCD is much richer than the matrix model (3.18). Hence one question that should be asked is when QCD spectral correlations deviate from that of RMT. We will see later in Section 3.4 that agreement with RMT disappears if the physical volume of the lattice is smaller than $(1.2\text{fm})^4$.

3.3 Spectral Properties of Various Lattice Fermions

Now we have studied the response of Dirac eigenmodes to gauge field topology, it is important to check how these spectral properties are realized by the various discretization schemes. A summary of what we might expect to see is given in this section. Problems with staggered fermions will again be highlighted. We will also argue that these problems are caused by flavour-changing effects and therefore should become less severe if improved operators are used.

The staggered quark scheme lacks exact zero modes on the lattice. The continuum 4-fold degeneracy in the spectrum is lifted by flavour-changing effects so zero modes (if there are any) are split into complex conjugate pairs, $\lambda = 0 \rightarrow \lambda \approx \pm i\mathcal{O}(a^2)$, at non-zero lattice spacing. This was demonstrated in Fig. 1.3 in Chapter 1 where the lowest 10 eigenvalues of the *unimproved* staggered operator are plotted for 50 gauge field configurations. No zero modes, not even approximate, are visible. Because of the absence of zero eigenvalues, it is a long held belief that staggered fermions do not feel gauge field topology: $n_\pm$ are always equal to zero so Q is equal to zero also.

We can further explore this problem by studying the distribution of the low-lying *nonchiral* modes. An example was given in Fig. 1.4 where the distribution of the smallest eigenvalues $\rho^{Q}_{\rm min}$, again for the *unimproved* staggered operator, is compared with analytic results (3.24). The graph is taken from Ref. [25]. Overall about 17,000 gauge field configurations were analyzed. It is worrisome that all results agree perfectly with $\rho^{Q=0}_{\rm min}$, even after the configurations have been divided into different topological sectors according to their topological charges determined using the continuum formula (1.13). Similar conclusions were also reached in other studies [23, 24, 26].

In contrast the overlap Dirac operator has exact zero eigenvalues at finite lattice spacing. In Ref. [79], Zhang *et al.* showed that the topological charges calculated by counting the number of zero modes agree with the results computed using (1.13), if one is sufficiently close to the continuum limit. Furthermore, the distribution of nonchiral modes was found to be consistent with RMT in all charge sectors [29, 80]. This was shown in Fig. 1.5.

Since the absence of zero modes for the staggered Dirac operator is related to the breaking of the continuum flavour symmetry by flavour-changing interactions, one might expect the problems described above to go away, or at least become less significant, if improved operators are used. The motive of this work is to establish this claim by studying the spectral properties of a variety of improved operators. Four different systematic effects have been considered:

- improvement in the staggered operator,
- improvement in the gauge field action,
- lattice spacing,
- lattice volume.

We observe that eigenmodes with small eigenvalue and large chirality appear as the level of improvement in the operator increases. These small eigenmodes can be identified as the continuum zero modes associated with topology of the background gauge fields. The separation between these "zero modes" and the nonchiral modes increases when the gauge field action is also improved, or when one moves closer to the continuum limit by reducing the lattice spacing. All these suggest that discretization errors and lattice artifacts are indeed responsible for the failure of the *unimproved* operator to feel gauge field topology. After successfully identifying the "zero modes",

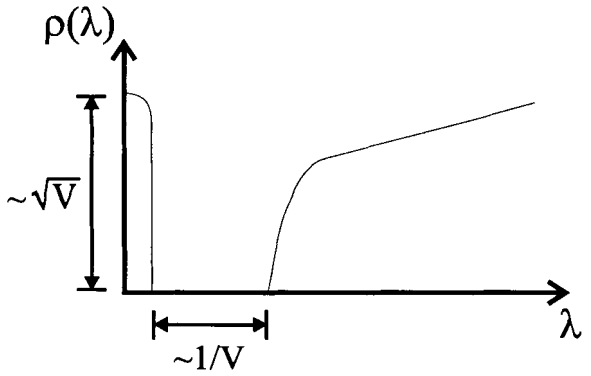

Figure 3.1: Spectral density and lattice volume. The gap between the zero modes and nonchiral modes scales as $1/V$ while the number of zero modes increases as $\sqrt{V}$.

the distribution of the remaining nonchiral is compared with the predictions of RMT. Excellent agreement is obtained not only for $Q = 0$ but also for nontrivial topological charge sectors.

The spectral density is also found to depend sensitively on the volume (V) of the lattice. In general, the charge average $\langle |Q| \rangle$ and consequently the number of zero modes scales like $\sqrt{V}$. This can be seen from the fact that the topological susceptibility, $\chi \equiv \langle Q^2 \rangle / V$, is independent of V. On the other hand, spectral analysis [81, 82] shows that the magnitude of the smallest nonchiral modes vanishes as $1/V$ as $V \to \infty$, see Fig. 3.1. These scaling properties are reflected in our data. In particular, we find that it again becomes difficult to identify the would be "zero modes" when V becomes too large. The magnitude of the smallest nonchiral modes decreases faster than the increase in the number of zero modes and hence the tails of the two distributions, zero modes and nonchiral modes, mix as V increases. Nonetheless zero modes can still be identified without much difficulty even for lattice volume as large as 16^4.

3.4 Simulations

Gauge field configurations are generated with both the Wilson plaquette action (2.5) and the tadpole improved gluon action (2.39) for a range of lattice spacings and volumes. The lattice spacing is determined from the linearly confining static quark potential, $V = \sigma R$. We measure the slope in lattice units (dimensionless), $\hat{\sigma} = a^2\sigma$. To extract a, the physical string tension $\sqrt{\sigma} \approx 0.44$GeV [83] is used. A sample calculation is given in Fig. 3.2. Simulation parameters are summarized in Table 3.1.

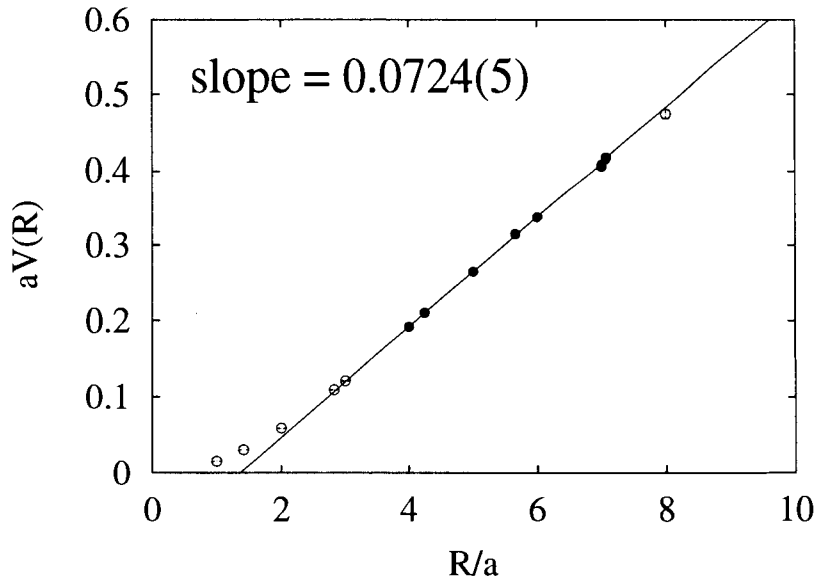

Figure 3.2: The inter-quark potential at $\beta = 8.26$ with improved gauge fields. The lattice spacing a can be determined from the slope $\hat{\sigma} = 0.0724(5)$ and the physical string tension $\sqrt{\sigma} \approx 0.44\text{GeV}$. Restoring $\hbar$ and c, we have $a^2 = \hat{\sigma}\hbar^2c^2/(0.44\text{GeV})^2$ so $a \approx 0.121\text{fm}$. Only those data points (•) at moderate separation are used in the fitting.

The couplings are carefully chosen such that lattice spacings agree between simulations using the Wilson action and the improved gauge action. Configurations are generated using the standard heat bath method [84, 85] and exactly 1000 configurations are generated in each case.

The eigenvalues and eigenvectors are computed using an accelerated conjugate gradient method with exact middle diagonalization [86]. Since the staggered operator is anti-Hermitian and satisfies $\{\epsilon(x), D^{sf}\} = 0$, the eigenvalues are purely imaginary and come in pairs $\pm i\lambda$. In addition, from (2.19), one can see that $(D^{sf})^2$ connects only even-even ($(D^{sf}_{ee})^2$) or odd-odd ($(D^{sf}_{oo})^2$) sites on the lattice. In this project, we choose to compute the eigenvalues of $(D^{sf}_{ee})^2$ since it is Hermitian and has real eigenvalues λ^2. Note that the extra doubling of modes induced by squaring is canceled by working on even sites only. To be precise, we compute the lowest 40 eigenvalues of $(D^{sf}_{ee})^2$, which correspond to the lowest 40 positive (imaginary) eigenvalues of D^{sf}.

For comparison we have also computed the small eigenvalues of the overlap Dirac operator D^{ov} on the smallest lattice with $V = 10^4$. Again, we use the operator $D^{ov\dagger}D^{ov}$ which is Hermitian and positive definite. Also $D^{ov\dagger}D^{ov}$ commutes with γ^5 so that

β	Action	$\hat{\sigma} = a^2\sigma$	$a\ (fm)$	Volume V
5.85	Wilson	0.0748(7)	0.123	10^4
6.0	Wilson	0.0478(5)	0.0981	12^4
6.2	Wilson	0.0259(5)	0.0722	16^4
8.26	improved	0.0724(5)	0.121	8^4, 10^4, 12^4, 16^4
8.62	improved	0.0456(4)	0.0958	12^4
9.18	improved	0.0246(5)	0.0704	16^4

Table 3.1: Simulation parameters and measured string tensions $\hat{\sigma} = a^2\sigma$. The couplings are carefully chosen such that lattice spacings agree between simulations using the Wilson action and the improved gluon action.

they can be simultaneously diagonalized [46, 79]. The eigenvalue solver is provided by Zhang [79], which uses the same conjugate gradient method mentioned above. The hopping parameter is set at $\kappa = 0.21$, which has been shown to be appropriate for our study of topology [79]. The matrix sign function $\epsilon(H^w)$ is approximated by a 14th-order Zolotarev expansion with maximum errors of $\mathcal{O}(10^{-10})$ in the interval [0.04,1.5]. Because of high computational cost we have only computed the lowest 5 eigenvalues in each chiral sector. Just a note, we find that computing all 40 eigenvalues of the staggered operator for a 10^4 configuration takes about 2 minutes, while it requires almost 2 days to complete the calculation, on the same configuration, for the overlap Dirac operator.

The chirality of an eigenmode $|\lambda\rangle$ is defined by $\chi \equiv \langle\lambda|\gamma^5|\lambda\rangle$. The eigenvector $|\lambda\rangle$ is a spin-singlet (only has space-time and colour indices) in the staggered quark scheme because of the spin-diagonalization procedure described in Section 3.3. Hence the usual definition of γ^5, which is a 4×4 operator acting on spinor space, becomes a 4-link operator Γ^5 in the staggered quark basis [81]

$$\langle\lambda|\Gamma^5|\lambda\rangle = \frac{1}{2^4}\sum_x \sum_{ijkl=\pm1} (-1)^{x_1+x_3}\lambda^\dagger(x)\bar{U}\lambda(x + i\hat{1} + j\hat{2} + k\hat{3} + l\hat{4}), \tag{3.26}$$

where $\bar{U}$ is the average of link products over all the equivalent shortest paths joining the two sites. There is no such complication for overlap fermions because spinor structure is retained in the formulation. The operator γ^5 is the standard chirality matrix, see (1.4).

3.5 Results

Results of our systematic study on the staggered Dirac operator's spectral properties is presented in this section. We have examined the dependence of the eigenvalue spectrum on

- improvement in the staggered operator,
- improvement in the gauge field action,
- lattice spacing,
- lattice volume.

It is observed that the distribution of the low-lying eigenmodes depends strongly on these systematic effects.

Improvement in the Staggered Operator

We first examine the effects of staggered operator improvement on the infrared eigenvalue spectrum. Four different operators have been considered: the unimproved operator, Asqtad, and the further improved UFat7×Asq and HYP operators. Comparisons are done with unimproved gauge fields for $\beta = 5.85$ ($a \approx 0.123$fm) and $V = 10^4$. The same comparisons with improved gauge fields (same lattice spacing and volume) will be presented in the next section. Results are shown in Fig. 3.3 where the absolute value of the chirality $|\chi|$ is plotted against the eigenvalue λ for the different operators. The symbols "○" label the would-be zero modes and "×" are the nonchiral modes. The same scale is used for the chirality. It can be observed that the eigenvalue spectrum depends quite sensitively on the way in which the staggered Dirac operator is improved. Eigenmodes with small eigenvalues and relatively large chirality appear as the level of improvement increases. These small eigenmodes can be identified as the zero modes associated with the topology of the background gauge fields. Throughout this project the following criteria are used for an eigenstate to be identified as a zero mode: (i) it is at least a factor of 2 smaller in eigenvalue than the smallest nonchiral mode and (ii) the chirality is at least 5 times larger than that of the smallest nonchiral mode.

One can see also that, as the level of improvement increases, the continuum 4-fold degeneracy emerges where the scattered eigenmodes begin to form quartets. Note

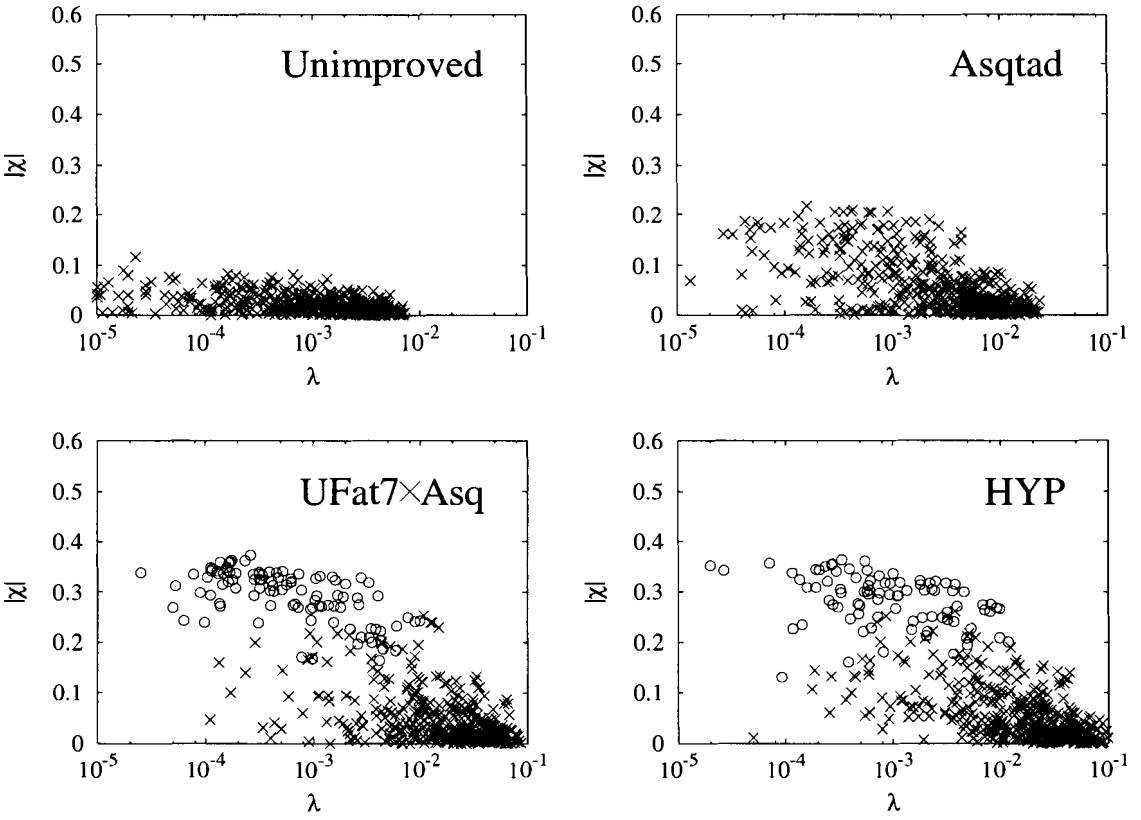

Figure 3.3: Spectral graphs for the different staggered operators with unimproved gauge fields [$\beta = 5.85$ ($a \approx 0.123$fm) and $V = 10^4$]. Results are shown for 50 configurations. The symbols "o" label the would-be zero modes and "×" are the nonchiral modes.

that at this lattice spacing with unimproved gauge fields the Asqtad operator is not sensitive to the topology and lattice artifacts are still dominant. One only starts to see a separation between the zero modes and the nonchiral modes with further improved operators. In addition, a large renormalization is observed for the chirality of the would-be zero modes, which is $|\chi| \approx 0.5$ instead of unity. This large renormalization was also observed in previous studies [81, 30]. Nevertheless, the zero modes can be identified without any difficulty in most of the cases for the UFat7×Asq and HYP operators.

To quantify the separation between the "zero modes" and the nonchiral modes, the ratios of eigenvalues between the smallest nonchiral mode and the largest "zero mode" are plotted in Fig. 3.4 for a small set of configurations with nontrivial topology (i.e., "zero modes" exist). We should mention that the configurations in Fig. 3.4 are

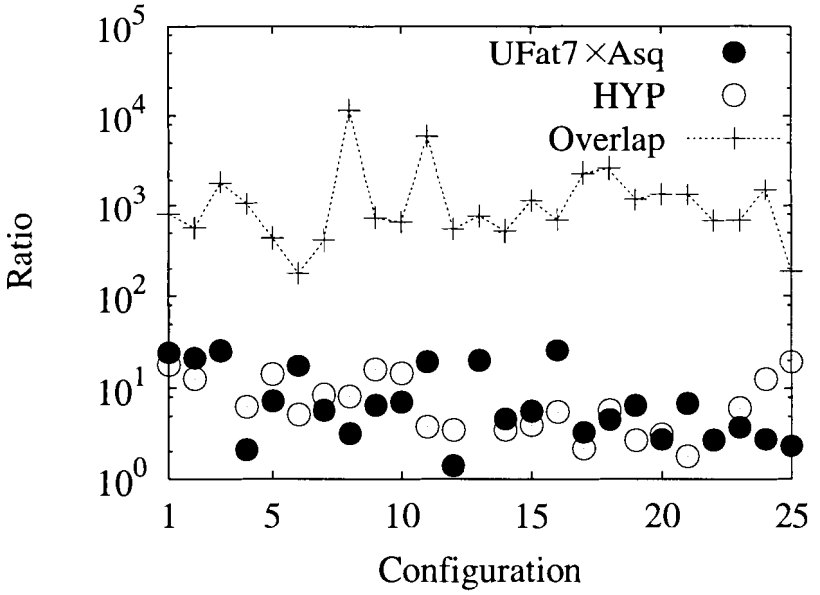

Figure 3.4: Ratios of eigenvalues between the smallest nonchiral mode and the largest "zero mode" for unimproved gauge fields [$\beta = 5.85$ ($a \approx 0.123$fm) and $V = 10^4$].

different for different operators as the topological indices obtained by using different operators generally do not agree on a configuration by configuration basis (see next paragraph). It is possible that for a given configuration there are no chiral modes for one operator while they exist for the others. For comparison, results of the overlap operator are also shown. Theoretically, the ratio is infinite for the overlap operator because exact zero modes exist on the lattice for overlap fermions. It is finite here solely because of computational precision. Results here show that the staggered operators are less sensitive to the topology at this lattice spacing with unimproved background gauge fields. The ratios are always three orders of magnitude for the overlap operator but only about one order of magnitude for the staggered Dirac operators. Nevertheless the separation is large enough for the chiral modes to be identified. In addition our results also show that improvements using UFat7 links or hyper-cubic blocking are equally efficient.

The identification of the topological charge index for a given gauge field configuration is not unique. Because of lattice artifacts and the different ways the staggered operator is improved, it can be expected that the topological charge indices obtained by using different operators do not always agree on a configuration by configuration basis. It is only when one is close to the continuum limit that the results agree. Even with the overlap operator previous studies [79] showed that the topological indices

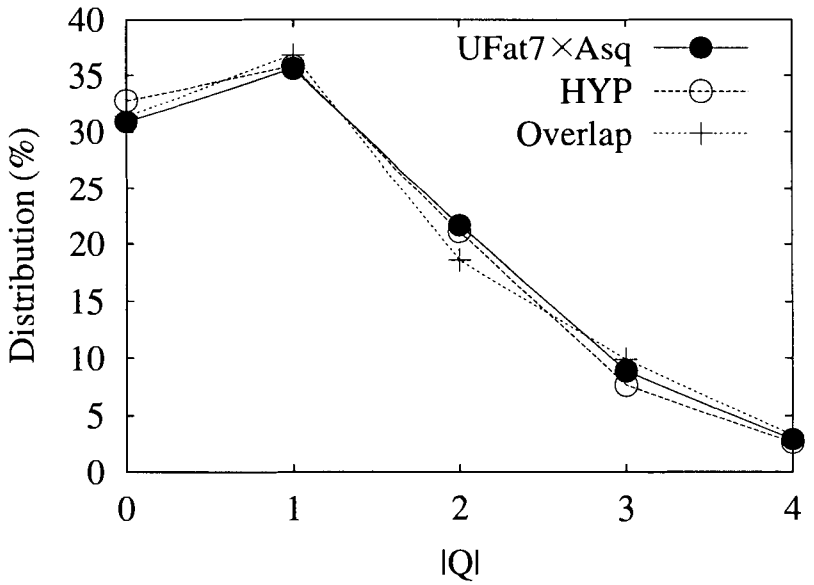

Figure 3.5: Topological charge distributions obtained by using different operators for unimproved gauge fields [$\beta = 5.85$ ($a \approx 0.123$fm) and $V = 10^4$].

do not agree on a configuration by configuration basis when, for example, a different mass parameter is used in the kernel. In the present case, we find that the topological charge indices determined by the different operators agree about 60%–70% of the time, compared to 28% if the values were completely random. More explicitly, indices from different operators are compared pairwise and the agreement is 63% for overlap and UFat7×Asq, 68% for overlap and HYP, 78% for UFat7×Asq and HYP. Note that the agreement between UFat7×Asq and HYP is larger than that obtained for an improved staggered operator and the overlap operator. It is then important to check whether the charge distributions are also different because physical observables, e.g., the topological susceptibility, are related to the ensemble average of the topological charge. The distributions obtained by these operators are given in Fig. 3.5. It can be observed that there is no significant difference among the results. This is important because it indicates that physics is independent of the discretization scheme and one would expect topological quantities obtained by these operators to agree.

Improvement in the Gauge Field Action

Lattice artifacts can be further suppressed if improvement is also applied to the gauge field action. This can be seen in Fig. 3.6 where the infrared eigenvalue spectra

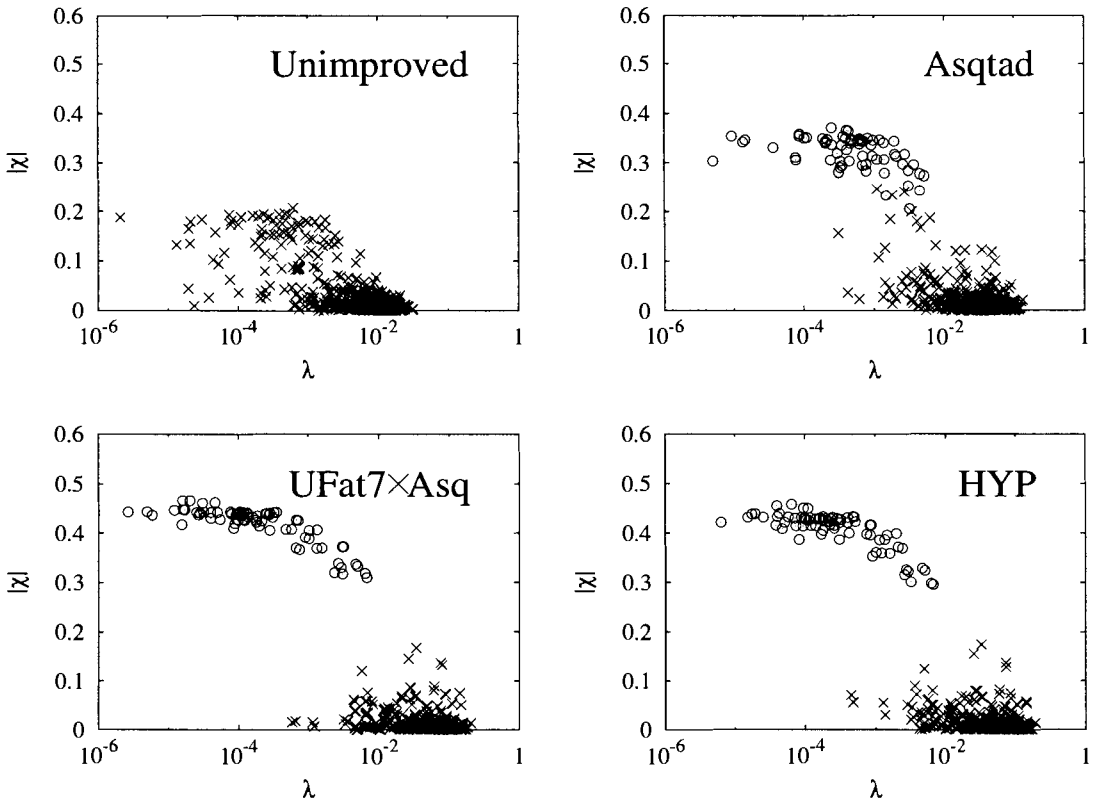

Figure 3.6: Same as Fig. 3.3 but with improved gauge fields [$\beta = 8.26$ ($a \approx 0.121$fm), $V = 10^4$].

of the different staggered operators are shown for configurations generated using the tadpole improved gauge field action (2.39). Here $\beta = 8.26$ ($a \approx 0.121$fm) and lattice volume is $V = 10^4$ so that both the lattice spacing and physical volume are very similar to those used in the unimproved case. Results here show that better topological properties are realized when the gauge field action is also improved. In particular even the Asqtad operator is sensitive to the topology at this coarse lattice spacing and zero modes can be identified unambiguously for the UFat7×Asq and HYP operators.

To have a quantitative picture of how improvement in the gauge field action affects the spectral flow, we again plot the ratios of eigenvalues between the smallest nonchiral mode and the largest zero mode in Fig. 3.7 for configurations with nontrivial topology. The same scale is used in Figs. 3.4 and 3.7. In comparison to Fig. 3.4, it can be observed that, for UFat7×Asq and HYP, the ratios increase from one order of magnitude in the unimproved case to three orders of magnitude when improved gauge fields are used. Hence, gauge field improvement clearly increases the separation

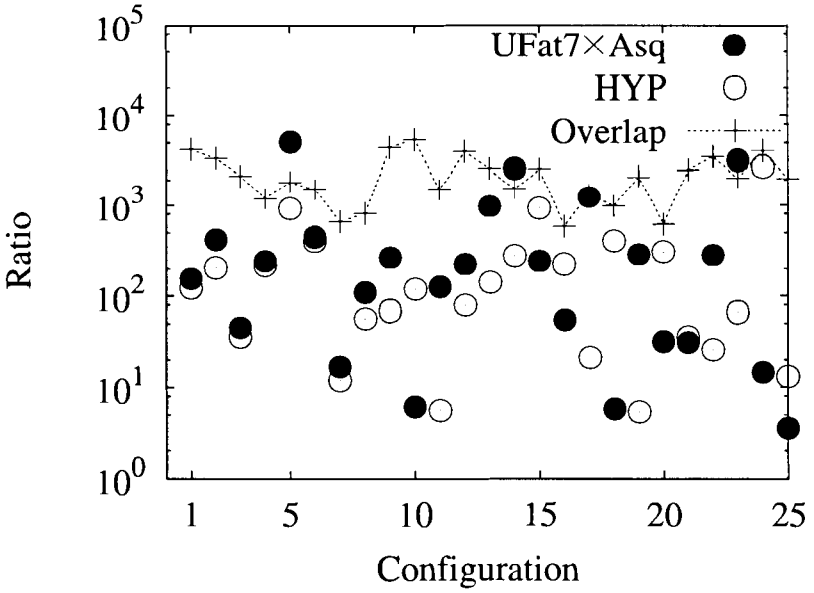

Figure 3.7: Same as Fig. 3.4 but with improved gauge fields [$\beta = 8.26$ ($a \approx 0.121$fm), $V = 10^4$].

between the chiral zero modes and the nonchiral modes. We should again emphasize here that the ratios should be infinite theoretically for the overlap operator since exact zero modes exist on the lattice.

We have also compared the topological indices obtained by the different operators in this case. It is found that the agreement increases significantly when the gauge field action is also improved: 91% between overlap and UFat7×Asq, 90% between overlap and HYP, and 96% between UFat7×Asq and HYP which is again the highest. The charge distributions are given in Fig. 3.8. It can be observed upon comparing with Fig. 3.5 that better agreement is obtained with improved gauge fields. Results here are significant because they indicate that different operators do respond the same way to the topology of the background gauge fields when discretization errors and lattice artifacts are reduced. In particular, results here show that the charge indices obtained by using the staggered operators and the overlap operator, two completely different representations of the Dirac operator on the lattice, agree even on a configuration by configuration basis at a high percentage as the level of improvement increases.

Dependence on Lattice Spacing

Here we examine the dependence of the infrared eigenvalue spectrum on lattice spacing and study the spectral flow as one approaches the continuum limit. Calcu-

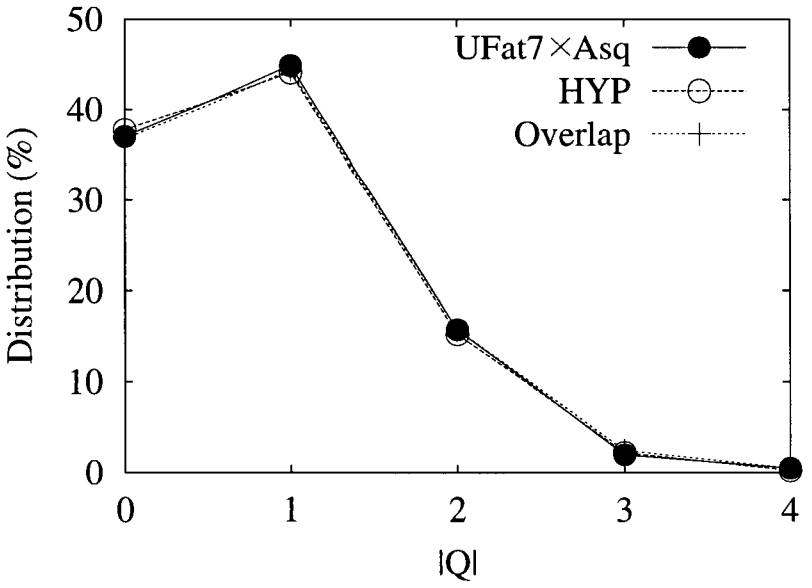

Figure 3.8: Same as Fig. 3.5 but with improved gauge fields [$\beta = 8.26$ ($a \approx 0.121$fm), $V = 10^4$].

lations are done at three lattice spacings with fixed physical volume $V \approx (1.2\text{fm})^4$ (so lattice volume increases as lattice spacing decreases, see Table 3.1). Results are shown for the Asqtad and UFat7×Asq operators in Fig. 3.9. One sees that separation between the zero modes and nonchiral modes becomes more clear. In addition the continuum 4-fold degeneracy is better realized as one approaches the continuum limit. Note that the chirality of the zero modes increases as the lattice spacing decreases and it is larger for the UFat7×Asq operator. This gives evidence to the fact that discretization errors and lattice artifacts are indeed responsible for the failure of staggered fermions to be sensitive to gauge field topology on coarse lattices. The chiral zero modes associated with the topology of the background gauge fields emerge as one approaches the continuum limit.

Our results also show that it is necessary to use a lattice spacing $a \lesssim 0.1$fm for the Asqtad operator to be sensitive to gauge field topology. This is similar to the lattice spacings used nowadays in dynamical simulations of QCD using the Asqtad fermion action and the tadpole improved gauge field action. On the other hand, further improvement of the staggered quark action, e.g, actions with unitarized fat links UFat7×Asq, may be necessary when working on coarse lattices to ensure that continuum physics is reproduced correctly.

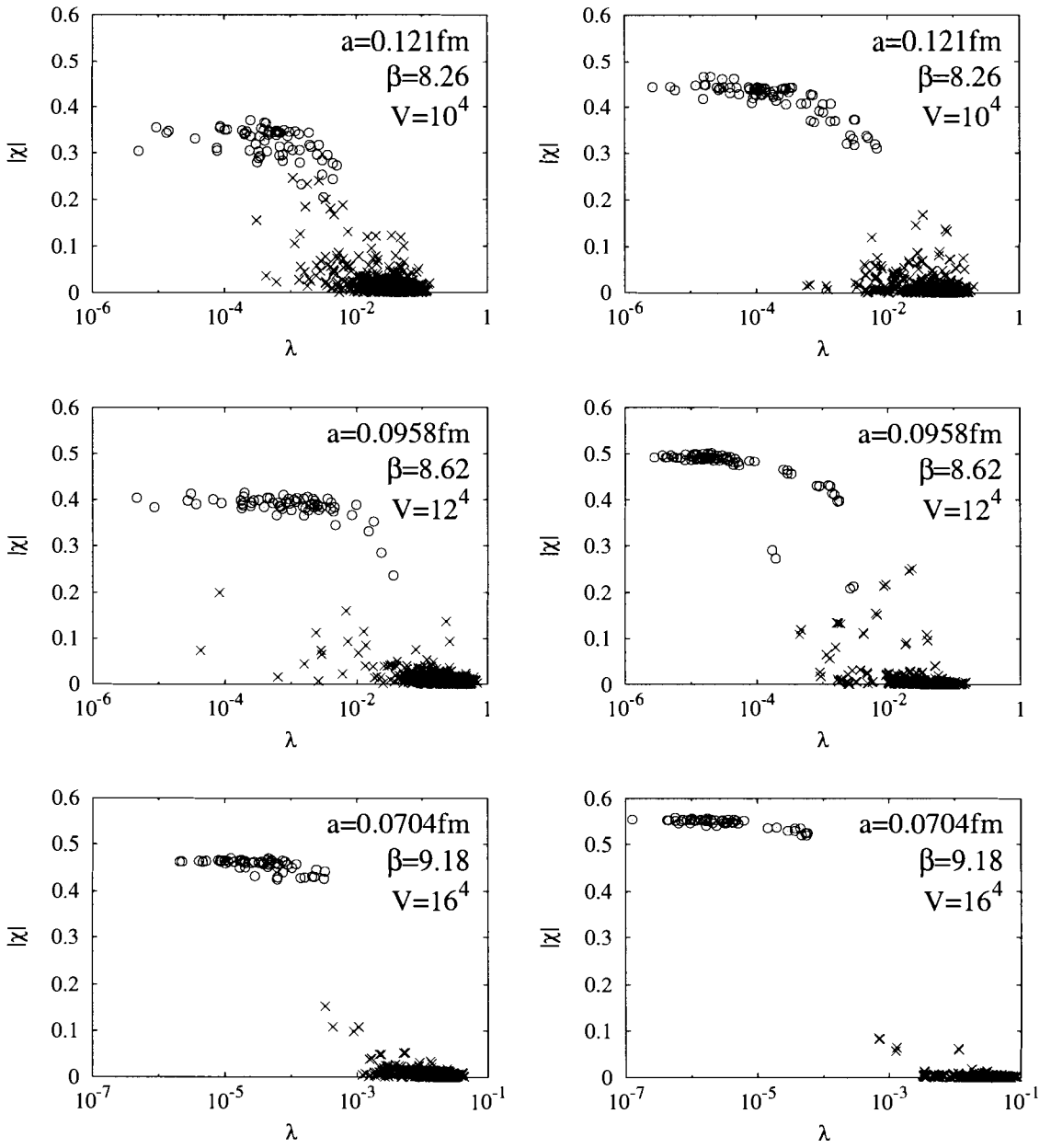

Figure 3.9: Dependence on lattice spacing. Results are shown for the Asqtad (left column) and the UFat7 × Asq (right column) operators with improved gauge fields. Physical volumes are $\approx (1.2\text{fm})^4$ in all cases.

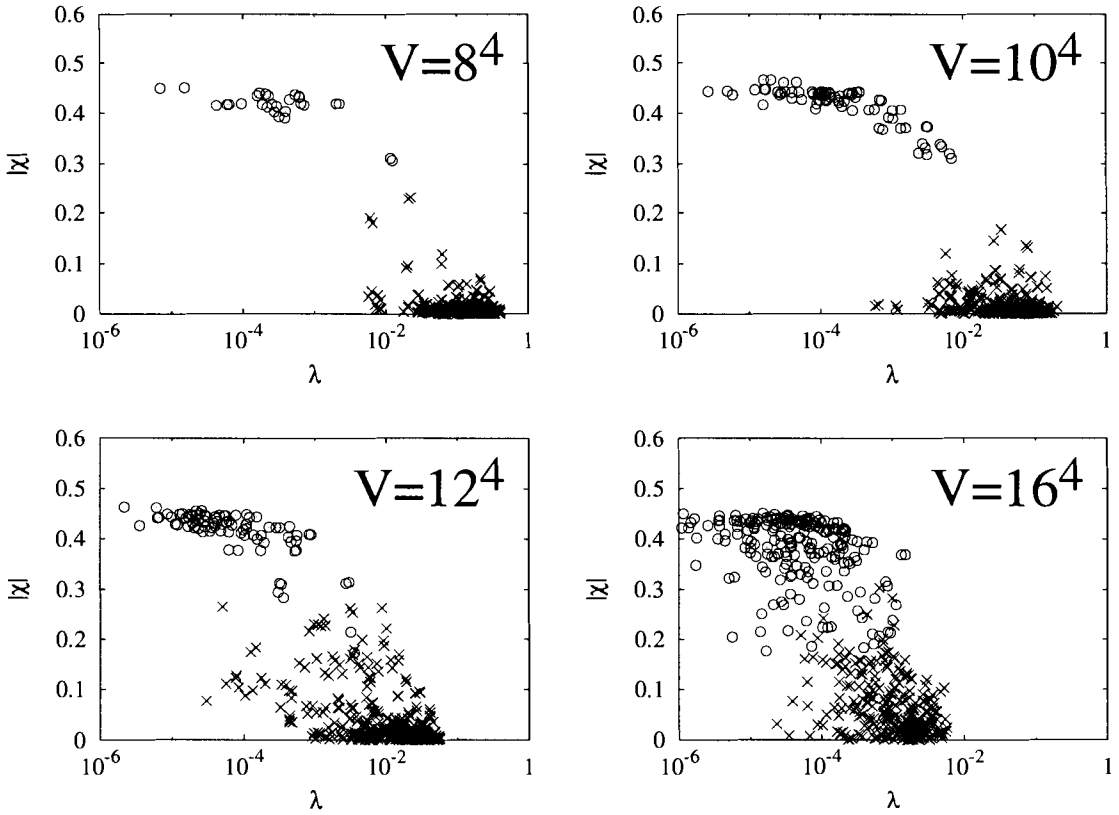

Figure 3.10: Spectral graphs for the UFat7×Asq operator at a fixed coupling $\beta = 8.26$ ($a \approx 0.121$fm) for volumes $V = 8^4$, 10^4, 12^4 and 16^4 with improved gauge fields. The spectrum becomes noisy again for large volumes.

Dependence on Lattice Volume

As discussed earlier, we expect a strong dependence of the spectral density on the volume V of the lattice and the topological charge average $\langle Q^2 \rangle$ should scale with V. In Fig. 3.10 the infrared eigenvalue spectrum of the UFat7×Asq operator is given for lattice volumes $V = 8^4$, 10^4, 12^4 and 16^4 at a fixed lattice spacing $a \approx 0.121$fm ($\beta = 8.26$) with improved gauge fields. Results from previous sections showed that zero modes should be visibly separated from the nonchiral modes at this spacing for configurations generated by the improved gauge action. This is the case when the volume is $< (1.2\text{fm})^4$. The spectrum, however, becomes noisy again for larger volumes. A similar volume effect has been seen with the overlap fermion operator also [29, 80].

Since the gap between the zero modes and the nonchiral modes scales as V^{-1} (see Fig. 3.1), there are more low-lying nonchiral modes as volume increases. As Fig. 3.10

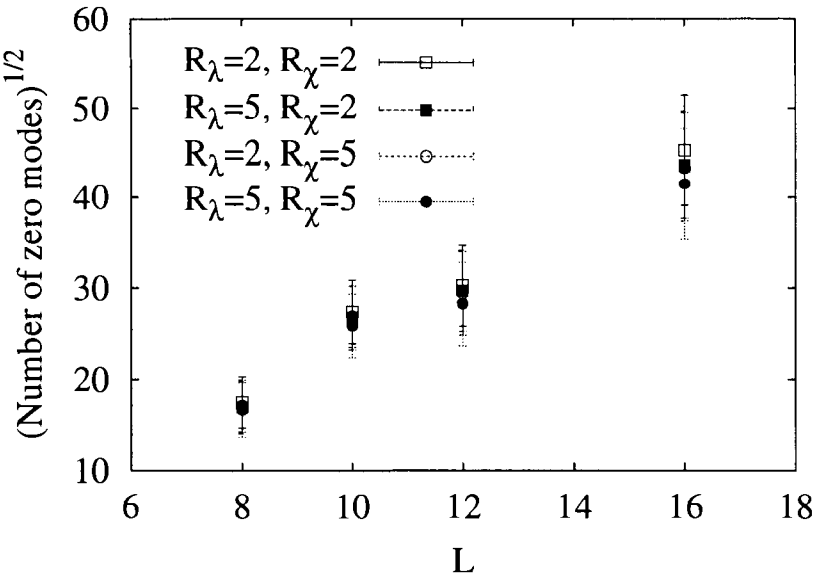

Figure 3.11: The square root of the total number of zero modes of the UFat7×Asq operator as a function of lattice size L (lattice volume $V = L^4$). The number of chiral zero modes increases roughly as $\sqrt{V}$. Results of using different criteria for identifying the zero modes are shown.

shows, a certain volume is necessary before the would-be zero modes show up and sensitivity to topology is established. As the volume is increased even further, the number of chiral zero modes increases roughly as $\sqrt{V}$ as can be inferred from Fig. 3.11. In the configuration average, the tail of the chiral-mode distribution begins to merge with the low eigenvalue tail of the nonchiral-mode distribution. However, the identification of the would-be zero modes is not quite as difficult as it may appear from Fig. 3.10. As seen from Fig. 3.11 the criteria which we adopt for a zero mode, namely, at least a factor of 2 smaller in eigenvalue than the smallest nonchiral mode ($R_\lambda = 2$) and a factor of 5 larger in chirality ($R_\chi = 5$), are very robust even for the 16^4 lattice. Imposing other values for these factors gives very similar results.

The expected increase of $\langle|Q|\rangle$ with the volume of the lattice can be seen in Fig. 3.12 where the topological charge distribution is shown for different lattice volumes. Most configurations have trivial topological structure when the volume is small and the charge average $\langle|Q|\rangle$ increases gradually with the volume of the lattice.

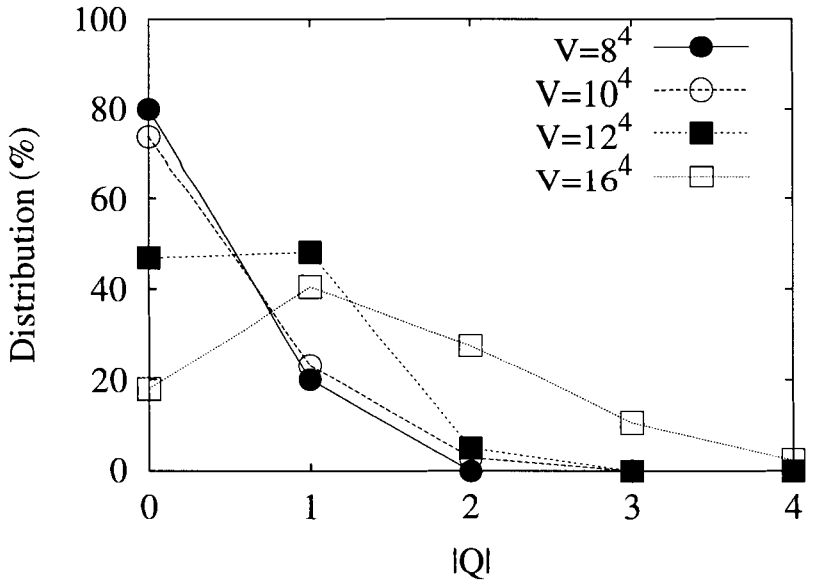

Figure 3.12: Topological charge distribution for different lattice volumes. Results are shown for the UFat7 × Asq operator at $\beta = 8.26$ ($a \approx 0.121$fm) with improved gauge fields.

Comparison with RMT

Results from our systematic analysis give strong indications that staggered fermions are sensitive to gauge field topology when lattice artifacts are sufficiently suppressed. It is then important to compare the distribution of the nonchiral modes, after successfully identifying the would-be zero modes, against the predictions of RMT. In particular, we study the cumulative distribution of the smallest nonchiral modes in different topological sectors $\mathcal{P}^{Q}_{\text{min}}(\zeta)$ (see (3.25)).

Calculations are done for three different operators (UFat7×Asq, HYP, and overlap) on two ensembles of configurations (unimproved and improved gauge fields with $a \approx 0.12$fm, $V = 10^4$). These ensembles are specifically chosen because the size of the lattice is limited by the cost in computing the eigenvalue spectra of the overlap operator while a coarse grid is used so that the physical volume is larger than the critical value $(1.2\text{fm})^4$. This criterion is important as it ensures that topological structure is fully formed [29, 80].

In our analysis, the would-be zero modes are first identified and the configurations are classified according to their charge indices obtained using the index theorem. We should reemphasize here that the indices obtained by using different operators do not always agree on a configuration by configuration basis but the charge distributions are

indistinguishable (see Figs. 3.5 and 3.8). It should also be noted that all configurations are used in our analysis. This is different from Ref. [25] where a small portion of the ensemble was discarded (see Fig. 1.3).

Results are shown in Fig. 3.13. The solid curves are predictions from RMT (3.25). Because computing the spectra for the overlap operator is much more expensive, the sizes of the ensembles are different: 1000 configurations for UFat7×Asq and HYP but only 400 for the overlap operator. This is the reason that the overlap results appear to have poorer agreement with the predictions of RMT. Note that the agreement is better with improved gauge fields. The results given here contribute to the evidence that staggered fermions do feel gauge field topology, provided that lattice artifacts are suppressed considerable, as the agreement with the predictions of RMT is impressive. They should be compared with previous studies [23, 24, 25, 26] with the unimproved staggered operator which appeared to indicate the presence of only a trivial topological sector.

3.6 Conclusion

In this project we studied numerically the spectral properties of a variety of improved staggered Dirac operators. Four systematics have been examined: i) improvement in the staggered operator, ii) improvement in the gauge field action, iii) lattice spacing, and iv) lattice volume.

It has been observed that the infrared eigenvalue spectrum depends sensitively on the way in which the staggered fermion operator is improved. On coarse lattices the unimproved operator is insensitive to gauge field topology. As the level of improvement increases, either on the operator itself or the background gauge fields, eigenmodes with small eigenvalues and large chirality appear. These small eigenmodes can be identified as the chiral zero modes associated with the topology of the gauge fields. Sensitivity to the topology also increases as one approaches the continuum limit. This gives evidence that lattice artifacts are responsible for the failure of the unimproved staggered operator to reflect properly the gauge field topology on coarse lattices. Our results also show that a lattice spacing $a \lesssim 0.1$fm is enough for the Asqtad operator to have a correct response to the topology with improved gauge fields. This spacing is of the order of the lattice spacings used in present-day state-of-the-act dynamical simulations of QCD. On the other hand, the next level of improved staggered opera-

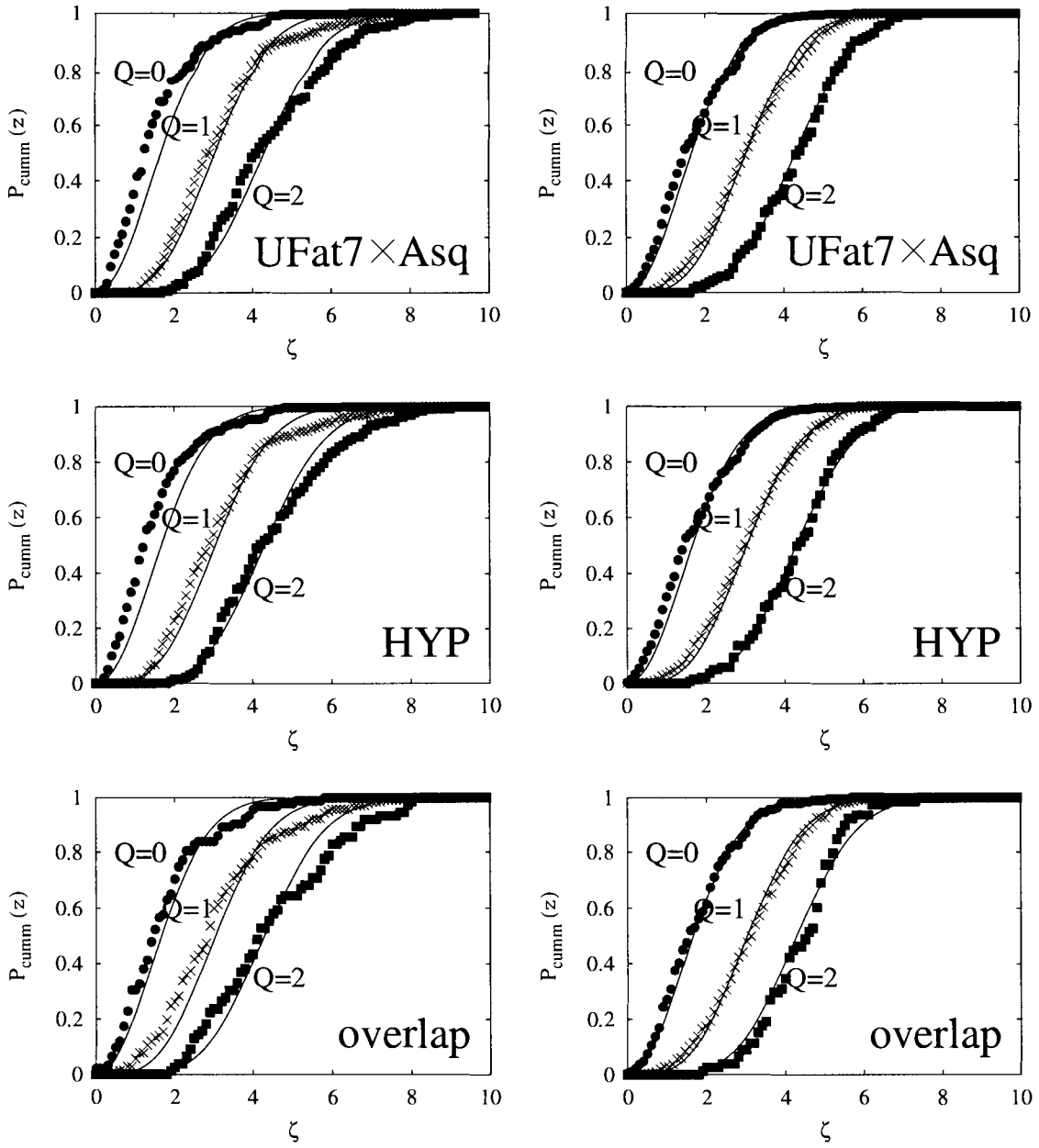

Figure 3.13: Cumulative distribution of the smallest nonchiral modes in different topological sectors. Results are shown for unimproved (left column) and improved (right column) gauge fields at $a \approx 0.12$fm, $V = 10^4$. Solid curves are predictions of RMT.

tors, e.g., UFat7×Asq, may be required to produce configurations which describe the correct continuum physics on coarser lattices. We also observe that the topological charge distribution is independent of which operator is used even though the charge indices do not always agree on a configuration by configuration basis. However, the agreement increases with the level of improvement. A minimum physical volume of about $(1.2\text{fm})^4$ seems to be necessary in order for zero modes to show up and for sensitivity to topology to be established. This effect was observed earlier for overlap fermions [29, 80]. As volume is increased the number of would-be zero modes increases as $\sqrt{V}$ but the number of low-lying nonchiral modes increases faster so some merging of tails of the distributions takes place. Up to the 16^4 volume considered here, it is still possible to make a clear separation of would-be chiral modes from nonchiral modes. The distribution of the nonchiral modes is matched with the predictions of RMT. The agreement is comparable to that obtained using overlap fermions.

In conclusion, this work gives strong evidence that, provided one uses improved staggered operators and improved gauge fields, staggered fermions properly feel gauge field topology.

Chapter 4

Lattice Perturbation Theory: An Example

The second topic of the thesis demonstrates how perturbative quantities can be efficiently computed from Monte Carlo simulations at weak coupling. In particular, perturbative series of Wilson loops, or the logarithm of the Wilson loops

$$-\frac{\ln W_{R,T}}{2(R+T)} = c_1\alpha_V(q^*_{R,T}) + c_2\alpha_V^2(q^*_{R,T}) + c_3\alpha_V^3(q^*_{R,T}) + \dots \tag{4.1}$$

are obtained through third order, in *full* QCD, with improved staggered fermions. Here R, T are the dimensions of the loop, and we will define the expansion parameter $\alpha_V(q^*_{R,T})$ later in this chapter. Two sets of actions have been considered

- **unimproved**: the Wilson plaquette action (2.5) and the unimproved staggered quark action,
- **MILC**: the 1-loop improved gauge field action (2.40) and the Asqtad action.

From now on we will simply refer to these actions as the *unimproved* action and the *MILC* action. The MILC [1] action is currently used in one of the most extensive studies of non-perturbative QCD on the lattice [10].

In this chapter, we will first demonstrate the important of lattice perturbation theory. Lattice field theory was originally invented to study the non-perturbative nature of QCD. Hence there seems to be a contradiction to consider perturbation

[1] It is called the MILC action because it is used in simulations done by the MILC collaboration. The action, however, was not proposed by the MILC collaboration.

theory on the lattice. Nevertheless, perturbative calculations are useful and sometimes essential in many aspects of lattice QCD. We have already seen that perturbative matching plays a crucial role in the attempt to restore short distance physics to the lattice actions. Perturbation theory is also important in connecting simulation results to physical quantities in the continuum. An example, the precise determination of the strong coupling constant, $\alpha_s^{\overline{MS}}(M_Z)$ [11, 12, 13], from lattice QCD will be presented in this chapter. This example will also review some of the basic ingredients of lattice perturbation theory. Results in this thesis are directly applicable to this research problem.

An Example: Precise Determination of $\alpha_s^{\overline{MS}}(M_Z)$ from Lattice QCD

Precise determination of the strong coupling constant is important not only to QCD phenomenology but also in the search of new physics. Any discrepancy between theoretical prediction and experimental data would signal the existence of new theory beyond the standard model. Figure 4.1 shows the values of $\alpha_s^{\overline{MS}}(M_Z)$ obtained by various experiments and theoretical calculations [2]. The coupling constant is evaluated at the scale M_Z (mass of the Z-boson) in the $\overline{MS}$ (minimal subtraction) renormalization scheme. We will explain this terminology below. It can be observed that lattice QCD provides one of the most accurate determinations of the coupling, $\alpha_s^{\overline{MS}}(M_Z) = 0.121(3)$, which agrees extremely well with the "world-average" of $\alpha_s^{\overline{MS}}(M_Z) = 0.119(2)$. The lattice result is obtained with staggered fermions [12]. A summary of other lattice determinations of $\alpha_s^{\overline{MS}}(M_Z)$ can be found in Ref. [2]. The latest lattice calculation [13], again uses staggered quarks, gives $\alpha_s^{\overline{MS}}(M_Z) = 0.1170(12)$ which has a even smaller error. This impressive agreement between lattice results and other determinations demonstrates that lattice QCD, which governs long-distance hadronic physics, is the same theory as the QCD of perturbation theory, which concentrates on high energy processes such as jet production.

Our presentation will essentially follow the works of Ref. [11, 12, 13]. Four steps are involved in the determination of $\alpha_s^{\overline{MS}}(M_Z)$ from lattice QCD:

- Perform full dynamical simulation of QCD using the MILC action (the unimproved action was used in the first two calculations [11, 12]).
- Determine the lattice spacing by measuring some long-distance physical quantities on the lattice such as a hadron mass, using experimental value as input.

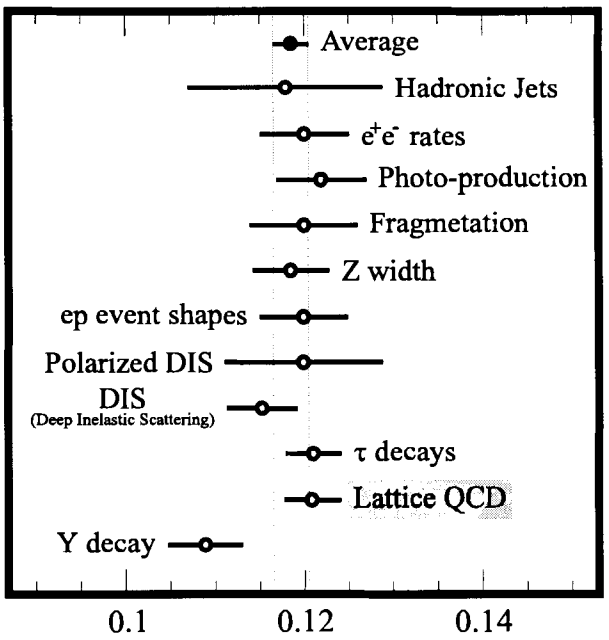

Figure 4.1: The strong coupling constant $\alpha_s^{\overline{MS}}(M_Z)$ determined from various experiments and theoretical calculations. Results are taken from the 2004 Review of Particle Physics [2]. The coupling constant is evaluated at the scale M_Z (mass of the Z-boson) in the $\overline{MS}$ (minimal subtraction) renormalization scheme.

- Choose a short distance quantity whose perturbative series is well known at least through second order. A good choice is the expansion of a small Wilson loop (4.1). To extract the coupling constant, equate the expansion to the non-perturbative result $-\ln \langle W_{R,T} \rangle_{MC}$ obtained in Monte Carlo simulation. More explicitly, we solve for $\alpha_V(q^*_{R,T})$ in

$$-\frac{\ln \langle W_{R,T} \rangle_{MC}}{2(R+T)} = c_1 \alpha_V(q^*_{R,T}) + c_2 \alpha_V^2(q^*_{R,T}) + c_3 \alpha_V^3(q^*_{R,T}) + \ldots \tag{4.2}$$

  where the momentum scale $q^*_{R,T} \propto a^{-1}$ and a is the lattice spacing determined above. So far the perturbative coefficients have only been computed analytically. **The purpose of this project is to give another determination of c_n using Monte Carlo methods.**

- Convert the result to $\overline{MS}$ scheme and integrate the running coupling formula to M_Z to obtain $\alpha_s^{\overline{MS}}(M_Z)$.

We are now going to discuss these steps in detail.

Determination of the Lattice Spacing

Lattice spacing is set implicitly by the value of β. It can be determined by computing a physical observable on the lattice and comparing the result to the experimental value. One should choose an observable which can be measured with high accuracy. The Υ mass splitting ($M_\Upsilon - M_{\Upsilon'}$) was used in Refs. [11, 12, 13]. These heavy-quark systems were chosen because they are essentially non-relativistic so that the quark propagators can be computed efficiently and precisely by using non-relativistic effective field theory such as lattice non-relativistic quantum chromodynamics (NRQCD). They are small in physical size hence finite volume effect is negligible even on modestly sized lattice. The mass splitting was also found to be insensitive to the input bare quark masses so that fine tuning of the mass parameters is not crucial. Finally, $M_\Upsilon - M_{\Upsilon'}$ is very well determined experimentally (=0.563GeV). On the lattice the mass splitting is measured in terms of the lattice spacing, i.e., $(M_\Upsilon - M_{\Upsilon'})a$. The lattice spacing can be deduced by equating this value to the experimental result.

We should mention that a major development of the recent calculation [13] is the use of other physical quantities involving light quarks (e.g. pion and kaon decay constants), to determine the lattice spacing. This is possible because accurate simulations can now be done, with 3 flavours of light quarks, using the MILC action. The lattice spacing determined from these quantities agrees with the spacing derived from Υ splitting.

Expansion Parameter

Choosing a proper expansion parameter is very important for perturbative calculations. For example [2], if $\alpha_{\rm good}$ produces a well behaved perturbative series for an observable, expansion with $\alpha_{\rm bad} \equiv \alpha_{\rm good}(1 - 1000\alpha_{\rm good})$ of the same quantity would have very large higher-order corrections

$$\begin{aligned} -\ln W_{R,T} &= c_1\alpha_{\rm good} + c_2\alpha_{\rm good}^2 + \mathcal{O}(\alpha_{\rm good}^3) \\ &= c_1\alpha_{\rm bad} + (1000c_1 + c_2)\alpha_{\rm bad}^2 + \mathcal{O}(\alpha_{\rm bad}^3). \end{aligned} \tag{4.3}$$

When working to all orders in $\alpha_{\rm bad}$ the second expansion is equally correct. However, it gives misleading results if the series is truncated since the higher-order terms are also significant.

[2] This argument is due to Lepage and Mackenzie [65].

A natural choice of expansion parameter for lattice theories is the bare coupling α_0, which is related to β by $\alpha_0 = \frac{6}{4\pi\beta}$. However, the nonlinear relationship between the link variable $U_{x,\mu}$ and the gauge field $A_\mu(x)$, $U_{x,\mu} \equiv e^{iaA_\mu(x)}$, leads to large renormalization of the coupling. As a result, expansions expressed in terms of α_0 generally converge much slower than those using other renormalization schemes. To illustrate this problem, consider the expansion of $-\ln W_{1,1}$ for the Wilson plaquette action. From perturbation theory [87], we have (to $\mathcal{O}(\alpha_0^2)$)

$$-\ln W_{1,1} = \frac{4\pi}{3}\alpha_0 [1 + 3.3729\alpha_0] = 0.4228 \tag{4.4}$$

for $\beta = 6.0$ or $\alpha_0 = \frac{6}{4\pi\beta} = 0.07958$ while Monte Carlo simulations in Chapter 3 give

$$-\ln\langle W_{R,T}\rangle_{MC} = 0.5215. \tag{4.5}$$

A renormalized coupling α_V will be defined in (4.8). At $\beta = 6.0$, it was found that $\alpha_V \approx 0.1414$ and expansion in α_V gives (to $\mathcal{O}(\alpha_V^2)$) [37]

$$-\ln W_{1,1} = \frac{4\pi}{3}\alpha_V [1 - 1.185\alpha_V] = 0.4931. \tag{4.6}$$

Clearly series expressed in terms of α_V have much better agreement with simulation results. Notice that α_V is about a factor of 2 larger (large renormalization) than the bare coupling α_0 at this value of β.

To incorporate the effects of renormalization we can define α directly in terms of a physical process. This is equivalent to **choosing a specific renormalization scheme**. A popular choice is the V-scheme which uses the static-quark potential $V(q)$ in momentum space [88, 65]. Let us consider the Wilson plaquette action as an example. The expansion of $V(q)$ to second order in α_0 is [89]

$$V(q) = -\frac{4}{3}\frac{4\pi\alpha_0}{q^2}\left[1 + \alpha_0\left(\beta_0 \ln\left(\frac{\pi}{aq}\right)^2 + 4.702\right) + \mathcal{O}(\alpha_0^2)\right], \tag{4.7}$$

where $\beta_0 = 11 - \frac{2}{3}n_f$. The large second order coefficient again indicates that α_0 is not a good expansion parameter. The renormalized coupling $\alpha_V(q)$ is defined such that

the potential has no higher-order corrections

$$V(q) \equiv -\frac{4}{3}\frac{4\pi\alpha_V(q)}{q^2}. \tag{4.8}$$

Therefore renormalization due to vacuum polarization is systematically included, resulting in a **running coupling** at scale q. Comparing (4.7) and (4.8), the relationship between α_0 and α_V, for the Wilson plaquette action, can be determined

$$\alpha_0 = \alpha_V(q)\left[1 - \alpha_V(q)\left(\beta_0 \ln\left(\frac{\pi}{aq}\right)^2 + 4.702\right) + \mathcal{O}(\alpha_V^2)\right]. \tag{4.9}$$

The connection between α_0 and α_V for the unimproved action and the MILC action is derived in [33] to third order (which requires a very difficult 2-loop perturbative calculation)

$$\alpha_0 = \alpha_V(q)\left[1 + v_1(q)\alpha_V(q) + v_2(q)\alpha_V^2(q)\right] + \mathcal{O}(\alpha_V^4). \tag{4.10}$$

The coefficients v_1, v_2 can be found in the reference given above. Perturbative quantities, e.g. $\ln W_{R,T}$, are then expanded in terms of $\alpha_V(q^*_{R,T})$ ((4.1) repeated here)

$$-\frac{\ln W_{R,T}}{2(R+T)} = c_1\alpha_V(q^*_{R,T}) + c_2\alpha_V^2(q^*_{R,T}) + c_3\alpha_V^3(q^*_{R,T}) + \mathcal{O}(\alpha_V^4). \tag{4.11}$$

The scale $q^*_{R,T}$ is called the "relevant scale", which is explained below.

Relevant Momentum Scale

The value of α_V also depends on the scale q at which it is evaluated (a running coupling constant). It is therefore necessary to determine the momentum scale relevant to the observable of interest. This momentum scale can be determined using the procedures described in Ref. [88]. The idea is to utilize the mean value theorem such that for 1-loop perturbative contributions

$$\int d^4q\alpha_s(q)f(q) \equiv \alpha_s(q^*)\int d^4q f(q). \tag{4.12}$$

This method essentially chooses the scale q^* such that $\alpha_s(q^*)$ mimics the use of the fully dressed gluon propagator within the process. To solve for q^*, we use the QCD

running coupling formula (to first order in perturbation theory) [2]

$$\begin{aligned}\alpha_V(q) &= \frac{\alpha_V(q^*)}{1+\beta_0\alpha_V(q^*)\ln\left(\frac{q^2}{q^{*2}}\right)} \\ &\approx \alpha_V(q^*) - \alpha_V^2(q^*)\beta_0 \ln\left(\frac{q^2}{q^{*2}}\right). \end{aligned} \tag{4.13}$$

Substituting the above equation into (4.12), we obtain a convenient formula for q^*

$$\ln\left(q^{*2}\right) = \frac{\int d^4q \ln(q^2) f(q)}{\int d^4q f(q)}. \tag{4.14}$$

The values of $q^*_{R,T}$ for Wilson loops are well known [65, 33]. They are listed in Table 6.1 in the next chapter.

Connection to $\alpha_s^{\overline{MS}}(M_Z)$

The final step is to convert the lattice result $\alpha_V(\frac{q^*}{a})$ to $\alpha_s^{\overline{MS}}(M_Z)$ so that it can be compared with other determinations (see Fig. 4.1). The connection between the "V-scheme" and the continuum $\overline{MS}$-scheme can be determined by expanding $V(q)$ in terms of $\alpha_{\overline{MS}}(q)$

$$V(q) \equiv -\frac{4}{3}\frac{4\pi\alpha_V(q)}{q^2} = -\frac{4}{3}\frac{4\pi}{q^2}\alpha_{\overline{MS}}(q)\left[1 + c_{1\overline{MS}}\alpha_{\overline{MS}}(q) + c_{2\overline{MS}}\alpha^2_{\overline{MS}}(q) + \mathcal{O}(\alpha^3_{\overline{MS}})\right] \tag{4.15}$$

where the coefficients can be found in Ref. [90]. This gives $\alpha_s^{\overline{MS}}(\frac{q^*}{a})$. Finally, to obtain $\alpha_s^{\overline{MS}}(M_Z)$, one numerically integrates the third order running coupling formula to the mass of the Z-boson [2]

$$\begin{aligned}\alpha(q) &= \frac{4\pi}{\beta_0\ln(q^2/\Lambda^2)}\left[1 - \frac{\beta_1}{\beta_0^2}\frac{\ln[\ln(q^2/\Lambda^2)]}{\ln(q^2/\Lambda^2)} + \frac{\beta_1^2}{\beta_0^4\ln^2(q^2/\Lambda^2)}\right. \\ &\quad \left.\times\left(\left(\ln\left[\ln(q^2/\Lambda^2)\right] - \frac{1}{2}\right)^2 + \frac{\beta_2\beta_0}{\beta_1^2} - \frac{5}{4}\right)\right], \end{aligned} \tag{4.16}$$

where Λ is a constant of integration. Here $\beta_0 = 11 - \frac{2}{3}n_f$ and $\beta_1 = 102 - \frac{38}{3}n_f$ are universal constants. The value of β_2, however, is scheme dependent. In the $\overline{MS}$-scheme it reads $\beta_2^{\overline{MS}} = \frac{2857}{2} - \frac{5033}{18}n_f + \frac{325}{54}n_f^2$, and in the V-scheme $\beta_2^V = 4224.18 - 746.006n_f + 20.8719n_f^2$ [90].

Chapter 5

Lattice Perturbation Theory from Monte Carlo Simulations at Weak Coupling

The key ingredients in the determination of $\alpha_s^{\overline{MS}}(M_Z)$ are the expansions of Wilson loops (4.1). So far the perturbative coefficients have only been computed analytically [33]. However, as we have discussed in the introduction, diagrammatic perturbation theory is very difficult for lattice actions, which have very complicated Feynman rules. One has to evaluate an enormous number of diagrams for higher-order calculations.

A simpler alternative to analytic perturbation theory, proposed in Ref. [35], is to simulate the quantity of interest at weak coupling [1] (or at high β) where QCD is perturbative, and fit perturbative expansions to the results. The 1-loop mass renormalization for Wilson fermions was correctly reproduced. This method was later applied to determine the perturbative coefficients of Wilson loops, through third order, of the Wilson plaquette action [37]. Excellent agreement with analytic perturbation theory was obtained. The tadpole improvement factor was studied at high β in Ref. [38]. Results agree with the existing 2-loop calculations and new prediction for the 3-loop perturbative coefficient was made.

In this project we extend the calculation of Ref. [37] to compute the perturbative coefficients of the Wilson loops in *full* QCD, for the unimproved action and the MILC action. This is the first time that the Monte Carlo method is applied to full QCD

[1] Remember that $\alpha = \frac{g^2}{4\pi} = \frac{6}{4\pi\beta}$, see (2.5).

lattice actions. All previous studies listed above were done for pure gauge theories where contributions from dynamical fermions had been neglected.

It is important to work at high enough β or small coupling so higher-order contributions are negligible, i.e., we are in the perturbative phase. The typical value of β used in simulations is $\beta \approx 6.0$, which gives a lattice spacing $a \approx 0.1$fm and $\alpha_V(q^*_{1,1}) \approx 0.14$ (see (4.6)). In this project we use couplings ranging from $\beta = 9.5$ to $\beta = 80.0$. For $\beta = 9.5$, we have $a \approx 0.02$fm and $\alpha_V(q^*_{1,1}) \approx 0.12$ (see Table 6.8 in next chapter), and at $\beta = 13.5$ the lattice spacing gets even smaller, $a \approx 0.005$fm and $\alpha_V(q^*_{1,1}) \approx 0.076$ [2]. At $\beta = 80.0$, the lattice spacing becomes infinitesimally small $a \approx 10^{-17}$fm, and $\alpha_V(q^*_{1,1}) \approx 0.01$. This lattice spacing is comparable to the Planck scale (about 10^{-20}fm [1])! Therefore any measured effects are far away from the confined phase of the theory, and well into the perturbative phase.

Finally we should mention that, although we develop our own computer programs in this project, simulation codes are publicly available (e.g., the MILC code developed by the MILC collaboration), and in principle one only has to perform the simulations.

While perturbative coefficients can be computed more efficiently with high-β simulations, at least for simple quantities like Wilson loops, this method produces perturbative coefficients with statistical errors and truncation errors so it is not a complete substitute for conventional perturbation theory. Additionally, numerical simulations are subject to various systematic effects. There are three major sources of errors: i) zero momentum modes (or finite size effects), ii) tunneling between the Z_3 center phases, and iii) errors in the simulation equations. An extensive study of these systematic effects will be presented in this chapter.

In Section 5.1, we will first discuss the problems with zero-momentum modes and tunneling. Zero modes contribute a large part of finite size effects while tunneling gives non-perturbative contributions. Twisted boundary conditions are employed in the present project to remove both of these effects. This will be discussed in Section 5.2. Simulation algorithms will be reviewed in Section 5.3. A new algorithm, the rational hybrid Monte Carlo (RHMC) algorithm [40], with no finite step size (Δt) error, is used for the unimproved action. This is the first time this algorithm has been used in a numerical application. However, RHMC is computationally much more expensive and is impractical to apply to highly improved actions such as the MILC action. In

[2]The lattice spacings are estimated using the data in Table 3.1. Near the continuum limit the lattice spacing scales like $a \sim e^{-k\beta}$ where k is a constant [22].

that case we use the R-algorithm [41], which has step size errors of Δt^2. Simulations are done at several values of Δt and results are extrapolated to $\Delta t = 0$. Finally, other systematic effects will be addressed in Section 5.4.

A comment should be made here about the precision of our data. The objective of this project is to extract the perturbative coefficients of Wilson loops from Monte Carlo simulations and to compare the results with the analytic calculation of Ref. [33]. We wish to do the comparison at least through third order. Given $\alpha_V \sim \mathcal{O}(0.01)$ for the values of β used in this project, the Wilson loops therefore must be determined with statistical precision of 10^{-5}–10^{-6}! Hence it is important to identify all possible systematic effects and to have them under control.

5.1 Zero Modes and Tunneling

Zero Momentum Modes

The measurement of Wilson loops on a finite-size lattice is subject to finite volume effects. A large part of the effect shows up as large zero-momentum contributions in the perturbative expansion. This is best illustrated by the loop integral of the free gluon propagator. For infinite lattice volume it is well behaved

$$\int_{-\pi/a}^{\pi/a} \frac{d^4p}{\hat{p}^2} = \text{finite}, \quad \hat{p}^2 = 4\sin^2\frac{p}{2}. \tag{5.1}$$

On the other hand if the lattice has finite size, $V = L^4 = (aN)^4$, the momentum is discrete and the integral becomes a sum

$$\sum_p \frac{1}{\hat{p}^2}, \quad p_\mu = \frac{2\pi n_\mu}{L} \text{ with } n_\mu = 0, \ldots, N-1. \tag{5.2}$$

Clearly the zero-momentum mode $p = 0$ creates problem.

A proper treatment of zero-momentum modes is a very complicated problem [91]. Therefore their contributions are usually neglected in finite-lattice perturbation theory. This is not perfect but the error introduced can be shown to vanish as $1/V$ in the infinite volume limit [91]. The simplest procedure is to simply neglect these effects (e.g., by not including the $p = 0$ term in the momentum sums, see Ref. [87] and references therein). Another approach, proposed by Lüscher and Weisz [34], is

to remove zero modes from the start by using twisted boundary conditions instead of periodic boundary conditions. We will see explicitly how this works in the next section.

For proper comparison with diagrammatic perturbation theory one must use the same boundary conditions in simulations as used in the analytic calculations (see next chapter for a detailed discussion on the matching of the results obtained in the present project and those in Ref. [33]). Only minor modifications of the computer codes are required when switching from periodic boundary conditions to twisted boundary conditions.

Tunneling

The gauge field action is invariant under the transformation for which all μ-directional links on a μ-plane (i.e., a fixed x_μ) pick up a *common* element from the center subgroup Z_3 of SU(3)

$$U_{x,\mu} \to Z U_{x,\mu}, \quad \text{on a particular } \mu\text{-plane}, \tag{5.3}$$

where $Z \in Z_3 = [\mathbb{I}, e^{i2\pi/3}\mathbb{I}, e^{i4\pi/3}\mathbb{I}]$. Let us consider the Wilson plaquette action as an example (see Fig. 5.1). For those plaquettes affected by the transformation (5.3), the extra phases on the opposite sides cancel leaving the action unchanged. This symmetry causes the gauge-field action minimum to be degenerate. The transition between the degenerate ground states in the from of (5.3) is known as "tunneling".

Perturbative calculations can be performed around *any* one of the three vacuum configurations. The usual one is defined by $U_{x,\mu} \approx \mathbb{I}$. Tunneling effect, however, is non-perturbative because the value of the gauge fields shifts by a constant factor during the transition (remember $U_{x,\mu} \equiv e^{iag\tilde{A}_\mu(x)}$)

$$A_\mu(x) \to Z + A_\mu(x). \tag{5.4}$$

Tunneling can occur quite frequently in numerical simulations (see below and Fig. 5.2). These non-perturbative events must be sufficiently suppressed to allow extraction of the desired perturbative effects.

Tunneling between the Z_3 phases can be detected by measuring the Polyakov loop

$$P_\mu = \frac{1}{L^3} \sum_{x, x_\mu = 1} \frac{1}{3} \mathrm{Tr}\left[U_{x,\mu} U_{x+\hat{\mu},\mu} \ldots U_{x+L\hat{\mu},\mu}\right], \tag{5.5}$$

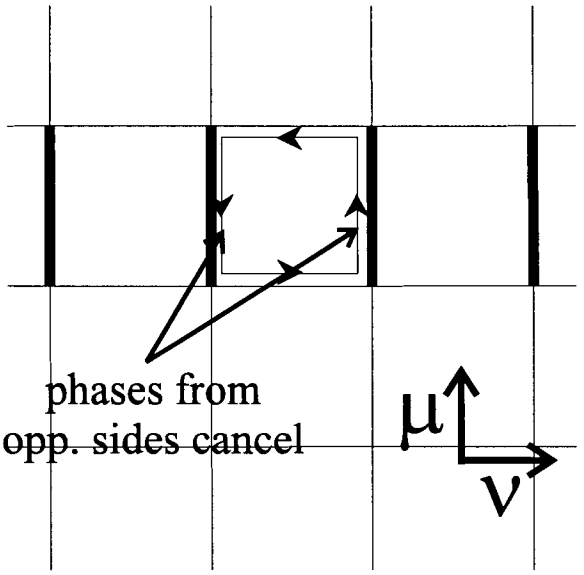

Figure 5.1: Example of tunneling for the Wilson plaquette action. The bold lines represent links that have transformed. The extra phases on the opposite sides cancel leaving the action unchanged.

which is the product of all links in the μ-direction. Since the Polyakov loop cuts through a particular plane only once, it picks up an extra phase factor (1, $e^{i2\pi/3}$, $e^{i4\pi/3}$) when tunneling occurs. A typical run history of the temporal Polyakov loop P_t is given in Fig. 5.2 for the unimproved action (i.e., with unimproved staggered quark action) at $\beta = 16$. Periodic boundary conditions are used in this case and the lattice volume is $V = 4^4$. The input bare mass is $m = 0.1$ with $n_f = 1$. Except for the volume [3], these parameters are the same as those used in next chapter. Unfortunately, one can observe that tunneling is very severe at this β and volume.

One method to suppress tunneling is to work at very large values of β or very large lattice volumes. Tunneling is more difficult at large β because fluctuations in gauge fields reduce as β increases. On the other hand more links have to be transformed on larger lattices so tunneling is also suppressed. However, the example that we gave above is already at relatively high β. We use a larger volume in the simulations, $V = 8^4$, but it has been seen that tunneling is still very severe at this volume. Increasing the volume further is not feasible because simulation cost scales as $\left(\frac{L}{a}\right)^6$, see Section 1.1. A more efficient method must therefore be utilized. We will see in the next section that tunneling can be strongly suppressed if twisted boundary conditions

[3]The actual simulations are done on $V = 8^4$ lattices.

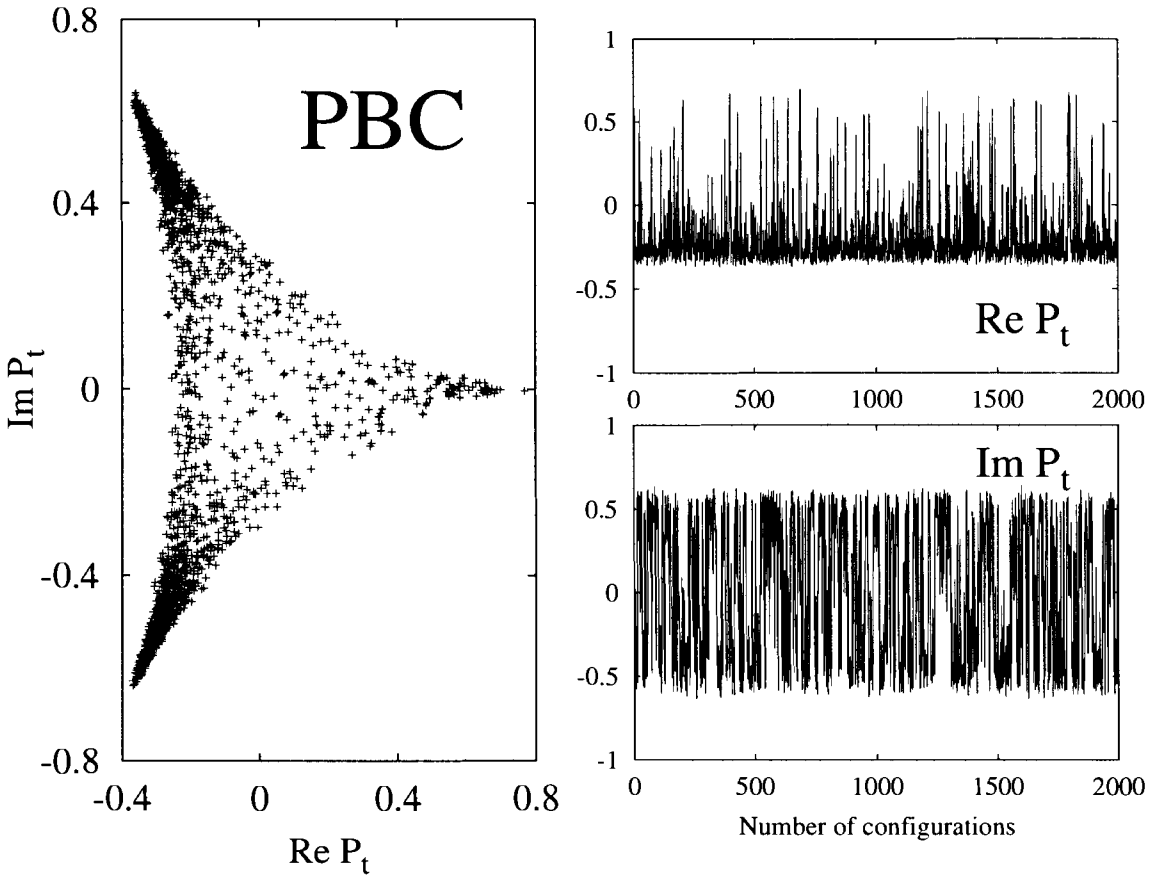

Figure 5.2: Run history and scatter diagram of the temporal Polyakov loop P_t on a 4^4 lattice at $\beta = 16$ using periodic boundary conditions. Results are obtained with the unimproved action (i.e., with unimproved staggered quark action) and 100 configurations are skipped between measurements.

are used.

We should mention that the presence of fermions breaks the Z_3 symmetry as the fermion actions are not invariant under the transformation (5.3). However, at small volumes and modest β, the cost of forming different phases is too small to prevent their frequent occurrence, as can be inferred in Fig. 5.2.

5.2 Twisted Boundary Conditions

Simulations usually employ periodic boundary conditions (PBC)

$$U_{x+L\hat{\nu},\mu} = U_{x,\mu}, \quad \psi_{x+L\hat{\nu}} = \psi_x, \tag{5.6}$$

where L is the size of the lattice. For twisted boundary conditions (TBC), extra twist matrices Ω_ν are inserted when one steps over the boundary

$$U_{x+L\hat{\nu},\mu} = \Omega_\nu U_{x,\mu}\Omega_\nu^\dagger, \quad \psi_{x+L\hat{\nu}} = e^{i\pi/3}\Omega_\nu \psi_x \Omega_\nu^\dagger. \tag{5.7}$$

In this project TBC are applied to spatial directions only and the temporal direction is not twisted. The twist matrices Ω_ν are fixed traceless elements of SU(3) group satisfying

$$\Omega_\mu\Omega_\nu = z\Omega_\nu\Omega_\mu, \quad z \equiv e^{i2\pi/3} \tag{5.8}$$

and

$$\Omega_\nu^3 = \mathbb{I}. \tag{5.9}$$

The first relation makes certain that $U_{x,\mu}$ is uniquely defined for those lying outside more than one boundary (i.e., independent of which boundary is crossed first)

$$\begin{aligned} U_{x+L\hat{\mu}+L\hat{\nu},\rho} &= \Omega_\mu\Omega_\nu U_{x,\rho}\Omega_\nu^\dagger\Omega_\mu^\dagger \\ &= \Omega_\mu\Omega_\nu U_{x,\rho}(\Omega_\mu\Omega_\nu)^\dagger \\ &= zz^*\Omega_\nu\Omega_\mu U_{x,\rho}(\Omega_\nu\Omega_\mu)^\dagger \\ &= \Omega_\nu\Omega_\mu U_{x,\rho}\Omega_\mu^\dagger\Omega_\nu^\dagger. \end{aligned} \tag{5.10}$$

The second condition implies that there is a periodicity of $3L$ in the twist direction for the link variables

$$U_{x+3L\hat{\nu},\mu} = \Omega_\nu^3 U_{x,\mu}{\Omega_\nu^\dagger}^3 = U_{x,\mu}. \tag{5.11}$$

On the other hand, the additional factor $e^{i\pi/3}$ in (5.7) ensures anti-periodicity for the fermion field

$$\psi_{x+3L\hat{\nu}} = -\psi_x. \tag{5.12}$$

These indicate that the length of the lattice is effectively tripled in the directions where TBC have been employed, and therefore one would expect to have smaller

finite size effects. The following representation of Ω_ν is used in this project [4]

$$\Omega_x = \begin{bmatrix} 0 & 1 & 0 \\ 0 & 0 & 1 \\ 1 & 0 & 0 \end{bmatrix}, \quad \Omega_y = \begin{bmatrix} e^{-i2\pi/3} & 0 & 0 \\ 0 & 1 & 0 \\ 0 & 0 & e^{+i2\pi/3} \end{bmatrix}, \quad \Omega_z = \Omega_x^2 \Omega_y = \begin{bmatrix} 0 & 0 & e^{-i2\pi/3} \\ 1 & 0 & 0 \\ 0 & e^{+i2\pi/3} & 0 \end{bmatrix}. \tag{5.13}$$

Note that only Ω_x and Ω_y are independent.

Because the twist is applied in a bilinear manner, the quark fields ψ_x must become 3×3 matrices similar to the link variables. Hence in addition to the SU(3) colour group, a SU(3) "smell group" is needed [92]. The three "smells" are degenerate like the colours. These extra degrees of freedom can again be identified as quark flavours. This is analogous to what we have done in the staggered quark formalism where doubler modes are treated as quark flavours. As a result, the same theory will describe $3n_f$ quark species if TBC are employed instead of PBC. Note the simulation cost is tripled. This is one disadvantage of TBC for dynamical fermions.

Twisted Boundary Conditions and Zero Modes (Gauge Field)

The use of TBC in simulations can completely remove the zero-momentum modes of both the gauge field $\tilde{A}_\mu(x)$ and the quark field $\psi(x)$. Let us consider the former case first. Since $U_{x,\mu} \equiv e^{iag\tilde{A}_\mu(x)}$, $\tilde{A}_\mu(x)$ satisfies the TBC (5.7) also

$$\tilde{A}_\mu(x + L\hat{\nu}) = \Omega_\nu \tilde{A}_\mu(x) \Omega_\nu^\dagger. \tag{5.14}$$

Now Fourier expansion gives

$$\tilde{A}_\mu(x) = \frac{1}{L^4} \sum_k \Gamma_k e^{ikx} e^{ik_\mu/2} A_\mu(k). \tag{5.15}$$

The extra factor $e^{ik_\mu/2}$ can be interrupted as defining the field $\tilde{A}_\mu(x)$ to sit in the middle between x and $x + \hat{\mu}$. For PBC, the matrices Γ_k would be the standard generators t^a of the SU(3) colour group and are independent of the momentum k. There would be a summation over colours, $\sum_a$, and there would be 8 independent

[4] The representation is not unique.

colour fields $A^a_\mu(k)$, $a = 1, \ldots, 8$. For TBC, however, there is an interesting mixing between colours and momentum. As we will see shortly, the colour degrees of freedom are transformed to momentum degrees of freedom. There will be 8 times more momentum vectors when TBC are used.

Applying (5.14) to (5.15), we have

$$\begin{aligned} \frac{1}{L^4}\sum_k \Gamma_k e^{ikx} e^{ik_\nu L} e^{ik_\mu/2} A_\mu(k) &= \frac{1}{L^4}\sum_k \Omega_\nu \Gamma_k \Omega_\nu^\dagger e^{ikx} e^{ik_\mu/2} A_\mu(k) \\ \therefore \quad e^{ik_\nu L}\Gamma_k &= \Omega_\nu \Gamma_k \Omega_\nu^\dagger. \end{aligned} \tag{5.16}$$

Multiply the above equation on the left by Ω_ν^2 and on the right by $\Omega_\nu^{\dagger 2}$, and use $\Omega_\nu^3 = \mathbb{I}$, we obtain

$$\begin{aligned} \Gamma_k &= e^{ik_\nu L}\Omega_\nu \left(\Omega_\nu \Gamma_k \Omega_\nu^\dagger\right) \Omega_\nu^\dagger \\ &= e^{i2k_\nu L}\left(\Omega_\nu \Gamma_k \Omega_\nu^\dagger\right) \\ &= e^{i3k_\nu L}\Gamma_k. \end{aligned} \tag{5.17}$$

This gives a quantization condition for the momentum

$$k_\nu = \frac{2\pi n_\nu}{3L}, \quad n_\nu = 0, \ldots, L. \tag{5.18}$$

The momentum appears to be quantized in a box with length $3L$ instead of the physical length L. This again indicates that the length of the lattice is effectively increased by a factor of 3. Substituting (5.18) back into (5.16), gives

$$\begin{aligned} e^{i\frac{2\pi n_\nu}{3}}\Gamma_k &= \Omega_\nu \Gamma_k \Omega_\nu^\dagger, \quad \text{or} \\ z^{n_\nu}\Gamma_k &= \Omega_\nu \Gamma_k \Omega_\nu^\dagger. \end{aligned} \tag{5.19}$$

Equation (5.19) can be solved by making the ansatz

$$\Gamma_k = \Omega_x^\alpha \Omega_y^\beta \Omega_z^\gamma = \Omega_x^{\alpha+2\gamma}\Omega_y^{\beta+\gamma}, \tag{5.20}$$

where α, β and γ are integers and we have used $\Omega_z = \Omega_x^2\Omega_y$, see (5.13). Since there are only two independent matrices, Ω_x and Ω_y, there are only two free variables, $(\alpha + 2\gamma)$

and $(\beta+\gamma)$. Substituting this ansatz into (5.19), we have, for $\nu = x$,

$$\begin{aligned} z^{n_x}\Gamma_k &= \Omega_x \Gamma_k \Omega_x^\dagger \\ &= \Omega_x^{\alpha+2\gamma+1}\Omega_y^{\beta+\gamma}\Omega_x^\dagger \\ &= z^{\beta+\gamma}\Omega_x^{\alpha+2\gamma}\Omega_y^{\beta+\gamma} \\ &= z^{\beta+\gamma}\Gamma_k \\ \therefore \quad \beta+\gamma &= n_x. \end{aligned} \tag{5.21}$$

Similarly, for $\nu = y$ and $\nu = z$

$$\alpha + 2\gamma = -n_y, \quad n_z = 2n_x - n_y. \tag{5.22}$$

Hence the Γ_k matrices are given by

$$\Gamma_k = \Omega_x^\alpha \Omega_y^\beta \Omega_z^\gamma = \Omega_x^{-n_y}\Omega_y^{n_x}. \tag{5.23}$$

Because $\Omega_\nu^3 = \mathbb{I}$, there are 9 distinct Γ_k only: eight traceless Hermitian matrices and the identity.

In summary, the Fourier decomposition of $\tilde{A}_\mu(x)$ is

$$\tilde{A}_\mu(x) = \frac{1}{L^4}\sum_k \Omega_x^{-n_y}\Omega_y^{n_x} e^{ikx} e^{ik_\mu/2} A_\mu(k), \tag{5.24}$$

and the momentum vectors are

$$\begin{cases} k_\mu = \frac{2\pi n_\mu}{3L}, & n_\mu = 0,\ldots,3L-1 \text{ for } \mu = x,y \\ & n_z = 2n_x - n_y \\ k_t = \frac{2\pi n_t}{L}, & n_t = 0,\ldots,L \end{cases} . \tag{5.25}$$

The condition that $\tilde{A}_\mu(x)$ is traceless excludes the case $\Omega_x^{-n_y}\Omega_y^{n_x} = \mathbb{I}$. This corresponds to $n_x = n_y = n_z = 0 \pmod 3$, i.e., **zero modes are eliminated**.

In addition, there are precisely 8 times more momentum degrees of freedom compared to the case when PBC are used [5]. For each momentum mode $\tilde{A}_\mu(k)$, however, the colour is fixed. There is only one Γ_k matrix associated with each $\tilde{A}_\mu(k)$. These

[5]Equation (5.25) indicates that there are 9 times more momentum vectors but we cannot have zero modes $n_x = n_y = n_z = 0 \pmod 3$.

show that **the original colour degrees of freedom become momentum degrees of freedom**. In the present case with SU(3) colour, there are 8 times more momenta because the colour group has 8 generators.

Twisted Boundary Conditions and Zero Modes (Quark Field)

Zero-momentum modes of the quark fields cannot be eliminated by the traceless requirement. Instead they are removed by the anti-periodicity condition (5.12) as we will see below.

Again, expand $\psi(x)$ into momentum modes

$$\psi(x) = \frac{1}{L^4}\sum_k \Gamma_k e^{ikx}\psi(k). \tag{5.26}$$

Remember that $\psi(x)$ is now a 3×3 matrix. Applying TBC (5.7) to those $\psi(x)$ that lie outside the boundary, gives

$$\begin{aligned} \psi_{x+L\hat{\nu}} &= e^{i\pi/3}\Omega_\nu \psi_x \Omega_\nu^\dagger \\ \frac{1}{L^4}\sum_k \Gamma_k e^{ikx}e^{ik_\nu L}\psi(k) &= \frac{1}{L^4}\sum_k \Gamma_k e^{ikx}e^{i\pi/3}\Omega_\nu\psi(k)\Omega_\nu^\dagger \\ \therefore \quad e^{ik_\nu L}\Gamma_k &= e^{i\pi/3}\Omega_\nu\Gamma_k\Omega_\nu^\dagger. \end{aligned} \tag{5.27}$$

Again, multiply the above equation on the left by Ω_ν^2 and on the right by $\Omega_\nu^{\dagger 2}$, we obtain

$$\begin{aligned} e^{ik_\nu L}\Omega_\nu\left(\Omega_\nu\Gamma_k\Omega_\nu^\dagger\right)\Omega_\nu^\dagger &= e^{i\pi/3}\Gamma_k \\ e^{i2k_\nu L}\left(\Omega_\nu\Gamma_k\Omega_\nu^\dagger\right) &= e^{i2\pi/3}\Gamma_k \\ \therefore \quad e^{i3k_\nu L}\Gamma_k = -\Gamma_k. \end{aligned} \tag{5.28}$$

This implies the quantization condition

$$k_\nu = \frac{2\pi}{3L}\left(n_\nu + \frac{1}{2}\right), \quad n_\nu = 0,\ldots,3L-1. \tag{5.29}$$

Therefore **there are no zero-momentum modes for the quark fields**. Again, the momentum seems to be quantized in a box with length $3L$.

Twisted Boundary Conditions and Tunneling

We have mentioned that tunneling can be suppressed by increasing the volume of the lattice because more links have to be transformed simultaneously. The quantization conditions (5.18) and (5.29) indicate that the lattice size is effectively tripled in the directions where TBC has been applied. Therefore one might expect to see less tunneling with TBC. This is demonstrated in Fig. 5.3 and 5.4 where TBC have been applied to two directions (TBC_{xy}) and three directions (TBC_{xyz}) respectively. For comparison simulation parameters are chosen to be the same as those used in Fig. 5.2. It can be observed that tunneling has already almost disappeared with two-way twist and there is no tunneling at all with TBC_{xyz}. In this project TBC are applied to all three spatial directions, i.e., TBC_{xyz}. We have generated about 1 Million configurations ($V = 8^4$) and not even a single tunneling event has been observed.

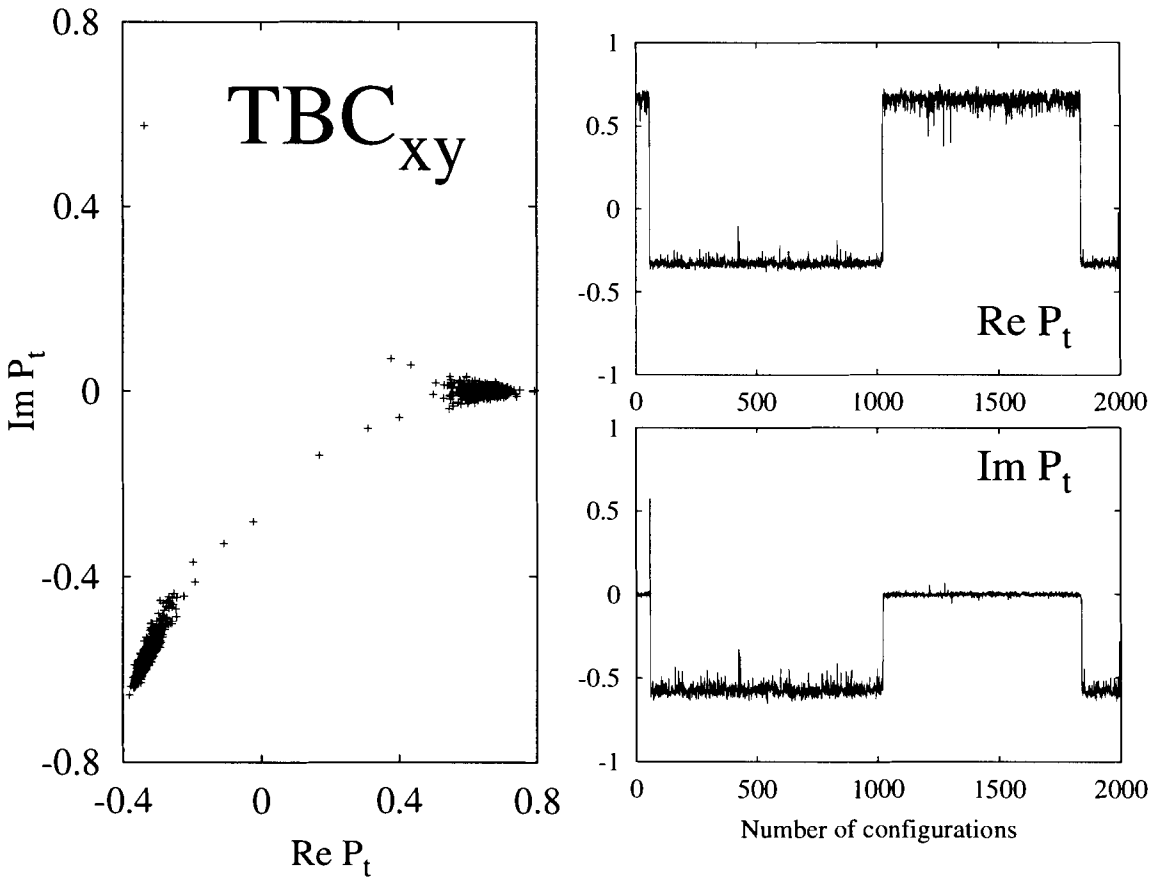

Figure 5.3: Run history and scatter diagram of the temporal Polyakov loop P_t at $\beta = 16$, $V = 4^4$ with xy-twist. Parameters are the same as those of Fig. 5.2.

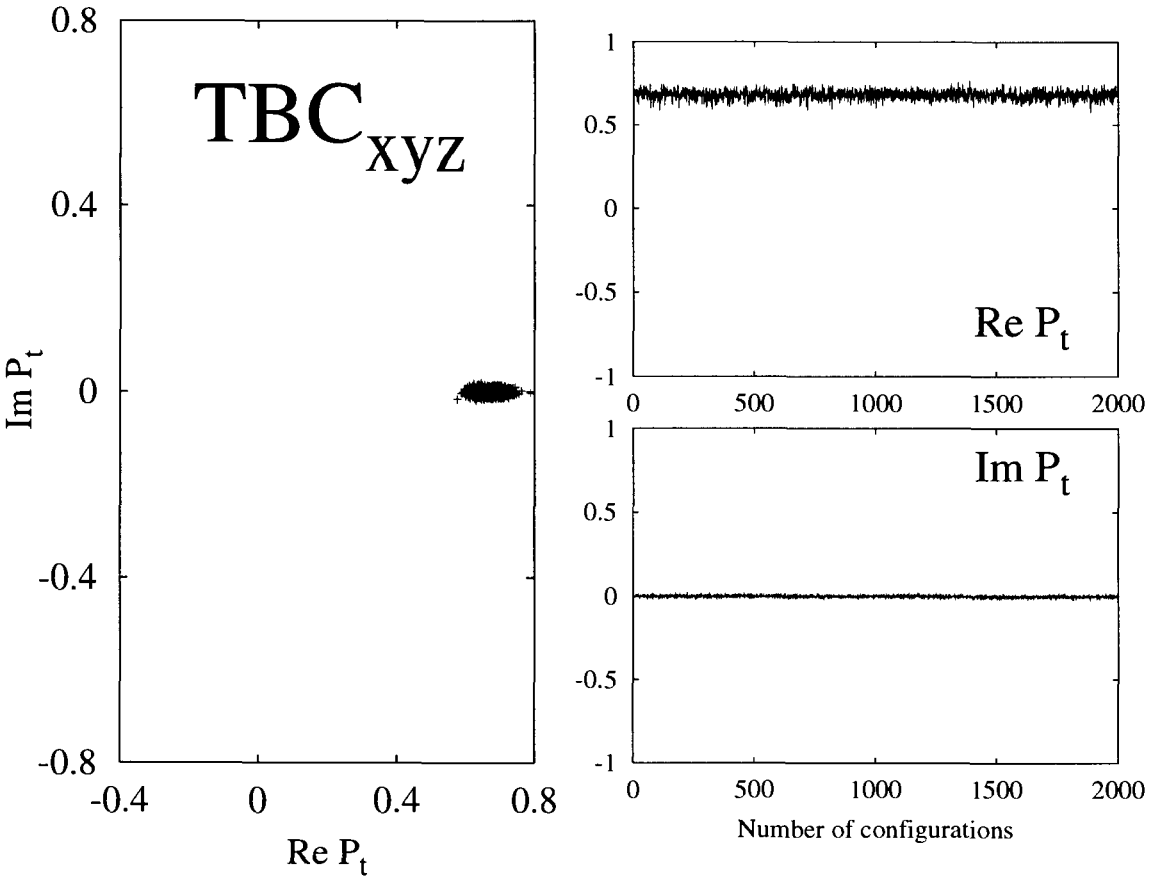

Figure 5.4: Same as Fig. 5.2 and 5.3 but with xyz-twist.

5.3 Simulation Algorithms

We want to compute the ensemble average of the Wilson loop $W_{R,T}$

$$\begin{aligned} \langle W_{R,T} \rangle &= \frac{1}{Z} \int DUD\phi W_{R,T} e^{-S} \\ &= \frac{1}{Z} \int DUD\phi W_{R,T} e^{-S_G - \phi^\dagger \left[M^\dagger M\right]^{-n_f/12} \phi}, \end{aligned} \tag{5.30}$$

where S_G is the gauge field action and M is the staggered quark matrix [6], see (2.18). Note that we have taken the 12-th root of $\det M$ which gives $e^{-\phi^\dagger \left[M^\dagger M\right]^{-n_f/12} \phi}$. This is because twisted boundary conditions introduce an extra SU(3) "smell" group. Therefore $\det M$ describes 12 fermion species, instead of 4 in the case when periodic bound-

[6] From now on we drop the superscript "sf" on M.

ary conditions are used. The partition function is

$$Z = \int DUD\phi D\phi^{\star} e^{-S_G - \phi^{\dagger}\left[M^{\dagger}M\right]^{-n_f/12}}. \tag{5.31}$$

The number of variables is enormous even on a relatively small lattice, e.g. 10^4, with SU(3) links: there are 4×10^4 links and each link has 8 real parameters so that the total number of degrees of freedom is about 320,000. Clearly, a direct numerical integration is impractical and one must use statistical methods to evaluate the expectation value.

Because of the exponential decay in the integrand, only a small number of configurations with a small action will give appreciable contributions to the partition function. Hence an efficient way of computing the ensemble average would be to generate a sample of configurations with Boltzmann distribution e^{-S}, and replace (5.30) with the sample average

$$\langle W_{R,T} \rangle \approx \frac{1}{N} \sum_{i=1}^{N} (W_{R,T})_i \,, \tag{5.32}$$

where N is the sample size and $(W_{R,T})_i$ is the Wilson loop measured with the i-th configuration in the sample. This technique is known as "important sampling".

Many algorithms have been designed to generate configurations with the desired distribution. We use the rational hybrid Monte Carlo (RHMC) algorithm [40] in the unimproved case and the R-algorithm [41] for the MILC action. The basis of these algorithms is a set of *discretized* equations of motion. The system is evolved through the phase space using these equations along a "simulation time t" with step size Δt. Since the evolution equations are not exact, there will be a small error in the distribution $e^{-S+\Delta S}$. This systematic error is corrected by a Monte Carlo accept/reject step [93] in the RHMC algorithm so that the algorithm is *exact*. However RHMC is computationally much more expensive and can only be applied to actions with a simple structure. For more complicated actions such as the MILC action the R-algorithm is often used. This algorithm has a disadvantage that it cannot be made exact by a Monte Carlo accept/reject step. The error is $\Delta S = \mathcal{O}(\Delta t^2)$. It is therefore necessary to do simulations at several different Δt and extrapolate the results to $\Delta t = 0$.

The RHMC algorithm has so far only been used in small test cases [40, 94] and has never been applied to large scale dynamical simulations. This project therefore is the *first* application of the algorithm. Our results will also serve as an important benchmark for future simulations.

Some Basic Ideas: the Hybrid Monte Carlo (HMC) Method

The RHMC algorithm and the R-algorithm are variants of the Hybrid Monte Carlo (HMC) method [93] so let us review some of the basics of this algorithm first. The central idea of HMC is to rewrite (5.31) as the partition function of a *classical statistical system* so that configurations can be generated using the classical equations of motion. More explicitly, by introducing a momentum field $P_{x,\mu}$ conjugate to the link variables $U_{x,\mu}$

$$\dot{U}_{x,\mu} = iP_{x,\mu}U_{x,\mu}, \tag{5.33}$$

we obtain

$$\begin{aligned} Z &= \int DPDUD\phi e^{-\left[\frac{1}{2}\mathrm{tr}P^2+S\right]}, \quad \mathrm{tr}P^2 = \sum_{x,\mu}\mathrm{tr}P_{x,\mu}^2 \\ &= \int DPDUD\phi e^{-\mathcal{H}}, \end{aligned} \tag{5.34}$$

where $\mathcal{H}$ is the Hamiltonian of our new statistical system. This is a 5-dimensional problem: the time derivative in (5.33) is with respect to the "simulation time" and the four space-time dimensions of the original lattice become the 4 spatial dimensions of the new system. Note that $P_{x,\mu}$ is traceless and Hermitian so that it can be written as $P_{x,\mu} = \sum_a p_{x,\mu}^a t^a$ where t^a are the generators of the SU(3) colour group. The HMC algorithm consists of three major components:

1) **Molecular dynamics evolution**. The advantage of changing to a classical statistical problem is that we can use the classical (discretized) equations of motion to move through the configuration space efficiently, $[U,P]\,|_{t=0} \rightarrow [U,P]\,|_{t=T}$, on a *constant "energy" surface* [7] (see Fig. 5.5)

- initial half step for P

$$P(\frac{\Delta t}{2}) = P(0) + \frac{\Delta t}{2}\dot{P}(t) + \mathrm{O}(\Delta t^2) \tag{5.35}$$

- $n_{md} = \frac{T}{\Delta t}$ times leapfrog integration

$$\begin{cases} U(t+\Delta t) = e^{iP(t+\frac{\Delta t}{2})\Delta t}U(t) + \mathrm{O}(\Delta t^3) \\ P(t+\frac{\Delta t}{2}) - P(t-\frac{\Delta t}{2}) = \dot{P}(t)\Delta t + \mathrm{O}(\Delta t^3) \end{cases} \tag{5.36}$$

[7] The word energy is in quotations because it is the energy of the statistical system and not the energy of the quantum system. From (5.34) the action of the quantum system is allowed to fluctuate.

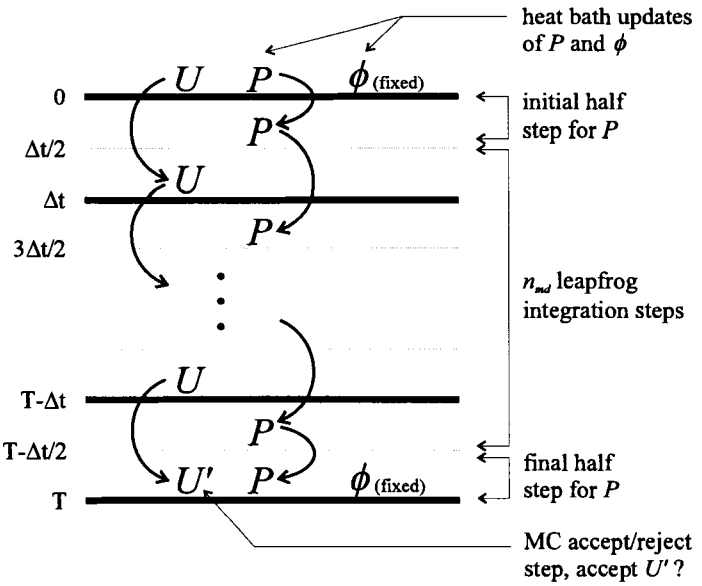

Figure 5.5: The HMC algorithm. Note that the pseudo-fermion field ϕ is held fixed during the integration.

- final half step for P

$$P(T) = P(T - \frac{\Delta t}{2}) + \frac{\Delta t}{2}\dot{P}(T) + \mathrm{O}(\Delta t^2). \tag{5.37}$$

Note that the pseudo-fermion field ϕ is held fixed during the integration. To get $\dot{P}_{x,\mu}$ we use the constraint $\dot{\mathcal{H}} = 0$

$$\begin{aligned} &\frac{d}{dt}\left[\frac{1}{2}\mathrm{tr}P^2 + S_g + \phi^\dagger (M^\dagger M)^{-n_f/12}\phi\right] = 0 \\ \therefore \quad &\sum_{x,\mu} \mathrm{tr}\left[P_{x,\mu}\dot{P}_{x,\mu} + \frac{\partial S_g}{\partial U_{x,\mu}}\dot{U}_{x,\mu} + \frac{\partial \langle\phi|(M^\dagger M)^{-n_f/12}|\phi\rangle}{\partial U_{x,\mu}}\dot{U}_{x,\mu} + h.c.\right] = 0. \end{aligned} \tag{5.38}$$

Using (5.33) we have

$$\begin{aligned} &\sum_{x,\mu} \mathrm{tr}\left[P_{x,\mu}\left(\dot{P}_{x,\mu} + iU_{x,\mu}\left(\frac{\partial S_g}{\partial U_{x,\mu}} + \frac{\partial \langle\phi|(M^\dagger M)^{-n_f/12}|\phi\rangle}{\partial U_{x,\mu}}\right) + h.c.\right)\right] = 0 \\ &\therefore \quad \dot{P}_{x,\mu} = \left[2iU_{x,\mu}\left(\frac{\partial S_g}{\partial U_{x,\mu}} + \frac{\partial \langle\phi|(M^\dagger M)^{-n_f/12}|\phi\rangle}{\partial U_{x,\mu}}\right)\right]_{TH}. \end{aligned} \tag{5.39}$$

Here $[A]_{TH}$ denotes the traceless-Hermitian part of the matrix A. The purpose of this step is to keep $P_{x,\mu}$ traceless and Hermitian so to maintain the unitarity of U

throughout the integration. Note that under TH the Hermitian conjugates ($h.c.$) simply give an extra factor of 2. The derivative of the gauge field action $\frac{\partial S_g}{\partial U_{x,\mu}}$ can be easily computed

$$\begin{aligned}\frac{\partial S_g}{\partial U_{x,\mu}} &= -\frac{\partial}{U_{x,\mu}}\left[\beta_{pl}\sum_{y,\mu<\nu}P_{\mu\nu}(y)+\beta_{rt}\sum_{y,\mu\neq\nu}R_{\mu\nu}(y)+\beta_{cu}\sum_{y,\mu<\nu<\sigma}C_{\mu\nu\sigma}(y)\right]\\ &= -\frac{1}{6}\left[\beta_{pl}V^P_{x,\mu}+\beta_{rt}V^R_{x,\mu}+\beta_{cu}V^C_{x,\mu}\right], \qquad (5.40)\end{aligned}$$

where $V^P_{x,\mu}$, $V^R_{x,\mu}$ and $V^C_{x,\mu}$ are the plaquette, rectangle and the cubic chair term without the link $U_{x,\mu}$. For example, $V^P_{x,\mu}$ contains the six staples connected to $U_{x,\mu}$. For $\boldsymbol{n_f = 12}$ the fermionic force is given by

$$\begin{aligned}\frac{\partial}{\partial U_{x,\mu}}\langle\phi|(M^\dagger M)^{-1}|\phi\rangle &= \langle\phi(M^\dagger M)^{-1}|M^\dagger\frac{\partial M(U)}{\partial U_{x,\mu}}+\frac{\partial M^\dagger(U)}{\partial U_{x,\mu}}M|(M^\dagger M)^{-1}\phi\rangle\\ &= \langle X|M^\dagger\frac{\partial M(U)}{\partial U_{x,\mu}}+\frac{\partial M^\dagger(U)}{\partial U_{x,\mu}}M|X\rangle. \qquad (5.41)\end{aligned}$$

Details on how to compute $\frac{\partial M}{U_{x,\mu}}$, $\frac{\partial M^\dagger}{U_{x,\mu}}$ are given in Appendix A. The RHMC algorithm and the R-algorithm generalize this step to allow arbitrary n_f. This will be discussed in the next two sections. We use the stabilized bi-conjugate-gradient method [95] to calculate the inverse $|X\rangle = (M^\dagger M)^{-1}|\phi\rangle$. Since $M^\dagger M$ is a very large matrix, this part is usually the most time-consuming (about 50% of the total cost). On the other hand, to compute $\frac{\partial M}{U_{x,\mu}}$, $\frac{\partial M^\dagger}{U_{x,\mu}}$ one has to identify all the paths containing $U_{x,\mu}$ and to construct the force matrix for each path. This calculation is rather trivial for the unimproved action and the computational cost is found to be $< 1\%$. For the MILC action, however, $\frac{\partial M}{U_{x,\mu}}$, $\frac{\partial M^\dagger}{U_{x,\mu}}$ have very complicated structure. A single pass of the derivative subroutine takes almost as much time as a matrix inversion.

2) **Heat bath updates**. The molecular dynamics evolution is deterministic and lacks ergodicity. To introduce randomness to the method, we interrupt the integration from time to time and choose a new set of P and ϕ with probability distributions (Gaussian) given by

$$\begin{aligned}P_{x,\mu} = \sum_a p^a_{x,\mu}t^a \quad &; \quad \mathrm{Prob}(p^a_{x,\mu}) \propto e^{-\frac{1}{2}(p^a_{x,\mu})^2}\\ |\phi\rangle = M(U)|R\rangle \quad &; \quad \mathrm{Prob}(R^a_x) \propto e^{-\frac{1}{2}R^{a*}_x R^a_x}. \qquad (5.42)\end{aligned}$$

3) **Monte Carlo accept/reject step.** The evolution equations (5.35) - (5.37) have finite step size errors hence energy is not exactly conserved. As a result there is an error in the distribution, $e^{-(S+\Delta S)}$. This systematic error can be eliminated by inserting a Monte Carlo accept/reject step at the end of the molecular dynamics integration: accept $U' \equiv U|_{t=T}$ as the new configuration with probability [93]

$$\text{Prob}(U \to U') = \min\left\{1, e^{-\delta\mathcal{H}}\right\}, \tag{5.43}$$

where $\delta\mathcal{H} = \mathcal{H}|_{t=T} - \mathcal{H}|_{t=0}$ is the change in energy. If the configuration U' is not accepted, keep the old configuration U and repeat 1) and 2). It can be shown that $\text{Prob}(U \to U)$ satisfies the so-called "detailed balance" and the distribution converges to e^{-S} as the sample size $N \to \infty$ [22, 93]. Note that the new configuration is always accepted if the energy is conserved, i.e., if there are no finite step size errors.

The major drawback of the HMC algorithm is the constraint on the number of quark flavours, $n_f = 12$ when TBC. We are now going to discuss the RHMC algorithm and the R-algorithm which are applicable to any number of flavours. However, as we will see below, the R-algorithm cannot be made exact by a Monte Carlo accept/reject step. Simulation results have to be extrapolated to $\Delta t = 0$.

The Rational Hybrid Monte Carlo (RHMC) Algorithm

The reason for fixing $n_f = 12$ in (5.41) is that $(M^\dagger M)^{-n_f/12}$ is an inverse of a matrix, $|X\rangle = (M^\dagger M)^{-1}|\phi\rangle$, which can be computed using well known numerical subroutines. On the other hand, there is no exact solution to $|X\rangle = (M^\dagger M)^{-n_f/12}|\phi\rangle$ when n_f is not a multiple of 12. The idea of the RHMC algorithm is to approximate the $n_f/12$-root by a rational expansion

$$(M^\dagger M)^{-n_f/12} \approx \alpha_0 + \sum_{l=1}^{N} \frac{\alpha_l}{M^\dagger M + \beta_l}. \tag{5.44}$$

We are therefore looking for an *optimal* rational approximation of $x^{-n_f/12}$ (and $x^{n_f/24}$, see below) in the interval $[\lambda_{\min}, \lambda_{\max}]$ where $\lambda_{\min}$ and $\lambda_{\max}$ are the smallest and largest eigenvalues of $M^\dagger M$. The lower bound is set by the quark mass $\lambda_{\min} = (2m)^2$ and one can show that $\lambda_{\max} = 32 + (2m)^2$ [82]. Optimal rational approximations can be found using the Remes algorithm [96] and numerical packages are available on the

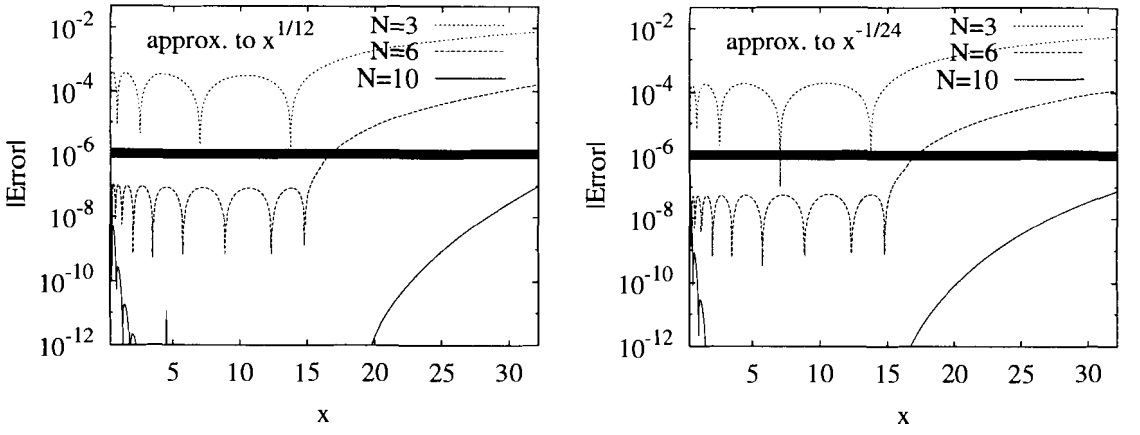

Figure 5.6: Quality of the optimal rational approximation to $x^{-1/12}$ and $x^{1/24}$. The absolute error, $|\sum_{l=1}^{N} \alpha_l/(x+\beta_l) - f(x)|$, is plotted. Solid lines represent the magnitude of statistical errors, $\mathcal{O}(10^{-6})$.

World-Wide-Web. The Netlib's Remes library is used in this project [8]. In Fig. 5.6 we plot the error of the approximation to $x^{-1/12}$ and $x^{1/24}$ over the range [0.16,32.16]. These correspond to $n_f = 1$ and $m = 0.02$ which are the actual parameters used in the next chapter. Solid lines represent the magnitude of the statistical errors, which are of $\mathcal{O}(10^{-6})$, see Section 5.5. It can be seen that rational approximations often converge quickly to the target functions. Our simulations use a 10-term expansion to make certain that approximation errors are always smaller than the statistical errors.

The rational approximation (5.44) changes the action back to the form $e^{-\phi^\dagger (M^\dagger M)^{-1}\phi}$ so that the HMC algorithm is again applicable. The fermionic force is modified to

$$\begin{aligned} \frac{\partial}{\partial U_{x,\mu}} \langle\phi|(M^\dagger M)^{-n_f/12}|\phi\rangle &\approx \sum_{l=1}^{N} \frac{\partial}{\partial U_{x,\mu}} \langle\phi| \frac{\alpha_l}{M^\dagger(U)M(U)+\beta_l} |\phi\rangle \\ &= \sum_{l=1}^{N} \alpha_l \langle X_l| M^\dagger \frac{\partial M(U)}{\partial U_{x,\mu}} + \frac{\partial M^\dagger(U)}{\partial U_{x,\mu}} M |X_l\rangle, \quad (5.45) \end{aligned}$$

where $|X_l\rangle = (M^\dagger M + \beta_l)^{-1}|\phi\rangle$. We also need to change the Gaussian update of $|\phi\rangle$

$$|\phi\rangle = (M^\dagger M)^{n_f/24}|R\rangle \approx \left(\rho_0 + \sum_{l=1}^{N} \frac{\rho_l}{M^\dagger M + \sigma_l}\right)|R\rangle, \quad (5.46)$$

[8] Web site: http://www.netlib.org.

and $|R\rangle$ is again a random Gaussian vector. Note that in the original HMC algorithm we wrote $|\phi\rangle = M|R\rangle$ for $n_f = 12$, see (5.42). The Hermitian form $M^\dagger M$ is used here, with an additional square-root, because rational approximation requires the matrix to be Hermitian (i.e., to have real eigenvalues). Hence we also need an approximation of $x^{n_f/24}$. These two steps both require the computation of N inverses of $M^\dagger M$ with mass shifts β_l or σ_l. Fortunately this can be done efficiently with a multi-mass solver [97] so that only one conjugate-gradient inversion is necessary. In the present case with $N = 10$ we found that the multi-mass solver is about 30% more expensive than a single stabilized bi-conjugate-gradient inversion. On the other hand we have to repeat the fermionic force calculation N times. This is not a major problem for the unimproved staggered quark action. For highly improved actions such as the Asqtad action this step, however, becomes extremely time consuming. This is the reason why the RHMC algorithm is used only in the unimproved case, and we found that overall RHMC is about two times slower than the conventional HMC algorithm.

The R-Algorithm

The R-algorithm [41] takes a completely different approach. Instead of writing $\left[\det(M^\dagger M)\right]^{n_f/12}$ as a path integral over a pseudo-fermion field ϕ as in (5.30), we use

$$\left[\det M^\dagger(U)M(U)\right]^{n_f/12} = \exp\left[\frac{n_f}{12}\mathrm{tr}\ln M^\dagger(U)M(U)\right]. \tag{5.47}$$

The partition function becomes

$$Z = \int DUDPe^{-\frac{1}{2}\mathrm{tr}P^2 - S_g + \frac{n_f}{12}\mathrm{tr}\ln M^\dagger(U)M(U)} = \int DUDPe^{-\mathcal{H}}. \tag{5.48}$$

Note that the ϕ field is completely absent. Phase space evolution can again be done using the discretized equations (5.35) – (5.37), but with a different fermionic force

$$\frac{n_f}{12}\frac{\partial}{\partial U_{x,\mu}}\mathrm{tr}\ln\left(M^\dagger(U)M(U)\right) = \frac{n_f}{12}\mathrm{tr}\left[\frac{1}{M^\dagger(U)M(U)}\frac{\partial}{\partial U_{x,\mu}}\left(M^\dagger(U)M(U)\right)\right]. \tag{5.49}$$

Clearly it is impractical to compute the fermionic force because we would have to calculate all elements of the inverse of $M^\dagger M$ rather than just the inverse applied to a

vector. The solution is to *estimate* $(M^\dagger M)^{-1}$ using a Gaussian noise $|R\rangle$ [98]

$$\begin{aligned}(M^\dagger M)^{-1} &\rightarrow \left(\frac{1}{M^\dagger M}M|R\rangle\right)\left(\langle R|M^\dagger\frac{1}{M^\dagger M}\right)\\ &= \frac{1}{M^\dagger M}|\phi\rangle\langle\phi|\frac{1}{M^\dagger M} = |X\rangle\langle X|. \end{aligned} \tag{5.50}$$

The fermionic force is then given by

$$\frac{n_f}{12}\mathrm{tr}\left[\frac{1}{M^\dagger(U)M(U)}\frac{\partial}{\partial U_{x,\mu}}\left(M^\dagger(U)M(U)\right)\right] \rightarrow \frac{n_f}{12}\langle X|\frac{\partial}{\partial U_{x,\mu}}(M^\dagger M)|X\rangle. \tag{5.51}$$

Note that the definitions of $|\phi\rangle$ and $|X\rangle$ are exactly the same as before, see (5.41) and (5.42), and we are back to the HMC algorithm. There are, however, two major differences. First, $|\phi\rangle$ is held fixed during the leapfrog integration in the HMC algorithm. Here, being a noisy estimator, $|\phi\rangle = M|R\rangle$ is re-evaluated every time we compute the fermionic force. The second difference which is more important is that energy is not conserved anymore. This is because we only *estimate* the fermionic force instead of calculating it. Consequently the R-algorithm cannot be made exact by a Monte Carlo accept/reject step. The acceptance rate would be extremely small. It can be shown that measurements have leading errors of $\mathcal{O}\Delta t^2$ [41], therefore results have to be extrapolated to $\Delta t = 0$.

5.4 Other Systematic Errors

There are two other systematic errors: autocorrelation and inaccuracy in the evaluation of $(M^\dagger M)^{-1}$. Statistical errors and fitting errors will also be discussed. In this project fitting is done with the constraint curve fitting program [99].

Autocorrelation

The sequentially generated configurations are not statistically independent to each other. Each configuration remembers the configurations that generate it. As a result successive measurements are correlated, and statistical errors would be underestimated. Correlation reduces to an acceptable level only after a sufficiently large number of updates. Correlation can be measured by the autocorrelation function (for

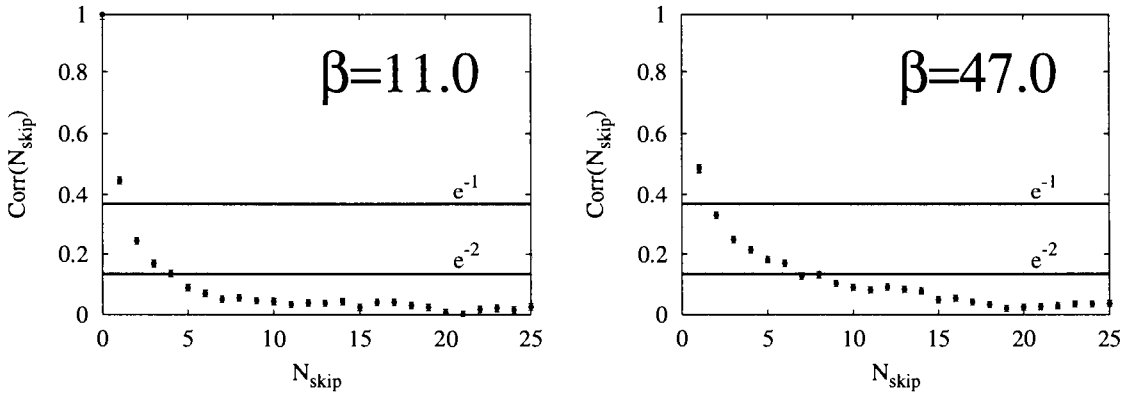

Figure 5.7: Plaquette autocorrelation functions at $\beta = 11.0$ and $\beta = 47.0$ in the MILC simulations.

observable $\mathcal{O}$ with average $\bar{\mathcal{O}}$) [100]

$$\mathrm{Corr}(N_{skip}) = \frac{\langle (\mathcal{O}_i - \bar{\mathcal{O}})(\mathcal{O}_{i+N_{skip}} - \bar{\mathcal{O}}) \rangle}{\langle (\mathcal{O}_i - \bar{\mathcal{O}})^2 \rangle} \tag{5.52}$$

where N_{skip} is the number of configurations skipped between measurements. In general, $\mathrm{Corr}(N_{skip})$ decays exponentially

$$\mathrm{Corr}(N_{skip}) \sim e^{-N_{skip}/N_c}. \tag{5.53}$$

The decay constant N_c is called the autocorrelation time, which is the time for the correlation function to decay a factor of e. It is evidence that different observables have different autocorrelation times. In particular the correlation is expected to be longer for a larger Wilson loop since more links have to lose their memory of the previous configurations.

We only tested the correlation for the plaquette where the autocorrelation functions at $\beta = 11.0$ and $\beta = 47.0$ (the smallest and largest β) in the MILC simulations are given in Fig. 5.7. Note that the autocorrelation time is longer for larger β. This is the problem of critical slow down: it becomes more difficult to get statistically independent configurations when one moves closer to the continuum limit [9]. In this project 20 configurations are skipped between measurements, as Fig. 5.7 indicates that this is enough for the autocorrelation function to reduce to zero within statistical errors.

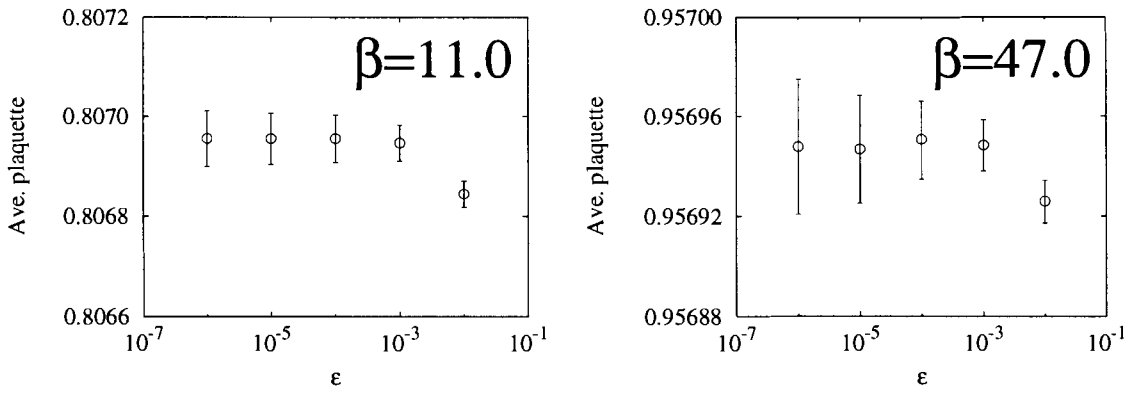

Figure 5.8: Dependence of the average plaquette on ϵ.

Inaccuracy in the Evaluation of $(M^\dagger M)^{-1}$

Both the RHMC algorithm and the R-algorithm require many matrix inversions in the form of $|X\rangle = (M^\dagger M)^{-1}|\phi\rangle$. The stabilized bi-conjugate-gradient method [95] is used in this project to compute the inverses. It is an iterative method and the convergence criterion is

$$||M^\dagger M|X\rangle - |\phi\rangle|| < \epsilon. \tag{5.54}$$

We have studied the dependence of measured quantities on ϵ. Figure 5.8 plots the average plaquettes obtained with different values of ϵ at $\beta = 11.0$ and $\beta = 47.0$ in the unimproved case. One can see that all results agree within statistical errors ($\mathcal{O}(10^{-5})$) for $\epsilon \leq 10^{-3}$. In this project we choose a value which is comparable to the magnitude of the statistical errors, $\epsilon = 1 \times 10^{-5}$.

Truncation Errors and Fitting Errors

In principle perturbative expansions have infinitely many parameters ((4.1) repeated here)

$$-\frac{\ln W_{R,T}}{2(R+T)} = c_1\alpha_V(q^*_{R,T}) + c_2\alpha_V^2(q^*_{R,T}) + c_3\alpha_V^3(q^*_{R,T}) + \ldots \tag{5.55}$$

On the other hand, simulations were done at 7 and 9 values of couplings for the unimproved action and the MILC action respectively (see next chapter) hence there is only a small number of data points. Clearly we cannot fit an infinite number of parameters using only 7 or 9 data points. The perturbative expansion therefore has to

be truncated. An important aspect of the fitting procedure is how to account for the truncation errors in the fitting function. Choosing an expansion with too few terms results in a poor fit of the data, while including too many higher-order terms leads to poor determination of the lower-order coefficients which should, if the perturbative series is well behaved, make dominant contributions to the data. This problem can be circumvented by using constrained curve fitting [99].

Traditional least square fits minimize

$$\chi^2 \equiv \sum_{\text{data } i} (\text{err}_i)^2 = \sum_{\text{data } i} \frac{(Y_i - \sum_n c_n \alpha_{Vi}^n)^2}{\sigma_{Y_i}^2} \tag{5.56}$$

by varying the perturbative coefficients $c_1, \ldots, c_N$, where N is the order at which we have made the truncation, and $(\alpha_{Vi}, Y_i \pm \sigma_{Y_i})$, $i = 1, \ldots, 7$ or 9, are the data points. In constrained curve fitting χ^2 is augmented by

$$\chi^2 \to \chi^2_{\text{arg}} \equiv \chi^2 + \sum_{n=1}^{n=N} \frac{(c_n - \bar{c}_n)^2}{\bar{\sigma}_n^2}. \tag{5.57}$$

The extra terms in χ^2_{arg} favour c_n's in the interval $\bar{c}_n \pm \bar{\sigma}_n$, which are inputs to the fitting subroutine and are collectively known as "priors". The values of $\bar{c}_n$ must be chosen based on theoretical expectation, and the optimal widths $\bar{\sigma}_n$ can be determined from the data by maximizing the probability of obtaining the measurements $(\alpha_{Vi}, Y_i \pm \sigma_{Y_i})$ given the prior information. We will not discuss the theoretical aspects of this method [9] but instead simply describe the fitting procedures. We set $\bar{c}_i = 0$ and all $\bar{\sigma}_n$ equal, and determined an optimal $\bar{\sigma}_n$ to be $\sim$1.0–1.5. This reflects the fact that c_n's to be of $\mathcal{O}(1)$ if perturbation theory is reliable. In addition, the priors for c_1, c_2 can be fixed to the existing analytic results to obtain a better constraint on higher-order coefficients. We observe that the errors on c_3 generally reduce by a factor of $\sim$4–5 compared to the case when there is no input from analytic calculation.

Convergence plays a crucial role in constrained curve fitting. For those coefficients whose values and errors are insensitive to $\bar{\sigma}_n$, and to the number of terms in the expansion (N), we can say that they are largely determined by the Monte Carlo data. On the other hand, if the coefficients are controlled mostly by the priors, it means that the data cannot resolve the coefficients. Therefore we do not have to worry at what

[9] See Ref. [99] for an overview of Bayesian statistics and constrained curve fitting.

order the truncation should be made, but instead the data should tell us how much it can determine. In this project we observe that c_1, c_2 and c_3 are very insensitive to N, while the fitting program simply reproduces the priors for higher-order coefficients c_4, c_5, ... This means that our data can only resolve the first three order coefficients. If the statistics of the data is increased, more coefficients can be determined.

Explicit examples on how the fitting is done will be given in next chapter. Constrained curve fitting is also used for Δt extrapolation for the R-algorithm. The fitting program is provided by Lepage [99]. Constrained curve fitting has now became a lattice industry standard.

Statistical Errors and Summary

We have presented an extensive study of systematic errors in the last few sections. The reason for such a detailed analysis is that Wilson loops must be determined with extremely high statistics so that the third order coefficients can be extracted with a reasonable error. Statistical errors are estimated by the Jackknife method [101], a variant of the bootstrap method,

$$\delta\langle\mathcal{O}\rangle = \sqrt{\left(1-\frac{1}{N}\right)\sum_{i}^{N}(\langle\mathcal{O}\rangle - \langle\mathcal{O}\rangle_i^*)^2}, \tag{5.58}$$

where N is the number of configurations and $\langle\mathcal{O}\rangle_i^*$ is the average excluding $\mathcal{O}_i$

$$\langle\mathcal{O}\rangle_i^* \equiv \frac{1}{N-1}\sum_{j\neq i}^{N}\mathcal{O}_j. \tag{5.59}$$

As we will see in the next chapter, statistical errors are of $\mathcal{O}(10^{-6}-10^{-5})$. Approximately 2 months of computational time on 25 Pentium 4 processors is required to reach this level of accuracy for the unimproved action (with 7 values of β), and it took a total of 5 months computation, on the same number of processors, to finish the MILC simulations (with 9 values of β). Note that 4 times more configurations have to be generated to reduce the errors by half. Table 5.1 compares the size of the statistical errors with other systematic effects.

Source of errors	Magnitude	Solution/Remark
Zero modes	unknown	apparently eliminated by using TBC
Tunneling	unknown	strongly suppressed by using TBC
Δt errors in simulation equations	Δt^2	RHMC: removed by Monte Carlo accept/reject steps R-algorithm: extrapolation to $\Delta t = 0$
Rational approx. of $[M^\dagger M]^{n_f/12}$	$< 10^{-6}$ in $[\lambda_{\min}, \lambda_{\max}]$	10th-order expansions which have errors $< 10^{-6}$ in $[\lambda_{\min}, \lambda_{\max}]$ are used
Autocorrelation	unknown	20 configurations are skipped between measurements
Inaccuracy in evaluation of $(M^\dagger M)^{-1}$	convergence criterion $\epsilon = 10^{-5}$	there is no significant difference on measured quantities for ϵ as large as 10^{-3}
Fitting and truncation errors	data are sensitive to α^3	fitting is done by constrained curve fitting
Statistical errors	10^{-5}–10^{-6}	4 times more configurations have to be generated to reduce error by half

Table 5.1: Summary of the various systematic effects.

Chapter 6

Results

Simulation results are reported in this chapter. Simulations were done at 7 and 9 values of couplings for the unimproved action and the MILC action respectively. The logarithms of the Wilson loops were measured, and results are fitted with

$$-\frac{\ln W_{R,T}}{2(R+T)} = \sum_{n=1}^{n=N} c_n \alpha_V^n(q^*_{R,T}) \tag{6.1}$$

to extract the perturbative coefficients c_n. Our data can only resolve the first three order coefficients, which agree very well with those obtained analytically in Ref. [33]. **This provides an important cross-check of the analytic results**, which are used in a recent determination of the strong coupling $\alpha_{\overline{MS}}(M_Z)$ by the HPQCD collaboration [13].

This chapter is organized as follows. We will first describe how the analysis is done (e.g., how to determine the renormalized coupling $\alpha_V(q^*_{R,T})$) in the next section. The comparison between the results of Ref. [33] and our Monte Carlo results is complicated by the fact that the analytic calculations were done on 8^4 lattices with twisted boundary conditions for c_1, but at infinite volume for c_2 and c_3. A discussion on this issue will be given. Results for the unimproved action are presented in Section 6.2 and for the MILC action in Section 6.3. The R-algorithm is used in the latter case so Wilson loops must first be extrapolated to $\Delta t = 0$. A conclusion will be given in Section 6.4.

6.1 Analysis

Determination of $\alpha_V(q^*_{R,T})$

Before fitting, we must first of all determine the renormalized coupling $\alpha_V(q^*_{R,T})$ for each β. The connection between the bare coupling α_0 and $\alpha_V(q^*_{R,T})$ is given by (4.10). Since it is the same 2-loop calculation of the Wilson loops of Ref. [33], we instead use the expansion of the plaquette to serve as a simpler definition of the renormalized coupling. For the unimproved action (see below for a discussion on the volume and mass parameter used in the analytic calculations), it is

$$-\frac{\ln W_{1,1}}{4} \approx \begin{cases} 1.04720(0)\alpha_V - 1.3165(1)\alpha_V^2 - 1.30(3)\alpha_V^3, & n_f = 1 \\ 1.04720(0)\alpha_V - 1.4561(2)\alpha_V^2 - 0.34(8)\alpha_V^3, & n_f = 3, \end{cases} \tag{6.2}$$

and for the MILC action

$$-\frac{\ln W_{1,1}}{4} \approx 0.76710(0)\alpha_V - 0.6684(2)\alpha_V^2 + 0.02(4)\alpha_V^3, \quad n_f = 1. \tag{6.3}$$

The renormalized coupling $\alpha_V(q^*_{1,1})$ can be solved by inserting the measured plaquette value $\langle W_{1,1}\rangle_{\rm MC}$ into the above equations. Note that we are using the expansion of $-\ln W_{1,1}$ in Ref. [33] to define $\alpha_V(q^*_{1,1})$, but at the same time checking the results for large Wilson loops in the same calculation. Our analysis therefore is not completely independent of Ref. [33]. Nonetheless it serves as an important consistency check of the perturbative calculations.

After solving $\alpha_V(q^*_{1,1})$, the intrinsic scale Λ in the running coupling formula (4.16) can be determined, and one can then run the scale to $q^*_{R,T}$ to obtain $\alpha_V(q^*_{R,T})$. The values of $q^*_{R,T}$ are computed in Refs. [65, 33] and are given in Table 6.1.

Uncertainty in $\alpha_V(q^*_{1,1})$

A note should be added here. The values of $\alpha_V(q^*_{1,1})$ determined from (6.2) and (6.3) are subject to systematic errors, due to the statistical errors in $\langle W_{1,1}\rangle_{\rm MC}$ and the perturbative coefficients [1]. The errors then propagate to other values of $\alpha_V(q^*_{R,T})$. This induces an additional error, beyond its own statistical error, on $\langle \ln W_{R,T}\rangle_{\rm MC}$.

[1] Although Ref. [33] is an analytic calculation, not a simulation, the coefficients have statistical errors because loop integrations at higher-order were computed using a Monte Carlo integrator, e.g., VEGAS [102].

Loop	$q^*_{R,T}$ (unimproved)	$q^*_{R,T}$ (MILC)
1×1	3.40	3.33
1×2	3.07	3.00
1×3	3.01	2.93
2×2	2.65	2.58
2×3	2.56	2.48
3×3	2.46	2.37

Table 6.1: Relevant momentum scale for various small Wilson loops [65, 33].

To estimate this induced error, approximate $-\ln W_{R,T}/2(R+T)$ by its first order expansion

$$-\frac{\ln W_{R,T}}{2(R+T)} \approx c_{1\,R,T}\alpha_V(q^*_{R,T}). \tag{6.4}$$

Define $\Delta[X]$ to be the uncertainty in X, we have

$$\Delta[\alpha_V(q^*_{1,1})] \approx \frac{-\Delta[\ln W_{1,1}]_{\rm MC}}{4c_{11,1}}. \tag{6.5}$$

This equation reflects that statistical error of $\langle W_{1,1}\rangle_{\rm MC}$ dominates at high β. With $\alpha_V(q^*_{1,1}) \approx \alpha_V(q^*_{R,T})$ and $\Delta[\alpha_V(q^*_{1,1})] \approx \Delta[\alpha_V(q^*_{R,T})]$, the induced error on $\ln W_{R,T}$ is

$$\begin{aligned} -\Delta[\ln W_{R,T}]_{\rm induced} &\approx 2(R+T)c_{1\,R,T}\Delta[\alpha_V(q^*_{R,T})] \\ &\approx -2(R+T)c_{1\,R,T}\frac{\Delta[\ln W_{1,1}]_{\rm MC}}{4c_{11,1}} \\ &\approx -\frac{\ln W_{R,T}}{\ln W_{1,1}}\Delta[\ln W_{1,1}]_{\rm MC}. \end{aligned} \tag{6.6}$$

Table 6.2 shows $\Delta[\ln W_{R,T}]_{\rm MC}$ and $\Delta[\ln W_{R,T}]_{\rm induced}$ for one of the simulations. It can be observed that $\Delta[\ln W_{R,T}]_{\rm induced}$ grows, but becomes less significant compared to the Monte Carlo error $\Delta[\ln W_{R,T}]_{\rm MC}$ when the loop size increases. The sums of the two errors are used in the fitting.

A Discussion on the Analytic Calculation

The analytic calculations of Ref. [33] were done at infinite volume (to avoid zero momentum modes) with massless quarks (i.e., $m = 0$). On the other hand we work on 8^4 lattices with twisted boundary conditions and set $m = 0.2$ for the unimproved

Loop	$-\langle \ln W_{R,T} \rangle$	$\Delta[\ln W_{R,T}]_{\rm MC}$ ($\times 10^{-5}$)	$\Delta[\ln W_{R,T}]_{\rm induced}$ ($\times 10^{-5}$)
1×1	0.13976	2.2	2.2
1×2	0.24382	4.6	3.8
1×3	0.34158	7.9	5.3
2×2	0.39270	8.8	6.1
2×3	0.52235	13.7	8.1
3×3	0.66857	20.2	10.4

Table 6.2: Comparison of $\Delta[\ln W_{R,T}]_{\rm MC}$ and $\Delta[\ln W_{R,T}]_{\rm induced}$. Results are shown for the unimproved action at $\beta = 16.0$ and $n_f = 1$.

action and $m = 0.1$ for the MILC action [2]. Finite volume effects are proportional to $1/V \sim \mathcal{O}(10^{-4})$ [91] while c_2 suffers from $\mathcal{O}(m^2) \sim \mathcal{O}(0.01)$ corrections[3] [33]. Therefore for proper comparison with the Monte Carlo results in this thesis, my supervisor (one of the authors of Ref. [33]) repeated the perturbative calculations on 8^4 lattices with twisted boundary conditions for c_1, and with the same quark masses as in the simulations for c_2 and c_3. It is important to correct the finite volume effects for c_1, since we will fix c_1 and c_2 to their analytic values in the fits to obtain a better determination of the third order coefficients. Given that our α's are of $\mathcal{O}(0.01)$, an $1/V$ error in c_1 induces an error of $\mathcal{O}(1)$ in c_3. Similarly analytic perturbation theory for c_2 must be done at the same masses as used in the simulations because m^2 corrections in c_2 also lead to an error of $\mathcal{O}(1)$ in c_3.

6.2 The Unimproved Action

Simulation Parameters

Perturbative Wilson loops for the unimproved action (the Wilson plaquette action and the unimproved staggered quark action) are studied in this section. Simulation parameters are summarized in Table 6.3. Simulations were done at 7 values of couplings ranging from $\beta = 11.0$ to $\beta = 47.0$. These values are much larger than those

[2]Remember that the RHMC algorithm is used in the unimproved case, which requires the approximations of $x^{-n_f/12}$ and $x^{n_f/24}$ in $[(2m)^2, 32 + (2m)^2]$. Generally the rational approximation is less efficient if the lower limit is too small. This is the reason why a larger quark mass is used for the unimproved action.

[3]The first order coefficients are independent of n_f and the quark masses.

Number of flavours: $n_f = 1$						
β	$\alpha_0 = \frac{6}{4\pi\beta}$	$\langle W_{1,1} \rangle$	Measurements	Acceptance rate	$\alpha_V(q^*_{1,1})$	Λ
11.0	0.04341	0.805569(41)	849	92%	0.05574	2×10^{-5}
13.5	0.03537	0.843964(34)	902	90%	0.04292	9×10^{-6}
16.0	0.02984	0.869561(26)	992	87%	0.03496	4×10^{-7}
19.0	0.02513	0.890999(21)	981	81%	0.02860	9×10^{-9}
24.0	0.01989	0.914413(16)	1066	69%	0.02198	2×10^{-11}
32.0	0.01492	0.936259(11)	1180	58%	0.01605	7×10^{-16}
47.0	0.01016	0.956886(7)	1261	53%	0.01067	4×10^{-24}
Number of flavours: $n_f = 3$						
β	$\alpha_0 = \frac{6}{4\pi\beta}$	$\langle W_{1,1} \rangle$	Measurements	Acceptance rate	$\alpha_V(q^*_{1,1})$	Λ
11.0	0.04341	0.807064(36)	821	89%	0.05551	4×10^{-6}
13.5	0.03537	0.844847(26)	641	86%	0.04283	1×10^{-6}
16.0	0.02984	0.870205(21)	740	84%	0.03490	3×10^{-8}
19.0	0.02513	0.891387(18)	738	77%	0.02859	4×10^{-10}
24.0	0.01989	0.914647(13)	791	66%	0.02197	3×10^{-13}
32.0	0.01492	0.936402(10)	840	56%	0.01605	2×10^{-18}
47.0	0.01016	0.956950(6)	902	52%	0.01066	9×10^{-28}

Table 6.3: Simulation parameters for the **unimproved action**. Simulations were done on 8^4 lattices with quark mass $m = 0.2$. The RHMC algorithm is used with step size $\Delta t = 0.01$ and $n_{md} = 50$.

used in conventional simulations ($\beta \approx 6.0$) so that the coupling constants $\alpha_0 = \frac{6}{4\pi\beta}$ are purely perturbative, of $\mathcal{O}(0.1\text{–}0.01)$. Notice the differences between α_0 and the renormalized coupling $\alpha_V(q^*_{1,1})$. For comparison two sets of simulations, with $n_f = 1$ and $n_f = 3$, were done. The volume of the lattice is 8^4. Twisted boundary conditions are applied to all three spatial directions while periodic boundary conditions are used in the temporal direction.

Configurations were generated using the RHMC algorithm with $\Delta t = 0.01$ and $n_{md} = 50$. The acceptance rate is about 90% for $\beta = 11.0$ and reduces to 50% for $\beta = 47.0$ Since the algorithm is exact, no zero step size extrapolation is required. Simulations were started from a cold start (all links are set to the identity) and the

Dependence on N ($\bar{\sigma}_n = 1.5$)				Dependence on $\bar{\sigma}_n$ ($N = 6$)			
c_n	$N = 4$	$N = 5$	$N = 6$	c_n	$\bar{\sigma}_n = 1.0$	$\bar{\sigma}_n = 1.5$	$\bar{\sigma}_n = 5.0$
c_1	1.4334(6)	1.4334(6)	1.4334(6)	c_1	1.4335(5)	1.4334(6)	1.4333(6)
c_2	-1.37(4)	-1.37(4)	-1.37(4)	c_2	-1.38(4)	-1.37(4)	-1.36(4)
c_3	-0.91(56)	-0.91(56)	-0.91(56)	c_3	-0.79(51)	-0.91(56)	-0.98(77)
c_4	-0.1(15)	-0.1(15)	-0.1(15)	c_4	-0.1(10)	0.0(15)	-0.5(50)
c_5		0.0(15)	0.0(15)	c_5	0.0(10)	0.0(15)	0.0(50)
c_6			0.0(15)	c_6	0.0(10)	0.0(15)	0.0(50)
χ^2	0.56	0.56	0.56	χ^2	0.93	0.56	0.28

Table 6.4: Dependence on N and the prior width $\bar{\sigma}_n$ for constrained curve fitting. The priors are always set equal to $\bar{c}_n = 0$ and the same width is used for all n. Results are shown for the 2×2 loop, $n_f = 1$. The quality of the fits, χ^2 per degree of freedom, is also shown.

first 1000 configurations are discarded for thermalization. To minimize autocorrelation 40 configurations are skipped between successive measurements [4]. About 1000 measurements are taken for each simulation. It required 2 months to complete the simulations on 25 Pentium 4 processors.

Results

The renormalized coupling $\alpha_V(q^*_{R,T})$ for each Wilson loop can be solved using the procedures described in the last section. Results are analyzed using the constrained curve fitting program with

$$-\frac{\ln W_{R,T}}{2(R+T)\alpha_V(q^*_{R,T})} = \sum_{n=1}^{n=N} c_n \alpha_V^{n-1}(q^*_{R,T}). \tag{6.7}$$

To see how sensitive our data are to the higher-order terms in the expansion, we vary N (from $N = 4$ to $N = 6$) and the prior width $\bar{\sigma}_n$ ($\bar{\sigma}_n = 1.0$, 1.5, 5.0). The priors are always set equal to $\bar{c}_n = 0$ and the same width is used for all n. Results are shown in Table 6.4 for the 2×2 loop and $n_f = 1$. Perturbative calculations of Ref. [33] give $c_1 = 1.4339(0)$, $c_2 = -1.400(2)$, $c_3 = -0.52(7)$. One can see that c_1, c_2 and c_3 are

[4]Since the Monte Carlo accept/reject step keeps the old configuration about half of the time for the largest β, we expect the correlation time to be longer in this case. Therefore we skip 40 instead of 20 configurations between measurements.

Number of flavours: $n_f = 1$						
	Perturbation Theory			Monte Carlo Method		
Loop	c_1	c_2	c_3	c_1	c_2	c_3
1×2	1.2039(0)	-1.335(0)	-1.10(3)	1.2038(4)	-1.327(29)	-1.26(46)
1×3	1.2589(0)	-1.277(1)	-0.95(6)	1.2586(5)	-1.253(36)	-1.43(56)
2×2	1.4339(0)	-1.400(2)	-0.52(8)	1.4334(6)	-1.368(39)	-0.95(59)
2×3	1.5172(0)	-1.351(3)	-0.26(12)	1.5163(7)	-1.281(47)	-1.11(71)
3×3	1.6090(0)	-1.298(6)	0.67(25)	1.6080(8)	-1.230(56)	-0.45(82)
Number of flavours: $n_f = 3$						
	Perturbation Theory			Monte Carlo Method		
Loop	c_1	c_2	c_3	c_1	c_2	c_3
1×2	1.2039(0)	-1.485(0)	-0.11(9)	1.2039(4)	-1.480(28)	-0.28(45)
1×3	1.2589(0)	-1.437(1)	0.02(11)	1.2590(5)	-1.444(34)	-0.06(54)
2×2	1.4339(0)	-1.551(2)	0.51(13)	1.4337(5)	-1.529(38)	0.02(60)
2×3	1.5172(0)	-1.513(4)	0.73(16)	1.5169(6)	-1.476(46)	0.20(71)
3×3	1.6090(0)	-1.463(11)	1.62(30)	1.6088(8)	-1.431(53)	0.65(81)

Table 6.5: Perturbative coefficients of various small Wilson loops for the unimproved action.

very insensitive to N and $\bar{\sigma}_n$, while the fitting subroutine simply reproduces the priors for higher-order coefficients. This indicates that our data can resolve the first three coefficients only. Table 6.4 also shows the important of choosing an appropriate prior width $\bar{\sigma}_n$. Over constraining the coefficients results in a poor fit of the data (bad χ^2). On the other hand a large value of $\bar{\sigma}_n$ gives coefficients with large errors, e.g., changing from $\bar{\sigma}_n = 1.5$ to $\bar{\sigma}_n = 5.0$ increases the error in c_2 from 0.56 to 0.77, but its value is essential unchanged. As discussed in Section 5.4 the optimal width can be determined by maximizing the probability of obtaining the data given the prior information. We find that the value $\bar{\sigma}_n = 1.5$ is the most favourable in this case. In summary we use $N = 6$ and priors $\bar{c}_n \pm \bar{\sigma}_n = 0 \pm 1.5$ for the fitting.

Results are reported in Table 6.5. Agreement with the analytic calculations is impressive, although the statistical errors are much larger for the Monte Carlo results. Note that the first order coefficients are independent of the number of flavours. On the other hand, results for c_2 and c_3 clearly show that the effects of dynamical fermions

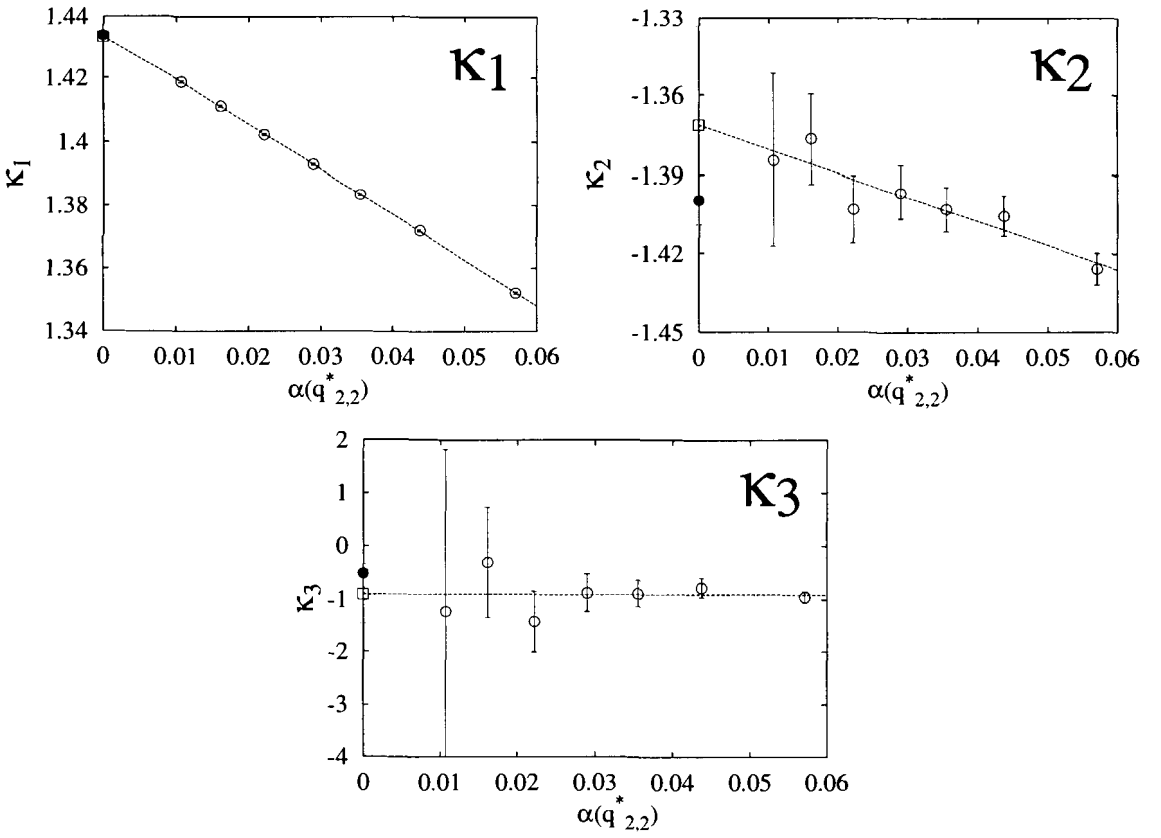

Figure 6.1: Plots of κ_1, κ_2, κ_3 [2×2 loop, $n_f = 1$, the unimproved action]. The symbols • and ⊡ label the Monte Carlo results c_n^{MC} and the analytic results respectively.

are correctly reproduced in the simulations. We again want to emphasize that this is the first time the Monte Carlo method is applied to lattice fermion actions. All previous studies were done for pure gauge theories where contributions from dynamical fermions had been neglected.

To visualize the quality of the fits, we plot the following quantities

$$\begin{aligned}
\kappa_1 &\equiv \frac{1}{\alpha_V(q^*_{R,T})}\left[\frac{-\ln W_{R,T}}{2(R+T)}\right] \approx c_1^{MC} + c_2^{MC}\alpha_V + c_3^{MC}\alpha_V^2 + c_4^{MC}\alpha_V^3 \\
\kappa_2 &\equiv \frac{1}{\alpha_V^2(q^*_{R,T})}\left[\frac{-\ln W_{R,T}}{2(R+T)} - c_1^{MC}\alpha_V\right] \approx c_2^{MC} + c_3^{MC}\alpha_V + c_4^{MC}\alpha_V^2 \\
\kappa_3 &\equiv \frac{1}{\alpha_V^3(q^*_{R,T})}\left[\frac{-\ln W_{R,T}}{2(R+T)} - c_1^{MC}\alpha_V - c_2^{MC}\alpha_V^2\right] \approx c_3^{MC} + c_4^{MC}\alpha_V
\end{aligned} \tag{6.8}$$

for the 2×2 loop ($n_f = 1$) in Fig. 6.1. The open squares (□) are the Monte Carlo results c_n^{MC} in Table 6.5 and the filled circles (•) are the perturbative results of

Number of flavours: $n_f = 1$				
	Perturbation Theory		Monte Carlo Method	
Loop	c_2	c_3	c_2	c_3
1×2	-1.335(0)	-1.10(3)	-1.332(9)	-1.19(22)
1×3	-1.277(1)	-0.95(6)	-1.270(11)	-1.20(27)
2×2	-1.400(2)	-0.52(8)	-1.403(12)	-0.48(29)
2×3	-1.351(3)	-0.26(12)	-1.342(14)	-0.28(34)
3×3	-1.298(6)	0.67(25)	-1.292(17)	0.38(41)
Number of flavours: $n_f = 3$				
	Perturbation Theory		**Monte Carlo Method**	
Loop	c_2	c_3	c_2	c_3
1×2	-1.485(0)	-0.11(9)	-1.480(10)	-0.28(25)
1×3	-1.437(1)	0.02(11)	-1.434(12)	-0.19(30)
2×2	-1.551(2)	0.51(13)	-1.541(13)	0.20(33)
2×3	-1.513(4)	0.73(16)	-1.499(16)	0.52(39)
3×3	-1.463(11)	1.62(30)	-1.442(20)	0.80(46)

Table 6.6: Second and third order coefficients with c_1 fixed to the analytic results.

Ref. [33]. Note again how well the analytic results are reproduced by the Monte Carlo data. The 4th-order term is included in the plots also, and the almost zero slope of κ_3 indicates that c_4^{MC} is small (in this case $c_4^{MC} = -0.1 \pm 1.5$). In fact, we found that all the 4th-order coefficients are equal to zero within errors.

To improve the accuracy of c_2 and c_3, we set the priors of the first order coefficients to the analytic results. Again the expansion is truncated at α_V^6 and $\bar{c}_n \pm \bar{\sigma}_n = 0 \pm 1.5$ are used for the undetermined coefficients. Results are reported in Table 6.6. One can see that the errors in c_2 and c_3 reduce by a factor of 3 and 2 respectively, and the agreement with perturbation theory becomes even more clear.

The uncertainty in the third order coefficients can be further reduced by setting the priors of both c_1 and c_2 to their analytic values. Results are shown in Table 6.7. In comparison to the original fits in Table 6.5, it can be observed that the errors decrease substantially, by almost a factor of 5. Some of the Monte Carlo results even have a smaller error than those obtained analytically. Results here clearly show that perturbation theory and Monte Carlo simulations agree through third order.

	$n_f = 1$		$n_f = 3$	
Loop	c_3 (PT)	c_3 (MC)	c_3 (PT)	c_3 (MC)
1×2	-1.10(3)	-1.13(9)	-0.11(9)	-0.17(10)
1×3	-0.95(6)	-1.02(11)	0.02(11)	-0.12(11)
2×2	-0.52(8)	-0.55(12)	0.51(13)	0.42(13)
2×3	-0.26(12)	-0.08(14)	0.73(16)	0.81(16)
3×3	0.67(25)	0.49(19)	1.62(30)	1.16(27)

Table 6.7: Third order coefficients with both c_1 and c_2 fixed to the analytic results.

6.3 The MILC Action

We have extended the Monte Carlo method to determine the perturbative expansions of the Wilson loops for the MILC action. This is the action used in today's state-of-the-art numerical simulations of QCD [10]. Our results provide an important cross-check of the perturbation theory input to a recent determination of the strong coupling $\alpha_{\overline{MS}}(M_Z)$ by the HPQCD collaboration [13].

Simulation Parameters

Simulation parameters are summarized in Table 6.8. Simulations were done at 9 values of β. Again the corresponding bare couplings $\alpha_0 = -4 \ln u_0 / 3.0684$ (see (2.41)) are of $\mathcal{O}(0.1\text{–}0.01)$ so that we are well into the perturbative regime. Note that the couplings experience a smaller renormalization compared to the unimproved case. This is expected since the MILC action is highly improved and has smaller discretization errors. The volume of the lattice is $V = 8^4$, and twisted boundary conditions are adopted in all spatial directions while periodic boundary conditions are used in the temporal direction. Simulations were done with $n_f = 1$ and $m = 0.1$. We want to reemphasize that the perturbative calculations of Ref. [33] used the same set of parameters, with the only exception that c_2 and c_3 were computed at infinite lattice volume.

Configurations were generated using the R-algorithm so that extrapolation to $\Delta t = 0$ is required. Simulations were done at 4 values of step sizes, $\Delta t = 0.005$, 0.01, 0.02, 0.03 with $n_{md} = 100$, 50, 25, 15. The results are fitted to $\sum_{n=0}^{n=N} a_n (\Delta t)^n$. We use $N = 6$ and priors $\bar{a}_n \pm \bar{\sigma}_n \approx 0 \pm 5$ except for a_1. For a_1 we set $\bar{\sigma}_1 = 0$ since the

β	Input u_0 [$\Delta t = .005$]	Measured u_0 [$\Delta t = .005$]	α_0 [$\Delta t = .005$]	$\alpha_V(q^*_{1,1})$ [$\Delta t = .005$]	Λ	Measurements $\Delta t = .005, .01, .02, .03$
9.5	0.91690	0.916922(98)	0.113	0.127	6×10^{-2}	461,457,836,1335
11.0	0.93166	0.931687(73)	0.092	0.101	2×10^{-2}	281,633,1090,1038
13.5	0.94704	0.946986(55)	0.071	0.076	3×10^{-3}	290,635,1122,1078
16.0	0.95661	0.956614(53)	0.058	0.061	5×10^{-4}	296,634,1145,1100
19.0	0.96433	0.964311(38)	0.047	0.050	6×10^{-5}	298,643,1123,1172
24.0	0.97243	0.972453(29)	0.036	0.038	1×10^{-6}	308,645,1191,1113
32.0	0.97978	0.979785(23)	0.027	0.027	3×10^{-9}	315,652,1205,1204
47.0	0.98652	0.986526(15)	0.018	0.018	4×10^{-14}	215,709,1227,963
80.0	0.99220	0.992208(13)	0.010	0.010	6×10^{-25}	472,489,974,1527

Table 6.8: Simulation parameters for the **MILC action**. Only the parameters for $\Delta t = 0.005$ are shown. The number of flavours is $n_f = 1$ with $m = 0.1$.

leading errors of the R-algorithm are of $\mathcal{O}(\Delta t^2)$. Some examples of the extrapolation are given in Table 6.9 and Fig. 6.2.

The thermalization process is much more complicated for the MILC action because the tadpole factor (the mean link) $u_0 \equiv \langle W_{1,1} \rangle^{1/4}$ has to be determined self-consistently. It is set at $u_0 = 1$ at the beginning of the simulation. After 500 trajectories u_0 is re-calculated from the 500 configurations just generated. This process is repeated for 10 times. At the end of the thermalization the final running average of u_0 is saved and used for the entire simulation. This value is verified for consistency with the final value of u_0 determined from the entire simulation (see Table 6.8). To minimize autocorrelation 20 configurations are skipped between measurements. Again about 1000 measurements are obtained in each case. Simulations were done on 25 Pentium 4 for a total of 5 months, which required 250GB of hard-drive storage space.

Results

The procedures to extract the perturbative coefficients are the same as those used in the last section. The renormalized coupling $\alpha_V(q^*_{1,1})$ can be determined from (6.3) and the couplings at other q^*'s can be computed using the running coupling formula (4.16). Results are fitted to

$$-\frac{\ln W_{R,T}}{2(R+T)\alpha_V(q^*_{R,T})} = \sum_{n=1}^{n=N} c_n \alpha_V^{n-1}(q^*_{R,T}). \tag{6.9}$$

a_n	$-\ln W_{1,1}$ ($\beta = 11$)	$-\ln W_{2,2}$ ($\beta = 16$)	$-\ln W_{2,2}$ ($\beta = 32$)	$-\ln W_{3,3}$ ($\beta = 47$)
a_0	0.28320(4)	0.55886(11)	0.25044(5)	0.28700(8)
a_1	0(0)	0(0)	0(0)	0(0)
a_2	-1.48(17)	-3.19(37)	-3.01(29)	-4.53(33)
a_3	2.0(48)	3.8(45)	0.4(44)	4.0(47)
a_4	0.1(50)	0.2(50)	0.0(50)	0.3(50)
a_5	0.0(50)	0.0(50)	0.0(50)	0.0(50)
a_6	0.0(50)	0.0(50)	0.0(50)	0.0(50)
χ^2	0.56	1.3	0.43	0.68

Table 6.9: Zero step size extrapolation for the R-algorithm. The priors $\bar{a}_n \pm \bar{\sigma}_n = 0 \pm 5$ are used except for a_1, for which $\bar{\sigma}_1 = 0$.

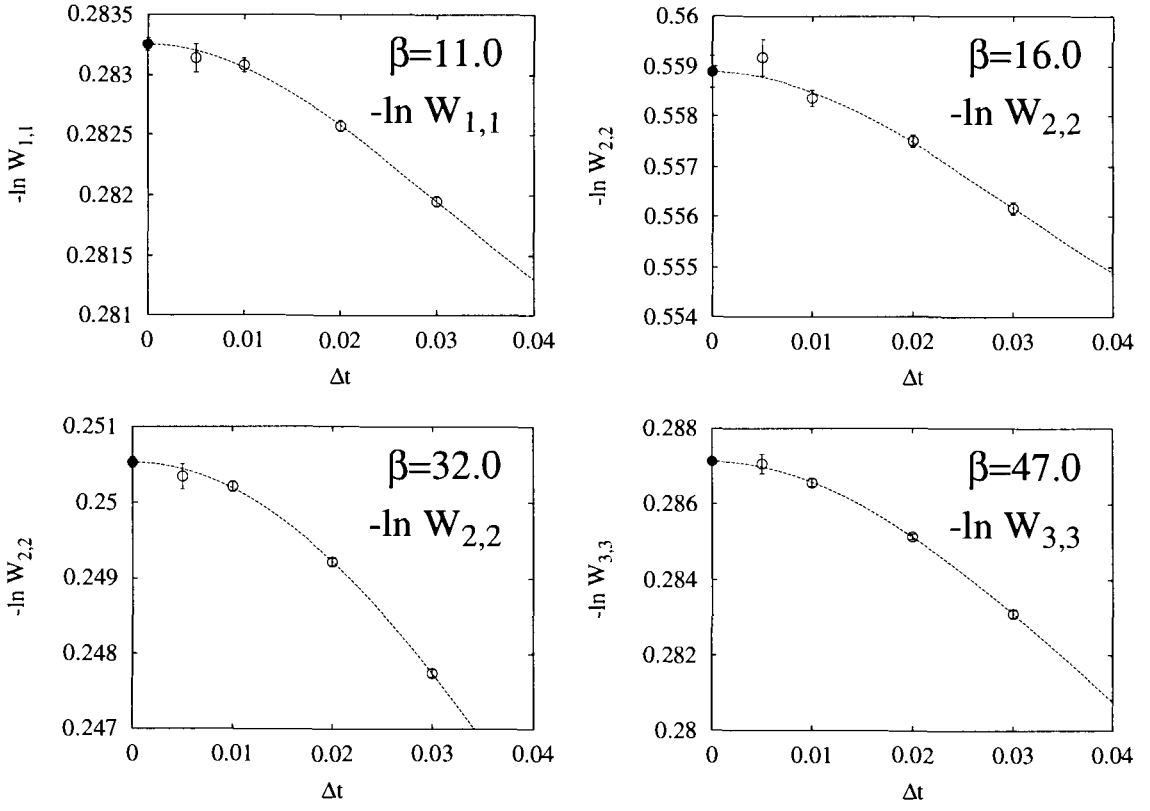

Figure 6.2: Zero step size extrapolation for the R-algorithm.

Dependence on N ($\bar{\sigma}_n = 1.0$)				Dependence on $\bar{\sigma}_n$ ($N = 6$)			
c_n	$N = 4$	$N = 5$	$N = 6$	c_n	$\bar{\sigma}_n = 0.5$	$\bar{\sigma}_n = 1.0$	$\bar{\sigma}_n = 5.0$
c_1	1.1499(4)	1.1499(4)	1.1499(4)	c_1	1.1498(3)	1.1499(4)	1.1502(5)
c_2	-0.641(15)	-0.641(15)	-0.641(15)	c_2	-0.636(12)	-0.641(15)	-0.658(27)
c_3	0.58(20)	0.58(20)	0.58(20)	c_3	0.51(12)	0.58(20)	0.85(43)
c_4	-0.2(9)	-0.2(9)	-0.2(9)	c_4	0.0(5)	-0.2(9)	-1.4(23)
c_5		-0.1(10)	-0.1(10)	c_5	0.0(5)	-0.1(10)	-0.8(48)
c_6			0.0(10)	c_6	0.0(5)	0.0(10)	-0.2(50)
χ^2	0.53	0.53	0.53	χ^2	1.2	0.53	0.25

Table 6.10: Dependence on N and the prior width $\bar{\sigma}_n$ for constrained curve fitting. Results are shown for the 2×2 loop, $n_f = 1$.

with constrained curve fitting. In Table 6.10 we again check the dependence of the fits on N and $\bar{\sigma}_n$ to see how sensitive our data are to the higher-order terms in the expansion. As before the priors are always set equal to $\bar{c}_n = 0$ and the same width is used for all n. Results are shown for the 2×2 loop. Perturbative calculations of Ref. [33] give $c_1 = 1.1499(0)$, $c_2 = -0.643(2)$, $c_3 = 0.59(9)$. Once again c_1, c_2 and c_3 are very insensitive to N and $\bar{\sigma}_n$. Note that the prior $\bar{c}_n \pm \bar{\sigma}_n = 0 \pm 5.0$ clearly under-constraints the coefficients, although the results are still statistically consistent with those obtained using other values of $\bar{\sigma}_n$. The optimal value of $\bar{\sigma}_n$ is determined to be ≈ 1.0 in this case.

Fit results are presented in Table 6.11 with $N = 6$ and $\bar{c}_n \pm \bar{\sigma}_n = 0 \pm 1.0$. The agreement with the analytic results is remarkable! Note that the coefficients are much better determined here than in the unimproved case: errors are almost a factor of 3 smaller for c_2 and c_3. In fact we are able to obtain high precision predictions for these coefficients **even with no input from perturbation theory**. Since the precision of the Wilson loops is similar in the two simulations, this illustrates that more data points are helpful (we have two more β's for the MILC action) in improving the accuracy of the coefficients. To visualize the quality of the fits, we again plot κ_1, κ_2 and κ_3 in Fig 6.3 for the 2×2 loop. No signal for c_4^{MC} was found, as indicated from the flatness of the c_3 graph. All 4th-order coefficients were found to be equal to zero within errors.

Number of flavours: $n_f = 1$						
	Perturbation Theory			Monte Carlo Method		
Loop	c_1	c_2	c_3	c_1	c_2	c_3
1×2	0.9252(0)	-0.646(0)	0.23(5)	0.9251(3)	-0.644(13)	0.20(18)
1×3	0.9845(0)	-0.595(1)	0.38(6)	0.9845(3)	-0.599(14)	0.37(19)
2×2	1.1499(0)	-0.643(2)	0.59(9)	1.1499(4)	-0.641(15)	0.58(20)
2×3	1.2341(0)	-0.595(3)	0.85(16)	1.2342(4)	-0.599(19)	0.88(26)

Table 6.11: Perturbative coefficients of various small Wilson loops for the MILC action.

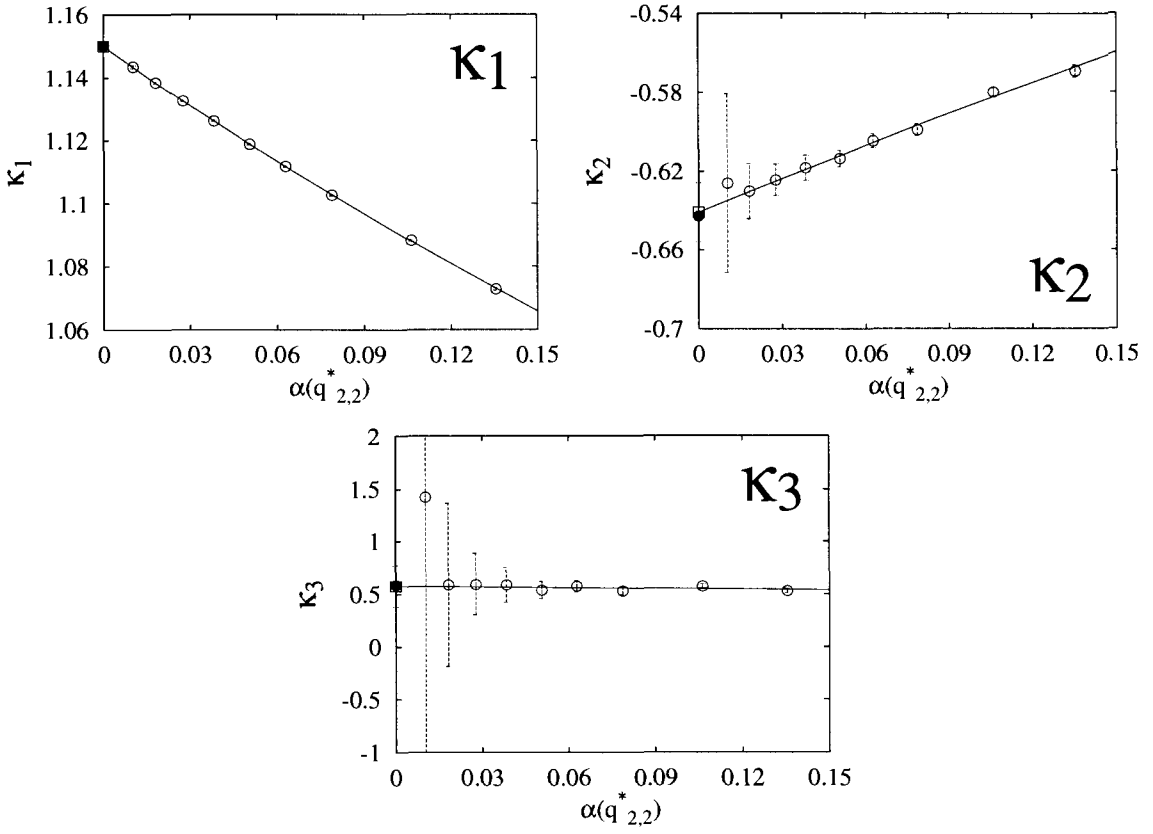

Figure 6.3: Plots of κ_1, κ_2, and κ_3 [2×2 loop, $n_f = 1$, the MILC action]. The Monte Carlo results c_n^{MC} are labeled by symbols □ and the analytic results are labeled by symbols •.

Number of flavours: $n_f = 1$				
	Perturbation Theory		Monte Carlo Method	
Loop	c_2	c_3	c_2	c_3
1×2	-0.646(0)	0.23(5)	-0.649(5)	0.26(12)
1×3	-0.595(1)	0.38(6)	-0.600(6)	0.39(13)
2×2	-0.643(2)	0.59(9)	-0.642(7)	0.59(14)
2×3	-0.595(3)	0.85(16)	-0.594(7)	0.82(15)

Table 6.12: Second and third order coefficients with c_1 fixed to the analytic results.

Loop	c_3 (PT)	c_3 (MC)
1×2	0.23(5)	0.21(4)
1×3	0.38(6)	0.28(5)
2×2	0.59(9)	0.61(6)
2×3	0.85(16)	0.84(8)

Table 6.13: Third order coefficients with both c_1 and c_2 fixed to the analytic results.

Once again we can set the priors of the lower-order coefficients to the analytic results to enhance the statistics of higher-order coefficients. This is done in Table 6.12 where only c_1 is fixed, and in Table 6.13 where both c_1 and c_2 are set to the perturbative values. The expansion is again truncated at α_V^6 and $\bar{c}_n \pm \bar{\sigma}_n = 0 \pm 1.0$ are used for the undetermined coefficients. In the latter case, all Monte Carlo results have a smaller error than those obtained analytically. The agreement with perturbation theory remains impressive.

6.4 Summary and Discussion

The perturbative coefficients of Wilson loops are extracted in *full* QCD, with the unimproved and Asqtad staggered quark actions, from Monte Carlo simulations at weak coupling. This is the first time that this method is applied to lattice actions where effects of dynamical fermions are included. Impressive agreement with the analytic calculations of Ref. [33] is obtained through third order. Results clearly show that Monte Carlo simulations are sensitive to fermion loops.

As mentioned earlier, Monte Carlo method is not a complete substitute for con-

ventional perturbation theory. It produces perturbative coefficients with statistical errors and truncation errors. However, accuracy can be greatly improved by using constrained curve fitting, and using perturbation theory input for lower-order coefficients. We observed that by setting the first order coefficients to the analytic results, the uncertainty in c_2 is only about a factor of 2 larger than those computed analytically; if both c_1 and c_2 are fixed, numerical simulations even give better predictions for the third order coefficients with smaller errors. This is significant since 2-loop perturbative calculations are extremely difficult. An alternative is to combine analytic calculations with Monte Carlo simulations: one can stop at 1-loop in perturbation theory, insert the results into the expansion, and allow simulations to determine c_3 or even higher-order coefficients. This approach avoids the evaluation of the hundreds of diagrams that could appear in higher-order calculations.

Another advantage of the Monte Carlo method is that many simulation codes are publicly available and one does not have to write their own program [5]. One simply have to choose an appropriate set of parameters, and do the simulations. Also the configurations can be reused to computed perturbative expansions of other observables: measure the observable of interest on the same set of configurations, and repeat the fitting procedures presented in the last two sections. In contrast it is a completely new problem to compute the expansion of another observable in conventional perturbation theory. The processes involved are completely different.

The biggest challenge of the Monte Carlo method is to have precise measurements of the observable. This requires an extensive study of all the possible systematic errors. Two distinct techniques are used in the present project to reduce the various systematic effects. First, **twisted boundary conditions are employed in the simulations**. This completely eliminates zero momentum modes which contribute a large part to the finite volume effect. Tunneling between the Z_3 phases is also strongly suppressed when twisted boundary conditions are applied to all three spatial directions. Secondly, **a new simulation algorithm, the rational hybrid Monte Carlo algorithm, is used for the unimproved staggered quark action**. The inclusion of an Monte Carlo accept/reject step makes this algorithm exact, i.e., there is no discretized time step error in measured expectation values. This is the first time that this algorithm is used in a large-scale simulation. We use the R-algorithm for the MILC action. In this case the finite step size errors are corrected by extrapolating

[5] Adapting the codes to twisted boundary conditions requires only minor modifications.

the results to $\Delta t = 0$. We have also discussed other sources of errors in Section 5.4, e.g., truncation errors, autocorrelation, and inaccuracy in matrix inversions. Since simulations and perturbation theory agree through third order, this shows that all systematic effects have been made smaller than the statistical errors, which are of $\mathcal{O}(10^{-5} - 10^{-6})$.

Finally we want to make a comment on the "fourth-root trick". Simulations were done with $n_f = 1$ and $n_f = 3$ hence the 12th-root and the 4th-root of the staggered quark determinant were taken. This procedure raises questions on the locality of the resulting action. Also the number of quark flavours has completely different interpretations in perturbation theory and Monte Carlo simulations: in perturbation theory n_f appears naturally in Feynman diagrams with fermion loops, while in numerical simulations the number of flavours is regarded as a parameter, which can be adjusted to any value by taking the appropriate root of the fermion determinant. Our study here, however, shows that this procedure of reducing quark flavours reproduces perturbative coefficients which agree, order-by-order, with perturbation theory. In particular simulations were done with $n_f = 1$ and $n_f = 3$ for the unimproved action, and results clearly show that Monte Carlo simulations are sensitive to fermion loops, with the correct value of n_f. Certainly we cannot consider this as a proof of the "fourth-root" trick. Nonetheless our work serves as another example where accurate results can be obtained with this formulation of staggered quarks.

In conclusion, this study not only provides an important cross-check of the perturbation theory input to a recent determination of the strong coupling $\alpha_{\overline{MS}}(M_Z)$ by the HPQCD collaboration, it also illustrates that perturbative series can be efficiently computed from Monte Carlo simulations at weak coupling.

Chapter 7

Conclusions

Two studies on improved staggered fermions have been presented in this thesis.

In the first project a systematic study of the spectral properties of a variety of improved staggered Dirac operators is presented. We observe that the distribution of low-lying eigenvalues depends sensitively on the way in which the operator is improved. Eigenmodes with very small eigenvalues and large chirality emerge as the level of improvement increases. These small eigenmodes can be identified as the chiral zero modes which contribute to the index theorem. The separation between these would-be zero modes and nonchiral modes becomes more clear when the gauge field action is also improved, or when one moves toward the continuum limit by reducing the lattice spacing. The distribution of the remaining nonchiral modes, after deleting the would-be zero modes from the spectrum, matches with the predictions of Random Matrix Theory not just for the trivial topological sector, but for $Q = 1, 2$ also. All of these give very strong evidence that staggered fermions do respond properly to gauge field topology, provided that discretization errors and lattice artifacts are significantly suppressed.

In the second project we computed the perturbative coefficients of Wilson loops, through third order, in *full* QCD from Monte Carlo simulations at weak coupling. Two lattice actions have been considered: the Wilson plaquette action and the unimproved staggered quark action, and the 1-loop improved gauge field action and the Asqtad quark action. This method is applied here for the first time to full QCD lattice actions. Twisted boundary conditions are used to eliminate zero momentum modes and to suppress tunneling between the Z_3 center phases. A new simulation algorithm, the rational hybrid Monte Carlo algorithm, is used for the unimproved action to

remove finite step size errors in simulation equations. This is the first time that this algorithm has been used in a numerical application, and our results will serve as an important benchmark for future simulations. Impressive agreement with perturbation theory is obtained. By setting the first and second order coefficients to the analytically known results in the fitting process, accuracy on the third order coefficients is greatly improved; all the third order coefficients have smaller errors than those obtained analytically. Results here provide an important cross-check of the perturbation theory input to a recent determination of the strong coupling $\alpha_{\overline{MS}}(M_Z)$ by the HPQCD collaboration.

This thesis demonstrates the importance of i) lattice action improvement, and ii) lattice perturbation theory, for reliable and high precision lattice calculations.

We have seen that the computational cost increases dramatically for small quark masses and small lattice spacings. Therefore simulations cannot be done at realistic quark masses, and discretization errors cannot be reduced by naïvely reducing the lattice spacing. Improved actions have smaller errors and better continuum properties, which allow simulations to be done at relatively coarse spacing. This is explicitly shown in the first project where the unimproved staggered quark operator is insensitive to gauge field topology even at a lattice spacing as small as 0.08fm, but results show that a lattice spacing $a \lesssim 0.1$fm is enough for the Asqtad operator to have a correct response to the topology with improved gauge fields. This spacing is of the order of the lattice spacings used in present-day state-of-the-act dynamical simulations of QCD.

The importance of lattice perturbation theory for high precision calculations was illustrated in Chapter 4 where we discussed in detail how to extract the strong coupling constant $\alpha_{\overline{MS}}(M_Z)$ from lattice simulations. To reduce systematic errors to the few percent level perturbative matching must be done through 2-loop. However higher-order analytic perturbation theory is very difficult because of the large number of diagrams that have to be evaluated. The second project of the thesis demonstrates that perturbative quantities can be efficiently computed from Monte Carlo simulations at weak coupling. This numerical approach produces estimates of higher-order coefficients with far less effort than conventional perturbation theory. We have also shown that accurate results for higher-order coefficients can be obtained by using perturbation theory input for lower-order coefficients.

The development of improved staggered quark actions over the past few years made

dynamical simulations possible at realistically small quark masses. Lattice perturbation theory, on the other hand, provides the connection between simulation results and continuum physical quantities. High precision lattice QCD is now possible, with improved staggered quarks [10]. Although the locality problem of staggered quark action is still to be resolved, the staggered quark formalism is the only discretization scheme which is capable of delivering accurate simulation results that can be compared with experiments in the near future.

Appendix A

Fermion Force in Molecular Dynamics Evolution

This appendix explains how to compute the matrix derivative $\frac{\partial M}{\partial U_{x,\mu}}$ [1] where

$$M_{x,y} = m\delta_{x,y} + D^{sf}_{x,y} = m\delta_{x,y} + \frac{1}{2}\sum_{\mu}\eta_{\mu}(x)\left(S_{x,\mu}\delta_{x,y-\hat{\mu}} - S^{\dagger}_{x-\hat{\mu},\mu}\delta_{x,y+\hat{\mu}}\right) \qquad \text{(A.1)}$$

is the staggered quark matrix (see (2.19)). For the unimproved staggered quark action S, $S^{\dagger}$ are the usual link variables U, $U^{\dagger}$. In general S, $S^{\dagger}$ are effective links, i.e., functions of U, $U^{\dagger}$.

The explicitly form of $\frac{\partial M}{\partial U_{x,\mu}}$ for the unimproved staggered quark action is given in Ref. [41]. An elegant implementation of the derivatives in numerical simulations for fat-link actions is given in Ref. [54]. This appendix concentrates on actions with unitarized fat-links, in particular the $(\text{UFat7})^n$ actions, which were studied recently by Kamleh *et al.* for FLIC fermions [75]. Dynamical simulations with the HYP action, which also utilizes unitarized links, were studied by Alexandru, Hasenfratz and Knechtli in Refs. [103, 104].

Let us consider the case with only one level of fattening/reunitarization as an example. The $\text{UFat7} = \text{Proj}_{SU(3)} \times \text{Fat7}$ action is in this form, and S, $S^{\dagger}$ are unitarized

[1] Since D^{sf} is anti-Hermitian, the formula for $\frac{\partial M^{\dagger}}{\partial U_{x,\mu}}$ is exactly the same as that of $\frac{\partial M}{\partial U_{x,\mu}}$ but with an extra negative sign.

Fat7-links U^R, $U^{R\dagger}$ constructed from Fat7 links U^F, $U^{F\dagger}$

$$\begin{cases} S = U^R(U^F, U^{F\dagger}) \\ S^\dagger = U^{R\dagger}(U^F, U^{F\dagger}) \end{cases}, \quad \begin{cases} U^F(U, U^\dagger) \\ U^{F\dagger}(U, U^\dagger) \end{cases}. \tag{A.2}$$

We treat U, $U^\dagger$ as independent variables, i.e. (restoring matrix indices a, b, p, q, ...),

$$\frac{\partial (U_{y,\nu})_{ab}}{\partial (U_{x,\mu})_{pq}} = \delta_{xy}\delta_{\mu\nu}\delta_{ap}\delta_{bq}, \quad \frac{\partial (U^\dagger_{y,\nu})_{ab}}{\partial (U_{x,\mu})_{pq}} = 0. \tag{A.3}$$

Note also that

$$\frac{\partial A^\dagger_{ab}}{\partial B_{pq}} = \left(\frac{\partial A_{ba}}{\partial B^\dagger_{qp}}\right)^*, \quad \frac{\partial A_{ab}}{\partial B_{pq}} = \left(\frac{\partial A^\dagger_{ba}}{\partial B^\dagger_{qp}}\right)^*. \tag{A.4}$$

Applying the chain rule to (A.2), we obtain

$$\begin{aligned} \frac{\partial (U^R_{y,\nu})_{ab}}{\partial (U_{x,\mu})_{pq}} &= \frac{\partial (U^R_{y,\nu})_{ab}}{\partial (U^F_{y,\nu})_{cd}} \frac{\partial (U^F_{y,\nu})_{cd}}{\partial (U_{x,\mu})_{pq}} + \frac{\partial (U^R_{y,\nu})_{ab}}{\partial (U^{F\dagger}_{y,\nu})_{cd}} \frac{\partial (U^{F\dagger}_{y,\nu})_{cd}}{\partial (U_{x,\mu})_{pq}} \\ &= (R_{y,\nu})^{ab}_{cd} (F^{y,\nu}_{x,\mu})^{cd}_{pq} + (\tilde{R}_{y,\nu})^{ab}_{cd} (\tilde{F}^{y,\nu}_{x,\mu})^{cd}_{pq} \\ \frac{\partial (U^{R\dagger}_{y,\nu})_{ab}}{\partial (U_{x,\mu})_{pq}} &= (\tilde{R}_{y,\nu})^{ba*}_{dc} (F^{y,\nu}_{x,\mu})^{cd}_{pq} + (R_{y,\nu})^{ba*}_{dc} (\tilde{F}^{y,\nu}_{x,\mu})^{cd}_{pq}. \end{aligned} \tag{A.5}$$

Hence the problem is reduced to the computation of two different types of derivatives, R, $\tilde{R}$ and F, $\tilde{F}$.

Derivatives of fat-links $F = \frac{\partial U^F}{\partial U}$, $\tilde{F} = \frac{\partial U^{F\dagger}}{\partial U}$

It is relatively straightforward to compute F and $\tilde{F}$ since fat-links are simple products of U, $U^\dagger$. For example, for Fat3 fattening, U^F, $U^{F\dagger}$ are 3-staple effective links

$$\begin{cases} U^F_{x,\mu} = \sum_{\nu\neq\mu} U_{x,\nu} U_{x+\hat{\nu},\mu} U^\dagger_{x+\hat{\mu},\nu} \\ U^{F\ \dagger}_{x,\mu} = \sum_{\nu\neq\mu} U_{x+\hat{\mu},\nu} U^\dagger_{x+\hat{\nu},\mu} U^\dagger_{x,\nu} \end{cases}. \tag{A.6}$$

To construct $(F^{y,\nu}_{x,\mu})^{ab}_{cd}$ or $(\tilde{F}^{y,\nu}_{x,\mu})^{ab}_{cd}$, one simply has to identify all the fat-links $U^F_{y,\nu}$ and $U^{F\dagger}_{y,\nu}$ which contain $U_{x,\mu}$, and to delete that link from each path (see Ref. [54] for details).

Derivatives of unitarized links $R = \frac{\partial U^R}{\partial U^F}$, $\tilde{R} = \frac{\partial U^R}{\partial U^{F\dagger}}$

First of all note that R and $\tilde{R}$ are local since reunitarization is local [2].

Traditional SU(3) projection, which is done by maximizing $\mathrm{ReTr}U^R U^{F\dagger}$ using an iterative procedure [74], is not differentiable. In Ref. [75], Kamleh *et al.* proposed to use the polar decomposition [105]

$$U^R = \frac{1}{(\mathrm{det}W)^{1/3}} W, \quad W = \frac{U^F}{\sqrt{U^{F\dagger}U^F}}, \tag{A.7}$$

so that the derivatives can be computed using standard matrix differentiation rules [106]. Kamleh *et al.* showed that these two methods produce unitarized fat-links which are numerically close even after many steps of smearing. The square-root in (A.7) can again be approximated by a Zolotarev expansion

$$W = U^F \left\{ \alpha_0 + \sum_i \frac{\alpha_i}{U^{F\dagger}U^F + \beta_i} \right\}. \tag{A.8}$$

Therefore

$$\begin{aligned} \frac{\partial W_{ab}}{\partial U^F_{pq}} &= \delta_{ap} \left\{ \alpha_0 + \sum_i \frac{\alpha_i}{U^{F\dagger}U^F + \beta_i} \right\}_{qb} \\ &- \sum_i \alpha_i \left(U^F \frac{1}{U^{F\dagger}U^F + \beta_i} U^{F\dagger} \right)_{ap} \left(\frac{1}{U^{F\dagger}U^F + \beta_i} \right)_{qb}. \end{aligned} \tag{A.9}$$

The derivative of the determinant is

$$\frac{\partial \mathrm{det}W}{\partial U^F_{pq}} = \mathrm{det}W \cdot \mathrm{Tr} \left(W^\dagger \frac{\partial W}{\partial U^F_{pq}} \right) \tag{A.10}$$

where matrix multiplication and trace are taken with respect to the indices on W. Combining (A.9) and (A.10), gives

$$(R_{x,\mu})^{ab}_{pq} = \frac{\partial (U^R_{x,\mu})_{ab}}{\partial (U^F_{x,\mu})_{pq}} = \frac{1}{(\mathrm{det}W)^{1/3}} \left\{ -\frac{1}{3} \mathrm{Tr} \left(W^\dagger \frac{\partial W}{\partial U^F_{pq}} \right) W_{ab} + \frac{\partial W_{ab}}{\partial U^F_{pq}} \right\}. \tag{A.11}$$

The derivative $(\tilde{R}_{x,\mu})^{ab}_{pq} = \frac{\partial (U^R_{x,\mu})_{ab}}{\partial (U^{F\dagger}_{x,\mu})_{pq}}$ can be obtained in a similar fashion.

[2] Because of this we will drop the space-time indices "x, μ" on the link variables in this section.

Summary

Gathering all the information, the derivative $\frac{\partial M}{\partial U_{x,\mu}}$ reads

$$\begin{aligned}\frac{\partial (M_{y,z})_{ab}}{\partial (U_{x,\mu})_{pq}} &= \sum_{\nu} \eta_\nu(y) \left(\delta_{y,z-\nu} \frac{\partial (U^R_{y,\nu})_{ab}}{\partial (U_{x,\mu})_{pq}} + \delta_{y,z+\nu} \frac{\partial (U^{R\dagger}_{y,\nu})_{ab}}{\partial (U_{x,\mu})_{pq}} \right) \\ &= \sum_{\nu} \eta_\nu(y) \Big(\delta_{y,z-\nu} \left[(R_{y,\nu})^{ab}_{cd} (F^{y,\nu}_{x,\mu})^{cd}_{pq} + (\tilde{R}_{y,\nu})^{ab}_{cd} (\tilde{F}^{y,\nu}_{x,\mu})^{cd}_{pq} \right] \\ &\qquad + \delta_{y,z+\nu} \left[(\tilde{R}_{y,\nu})^{ba^*}_{dc} (F^{y,\nu}_{x,\mu})^{cd}_{pq} + (R_{y,\nu})^{ba^*}_{dc} (\tilde{F}^{y,\nu}_{x,\mu})^{cd}_{pq} \right] \Big) . \quad \text{(A.12)}\end{aligned}$$

The calculation can be largely simplified if one contracts the upper indices a, b and space-time indices y, ν with those of the random source $|X\rangle$ first (see (5.41)). The lower indices p, q will be contracted with the indices of $U_{x,\mu}$ at the last step (see (5.39)).

Although the formula for $\frac{\partial M}{\partial U_{x,\mu}}$ looks very complicated, its structure is very convenient for numerical computation. In fact one only has to write two subroutines, one for R, $\tilde{R}$ and the other for F, $\tilde{F}$. These subroutines calculate the current derivatives, and multiply the results to the overall "chain" of derivatives. This procedure is very general and can be applied to almost any action. One simply has to rearrange the sequence in which the subroutines are called, and perform the appropriate index contraction (see also Ref. [75]).

We have developed computer codes for the $(\text{UFat7})^n \times \text{Asq}$ action. Some test runs were also done on 4^4 lattices [76].

Bibliography

[1] M. E. Peskin and D. V. Schroeder. An Introduction to Quantum Field Theory. *Perseus Books*, Massachusetts, 1995.

[2] S. Eidelman *et al.*, The Particle Data Group. Review of Particle Physics. *Physics Letters B*, **592**:1, 2004.

[3] D. J. Gross and F. Wilczek. Ultraviolet Behaviour of Non-Abelian Gauge Theories. *Physical Review Letters*, **30**:1343, 1973.

[4] H. D. Politzer. Reliable Perturbative Results for Strong Interactions. *Physical Review Letters*, **30**:1346, 1973.

[5] K. G. Wilson. Confinement of Quarks. *Physical Review D*, **10**:2445, 1974.

[6] K. G. Wilson. The Origins of Lattice Gauge Theory. *Nuclear Physics Proceeding Supplement*, **140**:3, 2005.

[7] H. D. Trottier and K. Y. Wong. Static Potential and Local Colour Fields in Unquenched Lattice QCD(3). Report Number hep-lat/0408028, 2004.

[8] E. Eichten, A. Duncan and H. Thacker. String Breaking in Four Dimensional Lattice QCD. *Physical Review D*, **63**:111501, 1974.

[9] G. P. Lepage. Redesigning Lattice QCD. Report Number hep-lat/9607076, 1996.

[10] C. T. H. Davies *et al.* High Precision Lattice QCD Confronts Experiment. *Physical Review Letters*, **92**:022001, 2004.

[11] C. T. H. Davies *et al.* A Precise Determination of α_s from Lattice QCD. *Physics Letters B*, **345**:42, 1995.

[12] C. T. H. Davies *et al.* Further Precise Determinations of α_s from Lattice QCD. *Physical Review D*, **56**:2755, 1997.

[13] Q. Mason *et al.* Accurate Determination of α_s from Realistic Lattice QCD. Report Number hep-lat/0503005, 2005.

[14] M. Okamoto. Full CKM Matrix with Lattice QCD. Report Number hep-lat/0412044, 2004.

[15] S. Weinberg. The U(1) Problem. *Physical Review D*, **11**:3583, 1975.

[16] S. L. Adler. Axial-Vector Vertex in Spinor Electrodynamics. *Physical Review*, **177**:2426, 1969.

[17] J. S. Bell and R. Jackiw. A PCAC Puzzle: $\pi_0 \to \gamma\gamma$ in the Sigma Model. *Nuovo Cimento A*, **60**:47, 1969.

[18] R. Rajaraman. Solitons and Instantons. *North-Holland Publishing Company*, New York, 1982.

[19] E. Witten. Current Algebra Theorems for the U(1) "Goldstone Boson". *Nuclear Physics B*, **156**:269, 1979.

[20] G. Veneziano. U(1) without Instantons. *Nuclear Physics B*, **159**:213, 1979.

[21] M. F. Atiyah and I. M. Singer. The Index of Elliptic Operators. *Annals of Mathematics*, **87**:484, 1968.

[22] H. J. Rothe. Lattice Gauge Theoreis. *World Scientific Publishing Co. Pte. Ltd.*, Singapore, 1992.

[23] M. E. Berbenni-Bitsch *et al.* Microscopic Universality in the Spectrum of the Lattice Dirac Operator. *Physical Review Letters*, **80**:1146, 2004.

[24] M. Göckeler *et al.* Small Eigenvalues of the SU(3) Dirac Operator on the Lattice and in Random Matrix Theory. *Physical Review D*, **59**:094503, 1999.

[25] R. Niclasen, P. H. Damgaard, U. M. Heller and K. Rummukainen. Staggered Fermions and Gauge Field Topology. *Physical Review D*, **61**:014501, 1999.

[26] J. J. M. Verbaarschot and I. Zahed. Spectral Density of the QCD Dirac Operator near Zero Virtuality. *Physical Review Letters*, **70**:3852, 1993.

[27] P. H. Ginsparg and K. G. Wilson. A Remnant of Chiral Symmetry on the Lattice. *Physical Review D*, **25**:2649, 1982.

[28] M. Lüscher. Exact Chiral Symmetry on the Lattice and the Ginsparg-Wilson Relation. *Physics Letters B*, **428**:342, 1998.

[29] K. Jansen, W. Bietenholz and S. Shcheredin. Spectral Properties of the Overlap Dirac Operator in QCD. *Journal of High Energy Physics*, **307**:33, 2003.

[30] J.-F. Lagaë, J. B. Kogut and D. K. Sinclair. Topology, Fermionic Zero Modes, and Flavour Singlet Correlators in Finite Temperature QCD. *Physical Review D*, **58**:054504, 1998.

[31] G. P. Lepage. Flavor-Symmetry Restoration and Symanzik Improvement for Staggered Quarks. *Physical Review D*, **59**:074502, 1999.

[32] Q. J. Mason. High Precision Lattice QCD: Perturbations in a Non-Perturbative World. *Ph.D. Thesis, Cornell University*, 2004.

[33] H. D. Trottier and Q. Mason. Third-Order Pertubation Theory for α_P and Small Wilson Loops for Three Lattice Actions, unpublished.

[34] M. Lüscher and P. Weisz. Efficient Numerical Techniques for Perturbative Lattice Gauge Theory Computations. *Nuclear Physics B*, **266**:309, 1986.

[35] G. P. Lepage, W. C. Dimm and P. B. Mackenzie. Nonperturbative "Lattice Perturbation Theory". *Nuclear Physics Proceeding Supplement*, **42**:403, 1995.

[36] N. H. Shakespeare. Simulations of Non-Relativistic Quantum Chromodynamics at Strong and Weak Coupling. *Ph.D. Thesis, Simon Fraser University*, 2000.

[37] G.P. Lepage, H. D. Trottier, N. H. Shakespeare and P. B. Mackenzie. Perturbative Expansions from Monte Carlo Simulations at Weak Coupling: Wilson Loops and the Static Quark Selfenergy. *Physical Review D*, **65**:094502, 2002.

[38] R. R. Horgan, A. Hart and L. C. Storoni. Perturbation Theory vs. Simulation for Tadpole Improvement Factors in Pure Gauge Theories. *Physical Review D*, **70**:034501, 2004.

[39] D. Toussaint, K. Orginos and R. L. Sugar. Variants of Fattening and Flavour Symmetry Restoration. *Physical Review D*, **60**:054503, 1999.

[40] A. D. Kennedy, I. Horvath and S. Sint. A New Exact Method for Dynamicl Fermion Computations with Non-Local Actions. *Nuclear Physics Proceeding Supplement*, **73**:834, 1999.

[41] S. Gottlieb *et al.* Hybrid-Molecular-Dynamics Algorithms for the Numerical Simulation of Quantum Chromodynamics. *Physical Review D*, **35**:2531, 1987.

[42] F. Di Renzo *et al.* Four-Loop Result in SU(3) Lattice Gauge Theory by a Stochastic Method: Lattice Correction to the Condensate. *Nuclear Physics B*, **426**:675, 1994.

[43] F. Di Renzo and L. Scorzato. Numerical Stochastic Perturbation Theory for Full QCD. *Journal of High Energy Physics*, **410**:73, 2004.

[44] J. Kogut and L. Susskind. Hamiltonian Formulation of Wilson's Lattice Gauge Theories. *Physical Review D*, **11**:395, 1983.

[45] H. Neuberger. Exactly Massless Quarks on the Lattice. *Physics Letters B*, **417**:141, 1998.

[46] H. Neuberger. A Practical Implementation of the Overlap Dirac Operator. *Physical Review Letters*, **81**:4060, 1998.

[47] K. G. Wilson. Quarks and Strings on a Lattice. New Phenomena in Subnuclear Physics, ed. A. Zichichi. *Plenum Press*, New York, 1975.

[48] O. Napoly, H. Kluberg-Stern, A. Morel and B. Petersson. Flavours of Lagrangian Susskind Fermions. *Nuclear Physics B*, **220**:447, 1983.

[49] K. Jansen. Actions for Dynamical Fermion Simulations: Are We Ready to Go? *Nuclear Physics Proceeding Supplement*, **129**:3, 2004.

[50] K. Jansen, B. Bunk, M. Della Morte and F. Knechtli. Locality with Staggered Fermions. *Nuclear Physics B*, **697**:343, 2004.

[51] H. Neuberger. The Fourth Root of the Kogut-Susskind Determinant via Infinite Component Fields. *Physical Review D*, **70**:097504, 2004.

[52] D. H. Adams. On the Fourth Root Prescription for Dynamical Staggered Fermions. Report Number hep-lat/0411030, 2004.

[53] W. Lee and S. R. Sharpe. Partial Flavour Symmetry Restoration for Chiral Staggered Fermions. *Physical Review D*, **60**:114503, 1999.

[54] K. Orginos and D. Toussaint. Tests of Improved Kogut-Susskind Fermion Actions. *Nuclear Physics Proceeding Supplement*, **73**:909, 1999.

[55] U. M. Heller, R. G. Edwards and R. Narayanan. A Study of Practical Implementations of the Overlap-Dirac Operator in Four Dimensions. *Nuclear Physics B*, **540**:457, 1999.

[56] M. Golterman and Y. Shamir. Overlap-Dirac Fermions with a Small Hopping Parameter. *Journal of High Energy Physics*, **09**:006, 2000.

[57] N. Cundy *et al.* Numerical Methods for the QCD Overlap Operator: III. Nested Iterations. Report Number hep-lat/0405003, 2004.

[58] R. Narayanan, Y. Kikukawa and H. Neuberger. Finite Size Corrections in Two Dimensional Gauge Theories and a Quantitative Chiral Test of the Overlap. *Physics Letters B*, **399**:105, 1997.

[59] C. H. Huang, W. Chiu, T. H. Hsieh and T. R. Huang. Note on the Zolotarev Optimal Rational Approximation for the Overlap Dirac Operator. *Physical Review D*, **66**:114502, 2002.

[60] C. Aubin *et al.* Light Pseudoscalar Decay Constants, Quark Masses, and Low Energy Constants from Three-Flavour Lattice QCD. *Physical Review D*, **70**:114501, 2004.

[61] W. Bardeen *et al.* Light Quarks, Zero Modes, and Exceptional Configurations. *Physical Review D*, **57**:1633, 1998.

[62] S. D. Katz, Z. Fodor and K. K. Szabó. Dynamical Overlap Fermions, Results with Hybrid Monte-Carlo Algorithm. *Journal of High Energy Physics*, **408**:3, 2004.

[63] A. D. Kennedy. Algorithms for Lattice QCD with Dynamical Fermions. Report Number hep-lat/0409167, 2004.

[64] M. Lüscher and P. Weisz. On-Shell Improved Lattice Gauge Theories. *Communications in Mathematical Physics*, **97**:59, 1985.

[65] G. P. Lepage and P. B. Mackenzie. Viability of Lattice Perturbation Theory. *Physical Review D*, **48**:2250, 1993.

[66] S. Elitzur. Impossibility of Spontaneously Breaking Local Symmetries. *Physical Review D*, **12**:3978, 1975.

[67] C. Bernard *et al.* Quenched Hadron Spectroscopy with Improved Staggered Quark Action. *Physical Review D*, **58**:014503, 1998.

[68] T. Blum *et al.* Improving Flavour Symmetry in the Kogut-Susskind Hadron Spectrum. *Physical Review D*, **55**:1133, 1997.

[69] J. F. Lagaë and D. K. Sinclair. Improved Staggered Quark Actions with Reduced Flavour Symmetry Violations for Lattice QCD. *Physical Review D*, **59**:014511, 1999.

[70] K. Orginos *et al.* Testing Improved Actions for Dynamical Kogut-Susskind Quarks. *Physical Review D*, **59**:014501, 1999.

[71] W. Lee. Perturbative Improvement of Staggered Fermions using Fat Links. *Physical Review D*, **66**:114504, 2002.

[72] A. Hasenfratz and F. Knechtli. Flavour Symmetry and the Static Potential with Hypercubic Blocking. *Physical Review D*, **64**:034504, 2001.

[73] E. Follana *et al.* Improvement and Taste Symmetry Breaking for Staggered Quarks. *Nuclear Physics Proceeding Supplement*, **129**:384, 2004.

[74] J. Hoek. Optimized Monte Carlo Renormalization Group Transformations for SU(3) Lattice Gauge Theory. *Nuclear Physics B*, **329**:240, 1990.

[75] D. B. Leinweber, W. Kamleh and A. G. Williams. Hybrid Monte Carlo Algorithm with Fat Link Fermion Actions. *Physical Review D*, **70**:014502, 2004.

[76] R. M. Woloshyn and K. Y. Wong. Calculating the Fermion Contribution to the Force, unpublished.

[77] M. L. Mehta. Random Matrices and the Statistical Theory of Energy Levels. *Academic Press*, New York, 1967.

[78] M. L. Mehta. Random Matrices. *Academic Press*, San Diego, 1967.

[79] J. B. Zhang *et al.* Numerical Study of the Lattice Index Theorem using Improved Cooling and Overlap Fermions. *Physical Review D*, **65**:074510, 2002.

[80] P. Weisz, L. Giusti, M. Lüscher and H. Wittig. Lattice QCD in the ϵ-Regime and Random Matrix Theory. *Journal of High Energy Physics*, **311**:23, 2003.

[81] S. J. Hands and M. Teper. On the Value and Origin of the Chiral Condensate in Quenched SU(2) Lattice Gauge Theory. *Nuclear Physics B*, **347**:819, 1990.

[82] T. Kalkreuter. Spectrum of the Dirac Operator and Multigrid Algorithm with Dynamical Staggered Fermions. *Physical Review D*, **51**:1305, 1995.

[83] S. P. Booth *et al.* Towards the Continuum Limit of SU(2) Lattice Gauge Theory. *Physics Letters B*, **275**:424, 1992.

[84] M. Creutz. Monte Carlo Study of Quantized SU(2) Gauge Theory. *Physical Review D*, **21**:2308, 1980.

[85] N. Cabibbo and E. Marinari. A New Method for Updating SU(N) Matrices in Computer Simulations of Gauge Theories. *Physics Letters B*, **119**:387, 1982.

[86] T. Kalkreuter and H. Simma. An Accelerated Conjugate Gradient Algorithm to Compute Low Lying Eigenvalues: a Study for the Dirac Operator in SU(2) Lattice QCD. *Computer Physics Communications*, **93**:33, 1996.

[87] U. Heller and F. Karsch. One-Loop Perturbative Calculation of Wilson Loops on Finite Lattices. *Nuclear Physics B*, **251**:254, 1985.

[88] G. P. Lepage, S. J. Brodsky and P. B. Mackenzie. On the Elimination of Scale Ambiguities in Perturbative Quantum Chromodynamics. *Physical Review D*, **28**:228, 1983.

[89] A. Billoire. Another Connection between the Λ Parameters of the Euclidean Lattice and Continuum QCD. *Physics Letters B*, **104**:472, 1981.

[90] Y. Schröder. The Static Potential in QCD to Two Loops. *Physics Letters B*, **447**:321, 1999.

[91] J. Jurkiewicz, A. Coste, A. Gonzalez-Arroyo and C. P. Korthals Altes. Zero-Momentum Contributions to Wilson Loops in Periodic Boxes. *Nuclear Physics B*, **262**:67, 1985.

[92] G. Parisi. Prolegomena to any Future Computer Evaluation of the QCD Mass Spectrum. *Summer Institute Progress in Gauge Field Theory, Cargese*, page 531, 1983.

[93] B. J. Pendleton, S. Duane, A. D. Kennedy and D. Roweth. Hybrid Monte Carlo. *Physics Letters B*, **195**:216, 1987.

[94] B. Joó, M. A. Clark and A. D. Kennedy. The RHMC Algorithm for Two Flavours of Dynamical Staggered Fermions. *Nuclear Physics Proceeding Supplement*, **129**:850, 2004.

[95] A. Frommer *et al.* Accelerating Wilson Fermion Matrix Inversions by means of the Stabilized Biconjugate Gradient Algorithm. *International Journal of Modern Physics C*, **5**:1073, 1994.

[96] S. L. B. Moshier. Methods and Programs for Mathematical Functions. *Halsted Press*, New York, 1989.

[97] A. Frommer *et al.* Many Masses on One Stroke: Economic Computation of Quark Propagators. *International Journal of Modern Physics C*, **6**:627, 1995.

[98] G. G. Batrouni *et al.* Langevin Simulations of Lattice Field Theories. *Physical Review D*, **32**:2736, 1985.

[99] G. P. Lepage *et al.* Constrained Curve Fitting. *Nuclear Physics Proceeding Supplement*, **106**:12, 2002.

[100] K. Akemi *et al.* Systematic Study of Autocorrelation Time in Pure SU(3) Lattice Gauge Theory. *Nuclear Physics Proceeding Supplement*, **34**:789, 1993.

[101] B. Efron. Computers and the Theory of Statistics: Thinking the Unthinkable. *Society for Industrial and Applied Mathematics Review*, **21**:460, 1979.

[102] G. P. Lepage. A New Algorithm for Adaptive Multidimensional Integration. *Journal of Computational Physics*, **27**:192, 1978.

[103] A. Hasenfratz and F. Knechtli. Simulation of Dynamical Fermions with Smeared Links. *Computer Physics Communications*, **148**:81, 2002.

[104] A. Alexandru and A. Hasenfratz. Partial-Global Stochastic Metropolis Update for Dynamical Smeared Link Fermions. *Physical Review D*, **66**:094502, 2002.

[105] N. J. Higham *et al.* Numerical Analysis Report 426. *Manchester Center for Computational Mathematics*, 2003.

[106] D. A. Harville. Matrix Algebra from a Statistician's Perspective. *Springer-Verlag New York Inc.*, New York, 1997.